



**Representative volume element size,  
Length-scale identification, and  
Stop-band frequencies in  
magnetorheological elastomers**

Sinan Eraslan

A thesis submitted for the degree of  
Doctor of Philosophy

Department of Mechanical Engineering

01/2023

# Summary

Smart composite materials have garnered a great interest from the engineering community, and been the subject of many studies in the last few decades. This is a commonly used terminology for composite materials being responsive to an external stimulus such as electric/magnetic field, light, pH or temperature. Specifically, magnetorheological elastomers (MREs) are examples of such responsive composites, typically they consist of ferromagnetic particles embedded in a polymer network. These composites exhibit a coupling behaviour between magnetism and elasticity via the magnetostriction effect occurring in the magnetic particles.

The underlying microstructure is a fundamental property in the analysis of heterogeneous materials' behaviour. Microstructural information needs to be taken into account in the macroscopic continuum to accurately describe and predict the material response. Therefore, the main aim of this study is to develop numerical models and investigate the static and dynamic behaviour of MRE materials by considering the influence of microstructural properties. In the static aspect, a multi-scale model has been proposed based on a non-local homogenisation scheme. In this analytical homogenisation approach, microstructural effects have been introduced to macroscopic magneto-elastic continua via additional material parameters: length-scales expressed in terms of Representative Volume Elements (RVE). Hence, a numerically-statistical procedure has been presented to define and determine the RVE sizes for an MRE material. Further, the key parameters, influencing the size of the determined RVE sizes have been studied. Thereafter, length-scale enriched generalised gradient magneto-elastic continuum model has been used with the determined RVE sizes to study the effectiveness of the model compared to a classical magneto-elastic continuum formulation that lacks of microstructural information. Moreover, the effects of geometrical properties and magneto-elastic coupling on the longitudinal wave propagation have been investigated, in particular, from appearance of band gap phenomenon in the dynamic aspect.

# Acknowledgements

First of all, I would like to express my sincere gratitude to my supervisors: Prof. Inna M. Gitman, Prof. Harm Askes and Prof. René de Borst who have provided me extensive professional guidance through each stage of this thesis. I am extremely grateful for the continuous support in my Ph.D study and related research, for their patience, motivation, and immense knowledge. Their guidance helped me in all the time of research and writing of this thesis. I could not have imagined having a better mentoring for my PhD study.

I would like to express my sincere appreciation to International Graduate Education Scholarship (YLSY), Türkiye government's international scholarship programme funded by The Ministry of National Education of Türkiye, for letting me be part of this incredible network.

And my biggest thanks to my family for all the support you have shown me through this research, the culmination of four years of distance learning. This accomplishment would not have been possible without them. Thank you.

I want to acknowledge my friends Eren, Bilge, Ozcan and Joaquin for the support that they have given me over the years. You have been a great source of comfort, love and inspiration since I met you. Without you by my side as my constant support and joy, I would not have managed in life as well as I did. You were there when I needed you the most. Lastly, I could not have asked for better people in my research group. I would like to thank Ruixuan, Iwo and Zakaria. Thank you for being there for me, thank you for caring and sharing especially in Covid-19 lockdown times.

I am also thankful to the department of mechanical engineering and all its member's staff for all the considerate guidance.

# Contents

<b>1</b>	<b>Introduction</b>	<b>10</b>
1.1	Magnetorheological elastomers with Terfenol-D . . . . .	15
1.2	Particulate MREs and influential parameters in magneto-elastic behaviour	18
1.3	Magneto-elastic modelling . . . . .	21
1.3.1	Macro-scale modelling in magneto-elasticity . . . . .	22
1.3.2	Micro-scale modelling in magneto-elasticity . . . . .	24
1.3.3	Multi-scale modelling in magneto-elasticity . . . . .	25
1.3.4	Representative volume element . . . . .	27
1.4	Piezomagnetism . . . . .	28
1.5	Motivations . . . . .	30
1.6	Outline . . . . .	33
<b>2</b>	<b>Determination of RVE size for an MRE</b>	<b>35</b>
2.1	Formulation and introduction of methodology . . . . .	36
2.1.1	Microscopic characterisation of MRE . . . . .	38
2.1.2	Finite element equations . . . . .	40
2.1.3	Definition and determination procedure of RVEs . . . . .	41
2.2	Numerical results and influence of material properties on RVEs . . . . .	46
2.2.1	Contrast in elastic properties . . . . .	48
2.2.2	Contrast in piezomagnetic coupling properties . . . . .	49
2.2.3	Contrast in magnetic permeability properties . . . . .	51
2.2.4	Larger contrast in elastic and magnetic properties . . . . .	52
2.3	Discussion . . . . .	53
<b>3</b>	<b>RVE Sizes and Length-Scale Identification in Generalised Magneto-Elasticity</b>	<b>55</b>
3.1	Non-local homogenisation . . . . .	56

---

3.2	Homogenisation and macroscopic length-scale parameter in MREs . . . . .	59
3.3	RVE Sizes and Identification of Characteristic Length-Scale Parameter . . .	62
3.4	Finite element formulations . . . . .	63
3.5	Removal of singularities . . . . .	68
3.6	Discussion . . . . .	71
<b>4</b>	<b>Effects of randomness and piezomagnetic coupling on the appearance of stop-bands in MREs</b>	<b>73</b>
4.1	Magneto-elastic materials and wave band-gaps . . . . .	74
4.2	Continuum equations and discretisation aspects . . . . .	76
4.3	Numerical test setup . . . . .	78
4.4	Results and analysis of influential parameters on stop-bands . . . . .	82
4.4.1	Periodic microstructure . . . . .	83
4.4.2	Random microstructure . . . . .	89
4.5	Discussion . . . . .	95
<b>5</b>	<b>Conclusions</b>	<b>97</b>
<b>6</b>	<b>Future works</b>	<b>102</b>
<b>A</b>	<b>Weak form derivation on micro-scale</b>	<b>104</b>
<b>B</b>	<b>Integrations of non-local homogenisation</b>	<b>106</b>

# List of Figures

1.1	Typical magnetostriction curve with particular regions (schematic) . . . . .	11
1.2	Representation magnetisation process . . . . .	11
1.3	Examples and various shapes of MREs. (Reprinted with permission. ©K. Dobberke for Fraunhofer ISC, 2018) . . . . .	13
1.4	Long (a) and short (b) fibres of Terfenol-D. (Reprinted with permission, from Lo et al., ©2006 IEEE.) . . . . .	16
1.5	SEM images of Terfenol-D particles with various distributions (a) 250–300, (b) 90–106, (c) <300, and (d) <45 $\mu\text{m}$ . (Reprinted from Duenas and Carman, with the permission of AIP Publishing.) . . . . .	16
1.6	SEM images of isotropic and anisotropic polymer-bonded Carbonyl Iron (CI) powder composites with permission from Elsevier. . . . .	18
1.7	Anisotropic polymer-bonded Terfenol-D composite. Reprinted with the permission of AIP Publishing. . . . .	19
1.8	Different approaches. Macrostructural (a), microstructural (b) and Multi-scale approach (c) . . . . .	22
1.9	Analytical (a) and computational (b) homogenisation representation . . . . .	26
2.1	Different realisations of the unit cell and FE discretisation (size $1 \times 1 \text{ mm}^2$ and $V_f = 30\%$ ) . . . . .	42
2.2	An RVE under external loadings . . . . .	42
2.3	Periodic boundary conditions . . . . .	43
2.4	Different sizes of unit cells (from left to right: $0.5 \times 0.5 \text{ mm}^2$ , $1 \times 1 \text{ mm}^2$ , $1.5 \times 1.5 \text{ mm}^2$ , $2 \times 2 \text{ mm}^2$ and $V_f = 30\%$ ) . . . . .	45
2.5	Procedure of RVEs sizes determination . . . . .	45
2.6	Convergence of the results . . . . .	47

2.7	RVE sizes for different stiffness contrast values. $L_1$ (a), $L_4$ (b), $L_2$ (c), and $L_3$ (d). . . . .	49
2.8	RVE sizes for different piezomagnetic contrast values. $L_1$ (a), $L_4$ (b), $L_2$ (c), and $L_3$ (d). . . . .	50
2.9	RVE sizes for different permeability contrast values. $L_1$ (a), $L_4$ (b), $L_2$ (c), and $L_3$ (d). . . . .	52
2.10	RVE sizes for larger contrast values . . . . .	53
3.1	Procedure of gradient enriched piezomagnetic model solution . . . . .	67
3.2	MRE Plate with a crack and finite element discretisation (Units: mm and thickness=5 mm) . . . . .	69
3.3	$\epsilon$ and $\mathbf{H}$ distributions along z-axis based on $\epsilon\&\mathbf{H} - \text{RA}$ approach . . . . .	70
4.1	Numerical model of simulation . . . . .	78
4.2	Procedure of wave propagation and stop-band analysis . . . . .	81
4.3	Example of test materials. Periodic (a), randomness in particle size (b), position (c) and both (d). ( $V_f = 30\%$ ) . . . . .	83
4.4	Transmission coefficients on the recording points for a periodic structure. Decoupled (left) and coupled (right).( $V_f = 30\%$ ) . . . . .	84
4.5	The average transmission coefficient $\bar{T}$ and effect of magneto-elastic coupling on the stop-band frequencies in periodic microstructure. . . . .	84
4.6	Increased volume fraction for periodic test material: $V_f = 30\%$ (a), $V_f = 45\%$ (b). . . . .	85
4.7	Transmission coefficients on the recording points for a periodic structure. Decoupled (left) and coupled (right).( $V_f = 45\%$ ) . . . . .	85
4.8	The average transmission coefficient $\bar{T}$ and the effect of volume fraction on the wave propagation. . . . .	86
4.9	Different particle sizes: smaller (a), original (b), larger (c). ( $V_f = 30\%$ ) . . . . .	86
4.10	Transmission coefficients on the recording points for different particle sizes. Smaller (a), original (b), larger (c) particle for $V_f = 30\%$ . Decoupled (left)/coupled (right). . . . .	87
4.11	The average transmission coefficient $\bar{T}$ and the effect of particle size on the wave propagation in coupled/decoupled cases. Decoupled (top), coupled (bottom). . . . .	88
4.12	Randomness added to particles sizes (a) or particles positions (b). ( $V_f = 30\%$ ) . . . . .	89

4.13	Transmission coefficients on the recording points for size randomness only. Decoupled (left) and coupled (right). . . . .	90
4.14	Transmission coefficients on the recording points for position randomness only. Decoupled (left) and coupled (right) . . . . .	90
4.15	The average transmission coefficient $\bar{T}$ and the effect of randomness in size, position and periodic on the wave propagation. Decoupled (top)/Coupled (bottom). . . . .	91
4.16	Randomness added to particles sizes and positions simultaneously. Three different realisations a, b and c from left to right. ( $V_f = 30\%$ ) . . . . .	92
4.17	Transmission coefficients $T_i$ in periodic and fully random test materials. Decoupled (left) and coupled (right). . . . .	93
4.18	The average transmission coefficient $\bar{T}$ in case of fully random material realisations and periodic material. Periodic, realisation-a, realisation-b, realisation-c. Decoupled (left)/Coupled (right). . . . .	94
B.1	Representative Volume Element . . . . .	106

# List of Tables

1.1	Relationship between constants in different forms . . . . .	30
1.2	Piezomagnetic terminology . . . . .	30
2.1	Material properties . . . . .	39
3.1	Effective material properties of MRE plate . . . . .	69
4.1	Size of the parts in the test setup (sizes in mm). . . . .	79
4.2	Material properties of test material . . . . .	82

# Chapter 1

## Introduction

Stimuli-responsive materials and their composites have taken a great interest of the engineering community in the last few decades due to their controllable/adjustable behaviours and properties. These materials can respond to an external stimulus such as temperature, light, pH, electric or magnetic field. Thus, they can alter their properties such as shape, size, permeability, mechanical or optical features [1, 2].

Magnetostrictive materials, which exhibit magnetostriction under magnetic field, are one of the well-known stimuli-responsive materials. Magnetostriction is a phenomenon in which a magnetic field leads to a change in the shape&size of ferromagnetic materials. This phenomenon was first discovered by James Prescott Joule in 1842 in iron bars. Ferromagnetic materials (or their alloys) have small magnetic domains in which atomic magnetic moments are aligned parallel to each other in the same direction. On a higher scale, those magnetic moments of the domains lead to zero total magnetisation in the material, and thus, material minimizes its potential energy [3, 4]. When a magnetic field is applied, those domains align themselves in the direction of the field and magnetostriction occurs. Magnetostriction is denoted by  $\lambda$ . The strain caused by the applied magnetic field will have a limit called saturation magnetostriction  $\lambda_s$  (see [Figure 1.1](#)). The change in shape can be contraction or extension, and known as the direct (Joule) effect. An inverse magnetostrictive effect, known as the Villari effect, can also be observed, and it describes the change in magnetic state of the ferromagnetic material due to applied mechanical stresses. These features presented a new field of research called magneto-elasticity for stimuli-responsive materials and composites. [1–6].

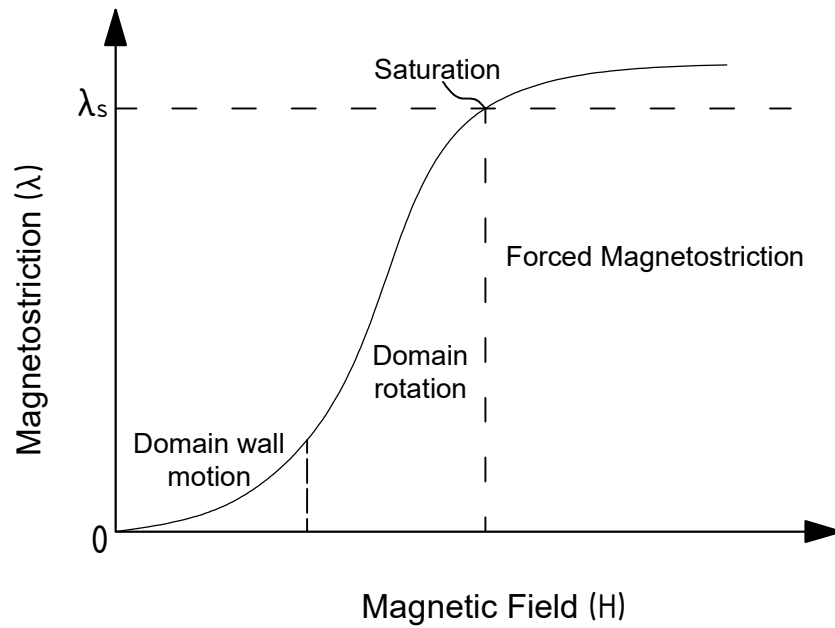


**Figure 1.1:** Typical magnetostriction curve with particular regions (schematic) [3, 7]

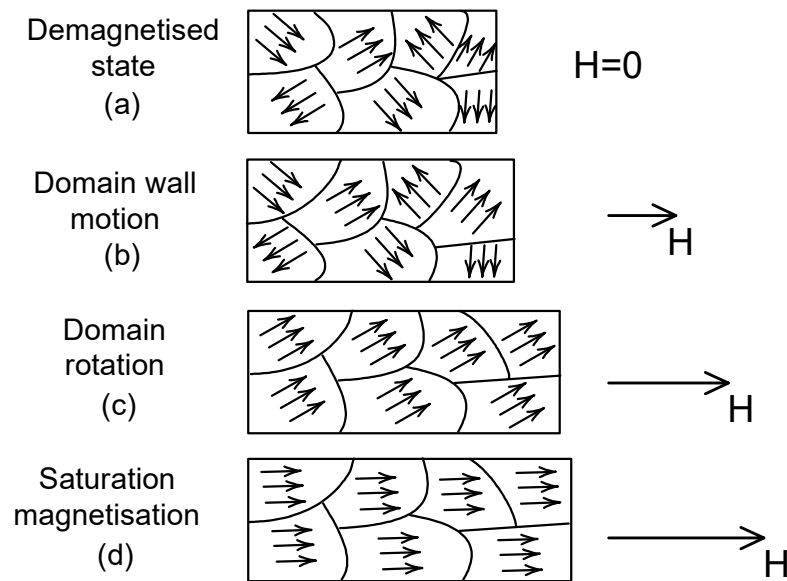


**Figure 1.2:** Representation of magnetisation process in magnetostrictive materials

The magnetic moments in the domains are oriented along one of the easy axes that are defined by crystal structure of the material. An external magnetic field will result in the domains aligned in the more energetically favourable direction with respect to the field direction. In magnetostriction of ferromagnetic materials, there are three distinct regions as shown in Figure 1.1. As mentioned, the magnetisation of the domains are randomly aligned leading to a zero net magnetisation that is energetically favourable configuration

in the demagnetised state (Figure 1.2a). These magnetic domains are separated by boundaries called domain walls that are thin transition regions. When a low magnetic field is applied, domain walls motion occurs in which resulting in growth of the magnetic domains initially aligned favourably in the applied field direction (Figure 1.2b). Hence, there will be small magnetostrictive strains in the first place at low fields and this is mostly because of domains's wall rotation that needs the least energy. Increasing the field causes the rotation of the domains's magnetisations to an easy axis that is the nearest to the applied field (Figure 1.2c). In this region, there will be a steep increase in magnetostrictive strain due to rotation of domains, and this part presents a relatively linear region that governs most of the applications. Finally, material will reach to saturation in which magnetisation vectors are oriented parallel to the field direction (Figure 1.2d) and last region will present forced magnetostriction that has no practical interest [3, 7].

Ferromagnetic materials can be divided into two groups as soft- and hard-magnetic materials [8]. Soft-magnetic materials show negligible magnetic hysteresis, which is the remanent magnetisation in the material when the applied magnetic field is removed, and present significant changes in material properties under external magnetic field. As a consequence, they can provide significant mechanical deformations. Those changes are reversed when the magnetic actuation is removed. Hard-magnetic materials present high remanent magnetisation after switching off the external magnetic field (high magnetic hysteresis), and they can show complex deformation phenomena [8].

Magnetorheological elastomers (MREs) are one type of such responsive composites of ferromagnetic materials. They are generally manufactured by dispersion of magnetic particles or fibres in an elastomer, and the size of those solid magnetic inclusions embedded in a polymer matrix can vary from micro to centimetre. These composite materials also show a coupling between magnetism and elasticity via the magnetostriction effect [1, 2, 5, 6]. By applying a magnetic field to an MRE, the magnetic inclusions will show magnetostriction, and the polymer matrix will experience some forces due to this phenomenon. As a result, the composite material will also deform [5, 9]. Monolithic form of the ferromagnetic materials (or their alloys) generally show the largest magnetostrictive response compared to their composite forms (i.e. MREs), however, polymer-bonded magnetic particles can have some advantages over the monolithic counterparts. For instance, the required/desired geometry (see Figure 1.3) can be created or resistivity and durability of the magnetic materials can be increased [3, 10, 11]. Besides, several disadvantages (due to the brittleness of some types of magnetostrictive materials) can also be improved [3, 11–14]. Magnetorheological fluids

---

(MRFs) are another type of well-known soft smart materials. In contrast to MREs, MRFs consist of magnetic particle suspensions in a carrier liquid, thus they show a liquid state that can be turned into a semi-solid state when the external magnetic field is applied [15].

In the context of this study, MREs will be the subject of research, and a magneto-elastic composite material will refer to as MREs unless otherwise stated.



**Figure 1.3:** Examples and various shapes of MREs. (Reprinted with permission. ©K. Dobberke for Fraunhofer ISC, 2018)

Magneto-elastic coupling phenomenon proposes a variety of potential applications in many engineering fields, including actuators, sensors, vibration isolation and control, sensing of ultrasonic waves, micro beams/plates in micro-electro-mechanical systems and health monitoring [1, 2, 5, 6, 8, 16–20]. A comprehensive review has been provided by Bastola et al. [19] for applications, and recent progress about MREs by also covering the fabrication processes, widely used materials for matrix, particle and additives in such composites. As stated, the most extensively studied and presented applications are shock and vibration isolators/absorbers, in addition to some other applications such as dampers, sandwich beams, actuators and sensors. Bastola and Hossain [20] also presented the current state of art for shape-morphing (bending, twisting, jumping, crawling) magnetoactive soft polymers with an extensive review focusing on material selection, fabrication methods, programming and actuation techniques. They also provided a very useful categorisation of the applications in terms of scale-wise classification namely macro-, mili-, micro- and nano-scale applications.

Böse et al. [15] have studied the relationship between the viscoelastic properties and the

composition of MREs under external magnetic field. They also manufactured ring-shaped MREs to study different actuation types for possible applications such as a pumping device, proportional valves and locking devices. Sun et al. [21] proposed a semi-active mass damper made of multilayered MREs and steel structures. It was shown that the shear modulus of MRE damper can be controlled by an external magnetic field, and vibrations can be suppressed. They concluded that MRE based mass damper can alter its natural frequency for different earthquakes. Besides MREs, MRFs are also used as adaptive vibration dampers, controllable shock absorbers, and seat dampers in automotive industry [15].

Application of MREs has initially emerged in material sciences and actuators, but the concept is now being used in the biomedical field. Potential medical applications of these materials including targeting cells, molecule separation, controlled drug release, shape memory polymers, rupture of a capsule are promising and advanced examples of MRE applications [1, 16, 20, 22, 23].

Despite being mostly laboratory-based prototypes, it was also reported that some potential future applications of magnetoactive soft materials such as controlled drug delivery, micro soft robotics, artificial muscle and invasive surgery are also being motivational for researches [20]. An in-depth and instrumental review has been given by Kim and Zhao [23] by addressing the recent progress, challenges and future aspects for soft magnetic materials specifically in biomedical and robotic applications. Besides conventional fabrication techniques, 3D/4D printing is relatively a new fabrication technique in magneto/electro-responsive polymers proposing some advantages such as single-step production, creation of complex geometries and specifically tailored devices for users [20, 22]. The details, types and recent progress about 3D/4D printing techniques have been reviewed by Yarali et al. [22] in addition to current and future applications of magneto/electro-responsive materials in biomedical field particularly.

Furthermore, there are various static and dynamic testing methods (i.e. uniaxial tension, compression, shear, bi-axial and forced vibration etc.) and experimental studies for the magneto-mechanical characterisation of MREs in the literature. Although the testing conditions and materials used in MREs differ in those studies, some general trends can be observed as summarized in the work of Bastola and Hossain [24]. Moreover, the authors suggested several standardisation ideas for magneto-mechanical characterisation of MREs, test setups and testing device settings to address the need of testing protocol for MREs.

Various soft-magnetic materials such as Terfenol-D, cobalt ferrite, certain earth metals and iron alloys can be used as magnetic filler with several alternatives of elastic matrix such as natural rubber, silicone rubber, vinyl rubber or polyurethane [1,6,25,26]. Terfenol-D and silicone rubber are commonly used elastomer matrix and magnetic material due to the simplicity of the preparation of the composite and the potential of very high magnetostrictive response [15]. For this reason, Terfenol-D will be of particular interest as a magnetic material here, and more details will be covered for this material in the following sections.

## 1.1 Magnetorheological elastomers with Terfenol-D

In 1970s, it was reported that an alloy of rare earth metals can achieve higher magnetostriction strains at room temperatures compared to pure metals that show low magnetostriction. This material was named Terfenol-D ( $\text{Tb}_x\text{D}_{1-x}\text{Fe}_y$ ), and it is an alloy of rare earth elements terbium (Ter), iron (Fe), and dysprosium (D) developed in naval ordnance laboratory (NOL) in US [3,27].

Terfenol-D is called as a giant magnetostrictive material since it is able to show high saturation strains in a range of 1000-1500 ppm [11,27,28]. Currently, the saturation strain of Terfenol-D is the largest known at room temperatures. This material can be manufactured in different forms such as powder, fibers, rods and films depending on the purpose/application (see [Figure 1.4](#) and [Figure 1.5](#) for frequently used fiber and powder forms). Moreover, the sizes of Terfenol-D can change from  $\mu\text{m}$  to  $\text{cm}$  depending on the form [3,4,28]. Mechanical stress and magnetic conditions are influential parameters on the material properties of Terfenol-D in addition to its crystal structure. Therefore, material properties and some characteristics such as the saturation magnetostriction, elastic properties, piezomagnetic coupling, and magnetic permeability differ widely as reported in the literature [4,13,27,28]. Terfenol-D is a brittle material with low tensile strength, it has a cubic crystal structure which leads to high anisotropy in magnetostriction [3,13].

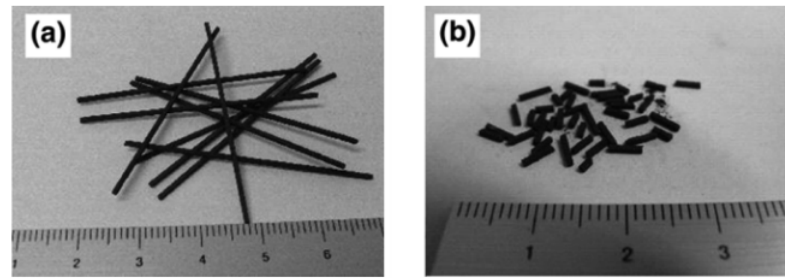


**Figure 1.4:** Long (a) and short (b) fibres of Terfenol-D. (Reprinted, with permission, from Lo et al. [28]. ©2006 IEEE)

Combining Terfenol-D particles or fibres with a polymer can lead to a decrease in maximum magnetostriction (saturation strain) and magneto-elastic coupling coefficient compared to a monolithic form of Terfenol-D. However, preferred or desired shape can be given to the composite and limitations due to brittleness can be improved as stated before. Furthermore, low resistivity of Terfenol-D causes Eddy current losses at high frequencies, but a polymer matrix can create insulating phase between the Terfenol-D particles and reduce the losses [3, 10, 12]. Therefore, MREs consisting of Terfenol-D material as the magnetic constituent have become promising and well studied type of MREs due to those advantages and being highly responsive.

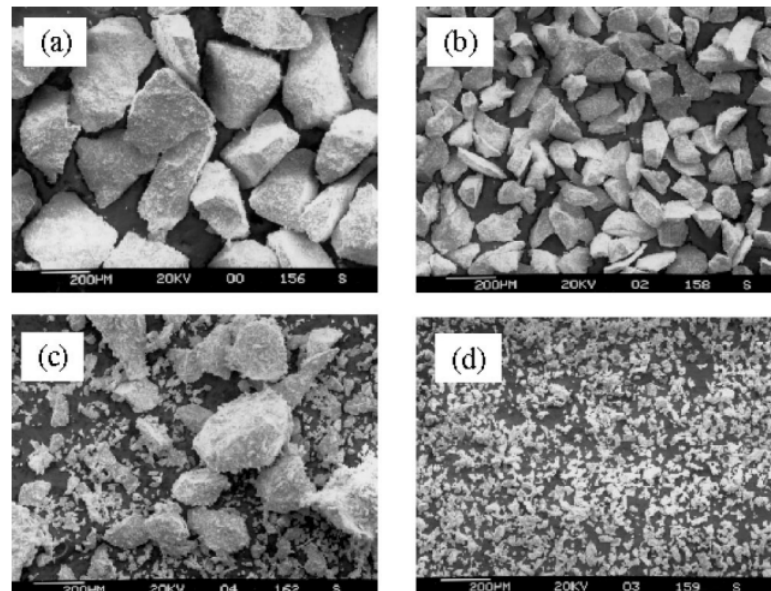


**Figure 1.5:** SEM images of Terfenol-D particles with various distributions (a) 250–300, (b) 90–106, (c) <300, and (d) <45  $\mu\text{m}$ . (Reprinted from Duenas and Carman [29], with the permission of AIP Publishing.)

Mech and Kaleta [27] have shown the positive correlation between the volume fraction ( $V_f$ ) of Terfenol-D powder (maximum of 70%  $V_f$ ) and magnetostrictive response of the composite. Further, they observed the difference in magnetostriction between bulk Terfenol-D and polymer-bonded composite. Although the composite has shown smaller magnetostriction compared to bulk form as expected, it still presented tens of times larger response than traditional magnetostrictive counterparts such as iron, nickel and cobalt. For this reason, Terfenol-D can be a preferable option over those magnetic materials in MREs. Moreover, Rodriguez et al. [10] have studied magnetostriction of polyurethane elastomer/Terfenol-D composites. They have demonstrated that samples with 50% wt aligned Terfenol-D particles (anisotropic samples) can reach  $\approx 800$  ppm of magnetostriction which is a promising value for magnetic actuators. In their later study, Rodriguez et al. [11] also observed that composites with larger Terfenol-D particles and narrower particle size distribution exhibit greater magnetostriction around 1350 ppm.

In addition to particulate Terfenol-D composites, Lo et al. [28] studied the magnetostriction of epoxy-bonded short and long (continuous) Terfenol-D fibres with a volume fraction of 50%  $V_f$ . It was seen that continuous fibre configuration of the composite exhibited larger magnetostriction ( $\approx 1300$  ppm) than all other forms (particulate, short fibre) including monolithic Terfenol-D. The reason for this interesting and significant improvement was attributed to a high aspect ratio for better stress transfer from fibres to polymer matrix, positioning the magnetic material in the direction of highly magnetostrictive crystallographic axis, and residual compressive stresses occurred in the fibres during the curing process. Similarly, Altin et al. [30] manufactured composites consisting of crystallographically aligned Terfenol-D fibrils (with different volume fractions) in vinyl ester epoxy. In this study, static properties of the composites such as Young's modulus, magnetic permeability, and piezomagnetic coupling coefficient were analysed. They also observed that crystallographically aligned Terfenol-D composite with 49%  $V_f$  of inclusions can have a coupling coefficient approximately 75% and magnetostriction roughly 90% of monolithic Terfenol-D.

In some applications of monolithic Terfenol-D and its composites, it was observed that a pre-stress can increase the saturation strain and piezomagnetic coefficient of the material along the direction of external magnetic field. This behaviour can be explained by the rotations of the magnetic domains from their initial states due to pre-stress. In other words, a compression pre-stress applied to Terfenol-D causes an increase in the number of domains aligned unfavourably with respect to applied field direction, and thus more

domains can be aligned along the field direction resulting in higher magnetostriction [3, 4, 7]. Kaleta et al. [14] studied the influence of pre-stress on the magnetostriction, and observed that pre-stress is less influential for the composite compared to monolithic Terfenol-D. Moreover, Ran et al. [12] proposed a non-linear magneto-elastic coupled model considering the effect of pre-stress for polymer-bonded Terfenol-D composites. This model was able to predict the saturation magnetostriction of the composite accurately by showing good agreement with the experimental results.

## 1.2 Particulate MREs and influential parameters in magneto-elastic behaviour

In magnetic particulate composites, the particle distribution plays a significant role in the magnetostriction of the composite material, as well as size, shape and volume fraction of the particles. On a macro-level, MREs can be categorised as isotropic or anisotropic according to the particle distribution in the polymer matrix (see Figure 1.6 and Figure 1.7). In manufacturing process, polymer and particles are mixed mechanically with some additives, and then the mixture is cured with or without magnetic field to obtain anisotropic or isotropic MREs, respectively. For the anisotropic case, dipolar moments are induced to magnetic particles when external magnetic field is applied, and this results in forming chain-like columnar structures of particles in the matrix [31].

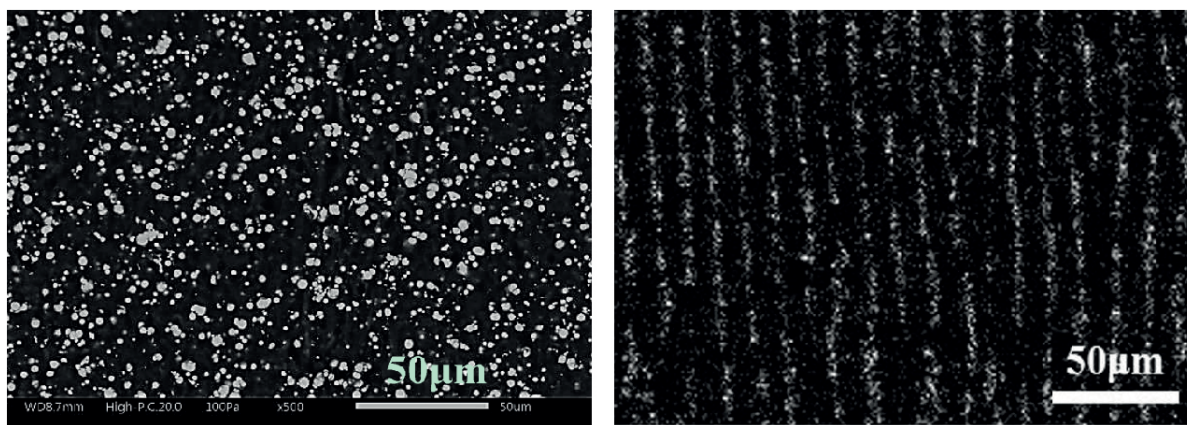


**Figure 1.6:** SEM images of isotropic and anisotropic polymer-bonded Carbonyl Iron (CI) powder composites (Reprinted from Khairi et al. [32] and An et al. [33] respectively, with permission from Elsevier)

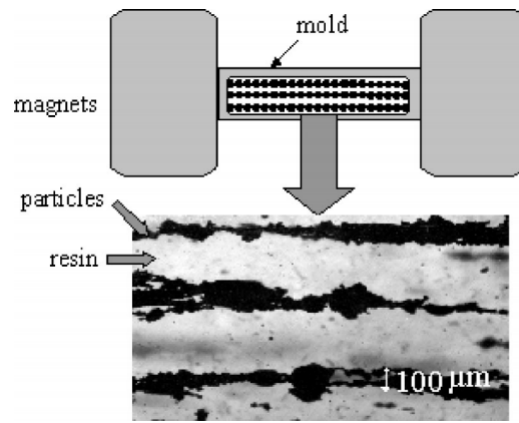


**Figure 1.7:** Anisotropic polymer-bonded Terfenol-D composite. (Reprinted from Duenas and Carman [29], with permission of AIP Publishing)

Various studies have shown that anisotropic MREs propose larger magneto-elastic response and they can have more functionality compared to isotropic counterparts [29, 32]. However, some difficulties can emerge during the fabrication, i.e. high intensity of external magnetic field is needed during cross-link process or thickness of MRE can be limited due to sharp decrease in magnetic flux density in the MRE [34]. In both types of MREs, high permeability, high magnetic saturation and low residual magnetisation are the preferable and desirable features for the magnetic particles in the elastomers to reach stronger magnetostriction effects [1, 6, 26, 35].

There are several reviews on the fundamentals of MREs, their production, modelling and applications in the literature. Thévenot et al. [1] and Filipcsei et al. [2] have treated magnetic responsive polymer composites (MRPCs) by covering different types of MRPCs, fabrication methods, detailed examples, the preparation steps and used products. Elhajjar et al. [5] evaluated the literature on magnetostrictive polymer composites (MPCs) after 2000 and presented progress and the current state of those materials. Some examples of different compositions (such as cobalt ferrites, Terfenol-D alloys and carbonyl iron) and their properties have been discussed in this review. Moreover, an overview from Ekrem et al. [9] explained how magnetostriction occurs and measurement techniques of this phenomenon. The advantages and disadvantages of the measurement procedures were compared to conclude the most common and sensitive methods.

In Newnham's nomenclature, composite materials consist of randomly distributed and oriented particles in a matrix are called [0-3] type composites. Besides, composites with fibres or particle chains in a direction embedded in the matrix are called [1-3] type [3]. In the literature, it is also possible to name isotropic and anisotropic MREs with their

corresponding [0-3] or [1-3] type, respectively. Duenas and Carman [29] conducted an experimental study for [1-3] type composites including Terfenol-D particle chains since they were expected to provide more responsive behaviour compared to [0-3] type even for the lower volume fractions. The higher magnetostrictive response in [1-3] type composites was attributed to crystal orientation of the Terfenol-D particles along the easy axis. They also studied the influence of particle size and distribution on the magnetostrictive response of the MREs. It was reported that decrease in particle size results in an increase in demagnetisation effects, thus the strain response of the composite is reduced. Moreover, Winger et al. [36] studied the dependency of the magnetorheological effect on the particle size fraction, and demonstrated that there is a correlation between larger particle size and magnetorheological effect.

Besides particle size and distribution, volume (and weight) fraction of the magnetic particles is also an important parameter in magneto-elastic response. Bellelli and Spaggiari [37] performed compression tests and three-point bending experiments on the isotropic and anisotropic MREs with or without external magnetic field. A phenomenological model has been developed to predict the mechanical response of MREs subjected to compressive stress. They concluded that weight fraction of the magnetic particles is the most influential parameter on the specimen behaviour in their experiments. Moreover, Li and Zhang [38] proposed an experimental and theoretical model, where an optimum volume fraction was calculated for magnetic particles that leads to an improvement in magnetorheological effects.

The temperature is another influential parameter on the properties and behaviour of the MREs since the polymer materials are used as matrix phase. Wen et al. [39] studied static and dynamic mechanical properties of anisotropic MREs under different temperatures. It was shown that temperature increase causes a decrease in initial modulus and magnetic-induced modulus due to rotation of particle chains in the polymer matrix.

In addition to using only one type of magnetic particle in MREs, different compositions of magnetic inclusions can also be used simultaneously. Furthermore, some non-magnetisable particles can also be added to MREs for some special purposes. These type of MREs are called hybrid MREs, and this feature can lead to an optimisation of the magneto-elastic performance. Borin et al. [40] investigated the mechanical stress that results from the magnetostriction of hybrid magneto-elastic materials. In the experimental setup, two different types of magnetic particles: CI powder (soft) and NdFeB (hard) were used with a polymer host (PDSM silicone). They observed an increase in magnetostriction

for hybrid form compared to those consist of only soft-magnetic CI particles.

Moreover, an experimental and computational characterisation of ultra-soft hybrid MREs consisting soft and hard magnetic particles has been given by Mateos et al. [8] to study the influence of different mixing ratios and the role of soft/hard particles on the magneto-mechanical performance. From the numerical results, it was suggested that soft magnetic particles lead to an amplification of the magnetisation while the hard magnetic particles contribute the actuation modes. It was also shown that hybrid MREs present enhanced stiffening under an applied magnetic field which is almost 1.5 and 4 times larger than MREs consisting only soft or hard magnetic particles, respectively. Burgaz and Goksuzoglu [34] also manufactured and studied isotropic hybrid MREs with the combinations of carbon-black, carbonyl iron powder (CIP) and bare iron powder (BIP) for dynamic applications. They pointed out high magnetic particle concentration results in aggregation of those particles which leads to undesirable properties such as very high damping ratio and low tensile strength for dynamic applications. Using carbon-black can prevent those issues by increasing filler-matrix interaction and improving mechanical properties.

Finally, another experimental study have been carried out by Bastola et al. [26] for MREs. They presented an innovative fabrication method and demonstrated that 3D printing can also be used to create anisotropic MREs without the need to use an external magnetic field. This study presents a new type of MRE manufacturing method, and it has been observed that some printing parameters, such as feed rate, extrusion pressure, and initial height have a significant effect on the properties of the MREs. In the experiments, it has been shown that damping capacity and dynamic stiffness of the 3D printed MREs could be tuned by applying a moderate external magnetic field.

## 1.3 Magneto-elastic modelling

After their introduction, researchers have conducted various experimental studies for MREs, and also developed theoretical and numerical models to investigate the behaviour of these composites.

Thus, besides experimental works, computational modelling of MREs has also been instrumental in the understanding of the behaviour, optimising the designs and exploring the potentials of these composites. Mechanical model of a composite material can be created by following two distinct approaches called macroscopic and microscopic approach.

In macroscopic approach, a mechanical model is established based on the empirical data that characterise the material behaviour (see Figure 1.8a). Consequently, the detailed description of materials such as geometrical and constitutive properties of the all components is not necessary in this approach. On the other hand, microscopic approach is built on the detailed definition of internal structure by considering the components' own constitutive response and geometry (see Figure 1.8b) [41, 42]. Microscopic or macroscopic modelling approaches can also be called as a mono-scale approach due to considering the composite material on one level (scale).

Alternatively, a third combined approach known as multi-scale approach, in which various scales are analysed simultaneously, can be used (see Figure 1.8c). The multi-scale approach considers material on the microscopic level to reflect the real structure of heterogeneous material, and the macroscopic level to model the material as homogeneous with *effective* properties. As mentioned, the geometrical configuration and constitutive properties of the each component are not taken into account *explicitly* on a higher level (macro-scale). Conversely, lower level (micro-scale) models the material as a heterogeneous medium by considering each component's configuration and constitutive properties *explicitly* [41–44]. In the following chapters, a multi-scale approach will be presented for an MRE material, and more discussion on mono- and multi-scale approaches will be provided.

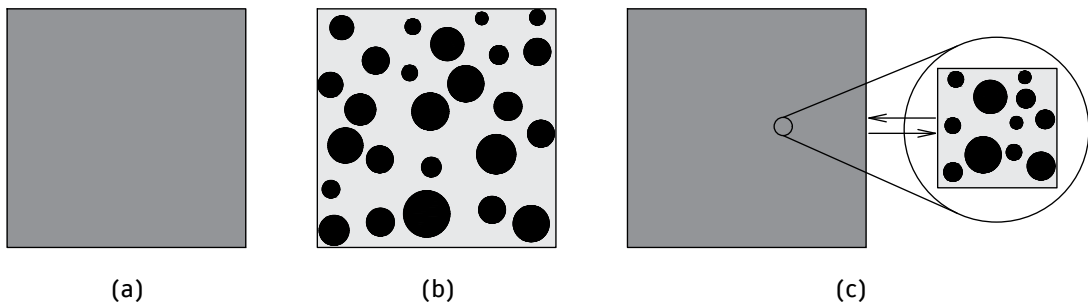


**Figure 1.8:** Different approaches. Macrostructural (a), microstructural (b) and Multi-scale approach (c)

### 1.3.1 Macro-scale modelling in magneto-elasticity

Several macroscopic material models have been developed for MREs. A macroscopic model has been proposed by Attaran et al. [45] to capture the mechanical deformation. The authors have simplified a previously developed continuum model for this reduced form, and it was reported that this reduced model shows good agreement with the experimental

results. Raikher and Stolbov [46] have followed a continuum approach for MREs by considering them as a homogeneous elastic and isotropically magnetisable medium. Despite some limitations and drawbacks, the model is able to reproduce experimental results with acceptable accuracy. Besides, Akbari and Khajehsaeid [47] have developed a continuum model for MREs with finite strains that takes the influence of magnetisation into account by directly introducing to material shear modulus. They showed that this model can simplify the constitutive model and considers the magnetic saturation in MREs.

Dorfmann and Ogden [48] studied constitutive relations for isotropic magneto-sensitive (MS) elastic continua by using the electromechanical and thermomechanical theories. After appropriate simplifications for such a material, they used their material model to address axial shear behaviour of a circular cylindrical magneto-sensitive tube under an applied magnetic field. The results showed that magnetic field leads to an increase in shear stiffness of the material. Brigadnov and Dorfmann [49] modelled MS elastomers as a moving non-polar deformable continuum in an electro-magnetic field. They considered the MS material as hyperelastic and derived the constitutive equations to study shear deformation of a rectangular shaped MS elastomer confined by parallel plates at the top and bottom. By applying a magnetic field normal to the plates, it was also shown that the influence of magnetic field was to stiffen the shear response of the MS material.

Further, Bustamante [50] developed a theoretical basis for non-linear transversely isotropic magneto-active elastomers based on the non-linear magneto-elastic theory provided by Dorfmann and Ogden [48, 51] used for only the isotropic magneto-elastic solids. By using the results of two basic problems (simple shear of a slab, simple tension of circular cylinder) and available experimental data, a prototype constitutive model was provided to give the closed-form solutions of some boundary value problems. Another model for anisotropic non-linear MRE bodies has been given by Shariff et al. [52] by introducing a new set of spectral invariants in total energy function. They showed that this form of energy function with novel spectral invariants is more general, presents simpler expression for the total stresses (in classical homogeneous and non-homogeneous problems) and has an experimental advantage.

Moreover, Saxena et al. [53] pointed out that magneto-elastic materials are naturally viscoelastic since they are generally polymer based, and the response of the material to an external magnetic induction is not perfectly instantaneous for all materials. The magnetic field developed in the material will not be constant, but start from a non-equilibrium value and approach to equilibrium in a finite time. Since these features are

significant factors in designing MRE actuators, they presented a mathematical modelling of magneto-viscoelastic behaviour by combining magneto-elastic theory (given by Dorfmann and Ogden [51]) and theory of mechanical viscoelasticity to consider magnetic and mechanical dissipation effects appropriately. Following this study, Saxena et al. [54] extended the proposed non-linear magneto-viscoelastic modelling to anisotropic MREs. In this model, an additional deformation gradient and a magnetic induction are considered in the direction of particle chains. By following the previously developed ideas and further decomposition of free energy function, they proposed physically reasonable and thermodynamically consistent free energy density functions and evaluation laws to address the problems such as stationary pure shear, time dependent strain and magnetic induction.

Similar to MREs, magneto-electro-mechanical soft materials are also promising candidates for several advanced applications such as magneto-electric random access memory, wireless energy harvesting and non-volatile memories. Bustamante et al. [55] proposed mathematical framework to obtain constitutive equations of non-linear magneto-electric soft materials at finite strains. With this model, they studied different homogeneous and non-homogeneous boundary value problems.

Furthermore, Haldar et al. [56] proposed the finite element implementation of rate-dependent (under time dependent mechanical and magnetic loadings) response of MRE materials by capturing the saturation effects in magnetostriction. Dadgar-Rad and Hossein [57] have also proposed a viscoelastic formulation for the time dependent analysis of soft materials consisting hard-magnetic constituent. Numerical examples given for 2D soft beams showed that the results of this model can be validated by previously reported results in case of purely elastic deformations. Following this validation, the authors studied the creep response of the beams in case of viscoelastic deformations and investigated the influence of viscoelastic parameters such as relaxation time and long-term shear modulus.

### **1.3.2 Micro-scale modelling in magneto-elasticity**

Microscopic material models have also been presented for MREs. Wood and Camp [25] presented a microscopic model to study the relationship between features of the microstructure and physical properties by using Monte Carlo computer simulations. It was shown that the elastic modulus can be controlled by applying a uniform magnetic field to the samples at the gel-formation stage. Another microscopically motivated approach has been proposed by Kalina et al. [35] to study the deformation behaviour of isotropic

and anisotropic MREs. Moreover, Moreno-Mateos et al [8] provided a detailed experimental characterisation and multi-physics microstructural computational approach for Hybrid MREs consisting of soft- and hard-magnetic particles together. It was shown that combination of soft- and hard-particles can have some functionalities such as stiffening, amplification of the magnetisation and torsional actuation.

Besides, a novel modelling approach has been proposed by Ethiraj and Miehe [58] for MREs with a constitutive formulation considering two microscopic fundamental properties namely the energy of magnetized inclusions and the elastic energy of polymer phase. By taking into account the dipole-dipole interactions, the presented model was used to solve several types of application-motivated boundary value problems such as spherical MRE sample, a finger actuator and ring shaped actuator in a valve. Further, Gonzales and Hossain [59] developed a continuum model by following a microstructural-based approach and considering the viscoelastic nature of the MREs. In this novel model, the influence of distribution of the particles has been considered in three main groups namely isotropic, perfectly aligned chain and wavy chain cases by also capturing the rate dependent, non-linear magneto-mechanical response of the materials.

### 1.3.3 Multi-scale modelling in magneto-elasticity

Multi-scale analysis have been also used by researches in magneto-elastic modelling. Various strategies can be followed in multi-scale analysis, and they can be categorized into two main groups as analytical continualisation or homogenisation and computational homogenisation techniques.

In the computational homogenisation technique, an explicit constitutive equation is not described on the macro-level. Instead, a constitutive relation is obtained implicitly from the macro-micro-macro connection. This connection is carried out via transferring of the macro-level strains to the micro-level as displacement boundary conditions and then solving a boundary value problem. Hereafter, reaction forces obtained from this problem are transformed as stresses to the macro-level by using a homogenisation technique [41]. Alternatively, analytical techniques may be preferred. The difference of this technique is having explicit constitutive equations on the macro-level. Here, a heterogeneous material model (continuum or discrete) is used at the lower scale, and boundary value problems are solved. These solutions are translated into the effective properties. Material is assumed to be homogeneous on the macro-level, and the constants in constitutive relations in the

macrostructure appear in the form of those effective properties [41, 42].

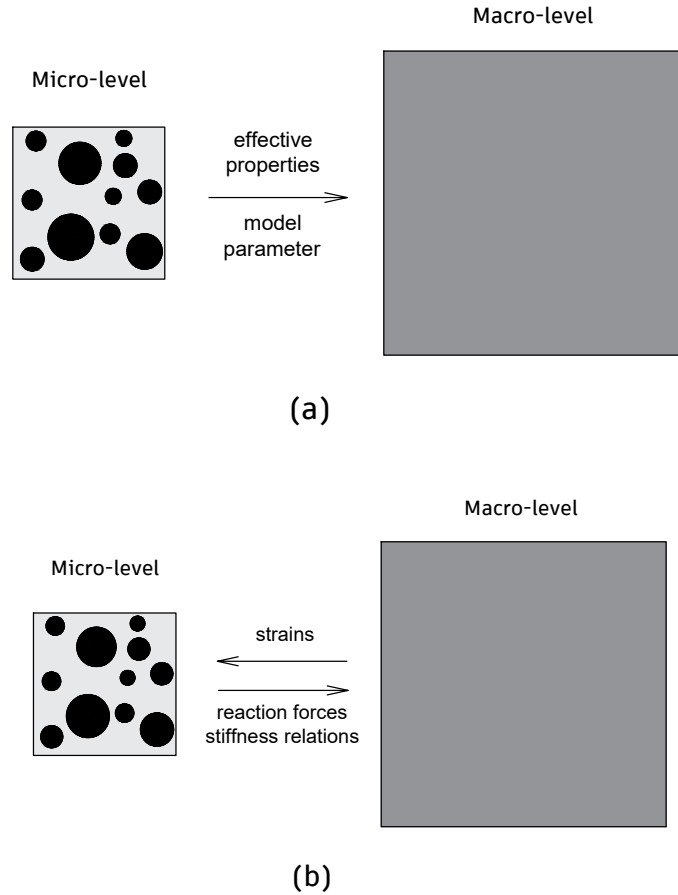


**Figure 1.9:** Analytical (a) and computational (b) homogenisation representation

In addition to macroscopically and microscopically motivated models, non-local continuum theories have been extended to magneto-elasticity by researchers to include the information from the micro-level to the macroscopic continuum via additional material constants such as length-scale parameters [60–63]. Xu et al. [61] have extended the theory to magneto-elasticity, and derived macro-level magneto-elastic constitutive relation enriched with higher order terms accompanied by characteristic length-scale parameters. Ke et al. [62] investigated the free vibration of magneto-electro-elastic nanoplates based on Eringen’s non-local theory, and they showed that the non-local parameter and the natural frequencies are inversely proportional. Besides free vibration, non-local bending and buckling behaviour of a size dependent plate model have been given for magneto-electro-thermo-elastic nanoplates by Gholamo et al. [60]. It was shown that non-local theory always predicts smaller critical buckling load and natural frequencies than those from the classical theory in the nanoplate. Non-local strain gradient theory has been used by [63]

to analyse the static bending behaviour of a sandwich nanoplate consisting of a FGM core and piezomagnetic face sheets. They presented that an increase in strain gradient parameter results in an increase in stiffness, and thus the displacements are decreased.

Zabihyan et al. [64] have followed a multi-scale approach by using fully-coupled finite element method with computational homogenisation procedure to obtain the response of MRE at the macro-scale. The effects of different microstructures have been studied, and it was shown that microstructure type and boundary conditions on micro-level has a significant influence on the macroscopic response. Further, Kalina et al. [65] have presented a macroscopic model for MREs by using a computational homogenisation technique. Various geometries and different volume fraction of magnetic particles have been investigated, and magnetostrictive response of the macroscopic MRE was determined by considering the underlying microstructure.

Moreover, Galipeau et al. [66] studied the effective macroscopic behaviour of magnetoactive materials and the influence of the microstructural properties such as particle concentration, shape, distribution and deformation. Finite element models and a theoretical homogenisation framework have been presented to investigate the behaviour of periodic (rectangular and quasi-hexagonal) and random microstructures. On the macroscopic scale, the total forces in the magnetoactive composite resulted from the applied magnetic field and total magnetostriction have been analysed. It was concluded that the microstructure of a magnetoactive composite has a significant role in optimizing the macroscopic magneto-elastic performance of such composites. Another multi-scale approach has been proposed by Javili et al. [67], and the connections between micro- and macro-level variables have been established by using a geometrically nonlinear homogenisation scheme for MREs at finite strains. On the micro-level unit cell, periodic boundary conditions have been considered and finite element method has been used to compute the macro-level field variables and tangent modulus. Two and three dimensional numerical examples under simple shear and simple extension loading conditions have been addressed in this model.

### 1.3.4 Representative volume element

In the multi-scale analysis, a Representative Volume Element (RVE) concept is typically used to analyse materials on the micro-scale in both analytical and computational homogenisation techniques. Here, an RVE is the smallest specimen of a material, which

is large enough to be constitutively valid. Therefore, the RVE must be satisfactorily smaller than macroscopic dimensions, but it must have sufficient information about the microstructure [41]. Generally, the existence of the RVE is assumed and its size is prescribed in applications. In literature, several definitions have been made on the RVE, and different procedures have been given in order to determine the size of an RVE for different engineering materials [68–71]. Some commonly accepted views are to associate the size of RVE with the largest inclusion particle size, number of grains or diameter of reinforcement in the heterogeneous material [71–74]. In addition to these different procedures, a systematic approach has been presented by Gitman [41] to determine the RVE size in quasi-brittle materials.

Metsch et al. [75] have modelled a range of RVEs based on a microscopically motivated continuum approach to investigate microstructural interactions. By applying varying amplitudes of the magnetic field, deformation of the isotropic and anisotropic RVE samples has been analysed for different volume fractions of the magnetic particles. This model is capable of describing magnetostriction by showing good agreement with the experimental results in the literature. Sun et al. [76] have proposed another RVE approach to investigate the effective mechanical properties of anisotropic MREs under plane stress conditions. The influence of some parameters such as magnetic field intensity, particle diameter and distance between the particles were examined and resulted in a positive correlation between shear modulus and field intensity/particle diameter, and inverse proportionality to the distance between the particles.

## 1.4 Piezomagnetism

Magnetostrictive materials exhibit non-linear material behaviour, but magnetostriction can be modelled as a linear behaviour in a certain range of operation. This linear magnetostrictive phenomenon follows piezomagnetic laws, and it can be obtained by considering only the variations around initial bias conditions including a magnetic field and mechanical pre-stress. In a static magnetic field (curl-free), the constitutive equations of a linear piezomagnetic medium in classical continuum theory are described as [18, 77–82]

$$\sigma_{ij} = C_{ijkl}^H \varepsilon_{kl} - q_{kij} H_k \quad (1.1a)$$

$$B_i = q_{ikl} \varepsilon_{kl} + \mu_{ik}^\varepsilon H_k \quad (1.1b)$$

where  $\boldsymbol{\sigma}$  and  $\boldsymbol{\varepsilon}$  are the stress and strain tensors,  $\mathbf{B}$  and  $\mathbf{H}$  are magnetic induction and magnetic field vectors.  $\mathbf{C}$  is the stiffness tensor for constant magnetic field and  $\boldsymbol{\mu}$  is the magnetic permeability tensor for constant strains, and  $\mathbf{q}$  is the piezomagnetic coupling tensor. Constitutive equations can be written in matrix form as shown below

$$\begin{bmatrix} \sigma_1 \\ \sigma_2 \\ \sigma_3 \\ \sigma_4 \\ \sigma_5 \\ \sigma_6 \\ B_1 \\ B_2 \\ B_3 \end{bmatrix} = \begin{bmatrix} C_{11}^H & C_{12}^H & C_{13}^H & C_{14}^H & C_{15}^H & C_{16}^H & -q_{11} & -q_{21} & -q_{31} \\ C_{21}^H & C_{22}^H & C_{23}^H & C_{24}^H & C_{25}^H & C_{26}^H & -q_{12} & -q_{22} & -q_{32} \\ C_{31}^H & C_{32}^H & C_{33}^H & C_{34}^H & C_{35}^H & C_{36}^H & -q_{13} & -q_{23} & -q_{33} \\ C_{41}^H & C_{42}^H & C_{43}^H & C_{44}^H & C_{45}^H & C_{46}^H & -q_{14} & -q_{24} & -q_{34} \\ C_{51}^H & C_{52}^H & C_{53}^H & C_{54}^H & C_{55}^H & C_{56}^H & -q_{15} & -q_{25} & -q_{35} \\ C_{61}^H & C_{62}^H & C_{63}^H & C_{64}^H & C_{65}^H & C_{66}^H & -q_{16} & -q_{26} & -q_{36} \\ q_{11} & q_{12} & q_{13} & q_{14} & q_{15} & q_{16} & \mu_{11}^\varepsilon & \mu_{12}^\varepsilon & \mu_{13}^\varepsilon \\ q_{21} & q_{22} & q_{23} & q_{24} & q_{25} & q_{26} & \mu_{21}^\varepsilon & \mu_{22}^\varepsilon & \mu_{23}^\varepsilon \\ q_{31} & q_{32} & q_{33} & q_{34} & q_{35} & q_{36} & \mu_{31}^\varepsilon & \mu_{32}^\varepsilon & \mu_{33}^\varepsilon \end{bmatrix} \begin{bmatrix} \varepsilon_1 \\ \varepsilon_2 \\ \varepsilon_3 \\ \varepsilon_4 \\ \varepsilon_5 \\ \varepsilon_6 \\ H_1 \\ H_2 \\ H_3 \end{bmatrix} \quad (1.2)$$

via the Voigt notation.

In the literature, it is possible to see different forms of piezomagnetic constitutive equations. Soh and Liu [79] have presented different forms of magneto-electroelastic constitutive equations and their thermodynamic potentials. Although they provided the forms for magneto-electroelastic solids, magneto-elastic (or piezomagnetic) forms can be reduced from those. They also presented the relationship between the material constants in different forms. Two most commonly used forms in the literature and the relations between the constants have been given in Table 1.1. In this thesis, the form given in Eq. (1.1) with the independent variables  $\varepsilon$  and  $H$  will always be adopted. For the ease of readability, quantities in piezomagnetic constitutive equations in Eq. (1.1) have been summarized in Table 1.2 with their symbols and SI units.

The most common two forms	Relationship between constants
$\boldsymbol{\varepsilon} = \mathbf{s}^H \boldsymbol{\sigma} + \mathbf{d} \mathbf{H}$ $\mathbf{B} = \mathbf{d}^t \boldsymbol{\sigma} + \boldsymbol{\mu}^\sigma \mathbf{H}$	$\mathbf{s}^H = (\mathbf{C}^H)^{-1}$
$\boldsymbol{\sigma} = \mathbf{C}^H \boldsymbol{\varepsilon} - \mathbf{q} \mathbf{H}$ $\mathbf{B} = \mathbf{q}^t \boldsymbol{\varepsilon} + \boldsymbol{\mu}^\varepsilon \mathbf{H}$	$\mathbf{q} = \mathbf{C}^H \mathbf{d}$ $\boldsymbol{\mu}^\varepsilon = \boldsymbol{\mu}^\sigma - \mathbf{d}^t \mathbf{q}$

**Note:** Matrix notation is used and  $t$  denotes the transposition of a matrix.

**Table 1.1:** Relationship between constants in different forms

Quantity	Symbol	Unit
Stress	$\boldsymbol{\sigma}$ (or $\mathbf{T}$ )	N/m <sup>2</sup>
Magnetic Induction	$\mathbf{B}$	T
Strain	$\boldsymbol{\varepsilon}$ (or $\mathbf{S}$ )	-
Magnetic field	$\mathbf{H}$	A/m
Elastic compliance (Under constant $\mathbf{H}$ field)	$\mathbf{s}^H$	m <sup>2</sup> /N
Elastic stiffness (Under constant $\mathbf{H}$ field)	$\mathbf{C}^H$	N/m <sup>2</sup>
Piezomagnetic constant ( $\boldsymbol{\sigma}$ & $\mathbf{H}$ independent variable)	$\mathbf{d}$	m/A
Piezomagnetic constant ( $\boldsymbol{\varepsilon}$ & $\mathbf{H}$ independent variable)	$\mathbf{q}$ (or $\mathbf{e}$ )	N/Am
Magnetic permeability (Under constant stress $\boldsymbol{\sigma}$ )	$\boldsymbol{\mu}^\sigma$ (or $\boldsymbol{\mu}^T$ )	N/A <sup>2</sup>
Magnetic permeability (Under constant strain $\boldsymbol{\varepsilon}$ )	$\boldsymbol{\mu}^\varepsilon$ (or $\boldsymbol{\mu}^S$ )	N/A <sup>2</sup>
Scalar magnetic potential	$\varphi$	A

**Table 1.2:** Piezomagnetic terminology

## 1.5 Motivations

In the analysis of heterogeneous materials, it is known that microscopic properties affect the macroscopic behaviour of the material. Therefore, capturing microstructural information in the macroscopic continuum results in a significant improvement in accurately describing and predicting the response of heterogeneous materials. [41,42,44]. Moreover, it is well known that size-dependent phenomena (when the smaller specimen behaves stronger,

compared to a large, but geometrically proportionally similar specimen [83]) must be considered in the analysis of small size structures that have an underlying microstructure. Classical continuum formulations are not sufficient to capture those microstructural information, and atomistic dynamic approaches have some limitations such as computational cost and difficulties in precision. Therefore, non-local continuum theories have been proposed (such as strain gradient elasticity theory [84], non-local elasticity theory [85], modified strain gradient theory [86], and modified couple stress theory [87]). These theories can be considered an efficient and adequate alternative to classical continuum theories [60].

In macroscopic level, additional material parameters so-called length-scale and time-scale parameters have been introduced in non-local formulations to describe the influence of the micro-scale. In case of multi-scale analysis, the micro- and macro-scales link to each other by coupling the kinematics, stresses and forces of the two scales. In this approach, size of the considered unit cell at the micro-scale is also become a significant parameter. As mentioned, MREs are heterogeneous materials and studies have also shown that they have the dimensions from the millimetre to centimetre [26, 40]. Therefore, introduction of the microstructural information has also a significant role in the analysis of mechanical behaviour of MREs.

The above overview shows the importance of microstructural properties on the overall behaviour of MREs and, thus, the importance of capturing these microstructural properties in mechanical models. As mentioned, RVE is used to denote the unit cell that represents the micro-level in multi-scale analysis. In analytical homogenisation approaches, the unit cell (or RVE) is considered as model input; thus, the RVE size becomes a model parameter [41, 42]. It was already shown in [41, 42, 44], there is a link between the RVE size on the micro-level and additional characteristic length-scale parameter employed in non-local continua on the macro-level. Hence, the determination of the RVE size in magneto-elasticity becomes an important step since it is to be used in multi-scale analysis of MREs. This problem will be addressed in following chapters in details by presenting an RVE size determination process for an MRE material and implementation of this parameter.

It is known that the behaviour of the materials with heterogeneous structure considerably varies compared to their homogeneous counterparts especially in dynamic problems. For instance, a well-known phenomenon called stop-bands or band gaps occur due to the dispersion of the waves in heterogeneous materials with a periodic arrangement of inclusions. In this phenomenon (stop-band), elastic/acoustic waves cannot propagate and vibrations are suppressed in some frequency ranges. This type of composite materials are

called as phononic crystals (PCs), and this feature enables various potential applications such as acoustic filters, reflectors, wave guides, switches and vibration isolation [88–94]. A great deal of effort has been put on the elastic wave propagation in periodic composite materials by theoretical and experimental studies [92, 95–99].

Controlling and tuning the characteristics (e.g. position and the width) of the stop-bands and analysing the effective parameters influencing these properties are important topics to create more effective designs or enhance the functionality of the PCs. It is known that the stop-band can be influenced by inclusion geometry, lattice pattern, volume fraction and elastic characteristics of the constituents [91, 97, 99, 100]. Besides these parameters, another interesting and promising way to control the stop-band characteristics is using the responsive (smart) materials in PCs. Since the material and geometrical properties can be influenced by an external magnetic field, magneto-elastic composites are also becoming a new type of PCs in the field. In particular, contactless tunability of the stop-bands in this type of composites has been studied extensively [88–91, 99, 101–104]. It is also known that band gap predictions can be affected by randomness in material parameters [97, 105].

With these motivations magneto-elastic coupling and the randomness in geometrical properties are worthy to investigate. Hence, the influence of these parameters on the longitudinal wave propagation and stop-band frequencies will be studied in this thesis. The randomness will be introduced to size and position of the inclusions separately and simultaneously by also covering the effects of magneto-elastic coupling.

## 1.6 Outline

In this thesis, two primary aims can be distinguished as:

- Determination and analysis of a representative volume element (RVE), employed in a gradient enriched magneto-elastic model.
- Analysing the influence of microstructure and magneto-elastic coupling on the longitudinal wave propagation, in particular, appearance of stop-band frequencies.

In accordance with these aims, [Chapter 1](#) provides an overview of the background about the fundamentals of the magneto-elasticity, introduces some modelling approaches and reviews the literature for magneto-elastic composite materials.

In [Chapter 2](#), the detailed procedure of the RVE size determination for a magnetorheological elastomer (MRE) will be given. Definitions of different RVEs are presented depending on different physical phenomena in the magneto-elastic material. To determine the defined RVE sizes, a finite element implementation will be adopted to obtain a microscopic boundary value problem that will be used in the statistical analysis. After analysing the convergence of the proposed statistical method in magneto-elastic problem, the influences of mechanical, magneto-elastic coupling and magnetic permeability properties of the constituents will be studied on these model parameters (RVEs). Numerical results and discussions of two-dimensional magneto-elastic RVEs are also addressed in this chapter, since they are used as input in the next chapter.

[Chapter 3](#) deals with the identification of the phenomenological material parameters (length-scales) on the macroscopic magneto-elastic continua in terms of RVE sizes for an MRE material. By means of a multi-scale approach based on a non-local analytical homogenisation scheme, the macro-level magneto-elastic constitutive formulation is developed with additional model parameters (RVE sizes) to introduce the micro-level information to macroscopic continua. By using the RVE size determination results from the previous chapter, a two-dimensional in-plane problem is presented for the singularity removal study in mechanics and magnetic fields which is not an ability of classical magneto-elastic continuum model.

The aim of [Chapter 4](#) is to analyse longitudinal wave propagation and stop-band behaviour in magneto-elastic composite materials and to investigate the combined influence of magneto-elastic coupling and geometrical randomness in the material. The influence of the size and the volume fraction of magnetic inclusions will be studied with and without

magneto-elastic coupling. Randomness will be introduced in the magnetic inclusions' sizes and positions separately as well as simultaneously. A finite element formulation will be described that has been used to simulate magneto-elastic wave propagation. The test setup and the algorithm of analysis will be given in this chapter as well as numerical results and discussions of different test material geometries to study the effects of periodicity, randomness, particle size, volume fraction, and coupled versus decoupled behaviour.

Finally, [Chapter 5](#) and [Chapter 6](#) give the conclusions of the thesis with some closing remarks and potential future works respectively.

## Chapter 2

# Determination of representative volume element size for a magnetorheological elastomer

The aim of this chapter<sup>1</sup> is to present a numerically-statistical procedure to define and analyse the Representative Volume Element (RVE) concept for an MRE material. As discussed in the previous chapter, microstructural information needs to be taken into account in the analysis of heterogeneous materials to describe and predict the behaviour of the macroscopic continuum accurately. At this point, various approaches can be followed such as mono-scale or multi-scale procedures. This microstructural information can be introduced via material parameters: length-scale or time scale (time dependent processes) parameters in a mono-scale approach [41, 106–108]. On the other hand, an interaction between micro-level (unit cell) and macro-level (macroscopic continuum) is considered in the multi-scale approach. In a multi-scale analysis, size of the unit cell also becomes an important parameter in addition to material parameters, and RVE concept is used to describe this unit cell.

Furthermore, it was already shown that a link between model parameter: RVE size in multi-scale approach and material parameters: length- and time-scale in non-local macroscopic continua can be established [42, 43, 108–110]. Because of these reasons, it can be concluded that the RVE size of a material can have a significant role in modelling approaches. Hence, this chapter seeks to determine the RVE size for an MRE material by

---

<sup>1</sup>This chapter is directly adopted from:

S. Eraslan, I. M. Gitman, H. Askes, and R. de Borst. Determination of representative volume element size for a magnetorheological elastomer. *Computational Materials Science*, 203:111070, 2022. [81]

analysing the influence of the constituents' properties on this model parameter. A finite element implementation will be adopted to obtain a microscopic boundary value problem to be used in statistical analysis for RVE size determination. Moreover, the link between the RVE size and the length-scale parameter on macroscopic continua will be explored and extended to magneto-elastic coupling framework in details in [Chapter 3](#) for a generalised magneto-elastic continua.

## 2.1 Formulation and introduction of methodology

As introduced above, in this section, the methodology and formulation of RVE size determination problem will be presented for an MRE material. As has been explained, RVE creates the connection between micro- and macro-scales, thus it is an important parameter in accurate description of the behaviour for heterogeneous materials. In the literature, some well-known definitions of the RVE have been given by scientists. Analysing them, there are specifically two common points that can be identified in all definitions [[68](#), [69](#), [71](#), [74](#)]. These points can be summarised as:

1. on the one hand, RVE should be small enough compared to macrostructural dimensions;
2. on the other hand, it must contain adequate information about the microstructure to be considered as a representative.

After the definition, scientists attempted to determine the size of RVE for several engineering materials. For instance, Van Mier et al. [[71](#)] suggested RVE size to be at least 3 – 5 times bigger than the largest particle size for concrete samples. Lemaitre et al. [[70](#)] proposed three-dimensional RVE sizes approximately 0.1mm, 1mm, 10mm, and 100mm for metallic materials, polymers, wood and concrete, respectively. Drugan and Willis [[74](#)] related the reinforcement diameter and RVE size for reinforced elastic composite. They pointed out RVE must be twice the diameter of the reinforcement. Besides these studies, Gitman [[41](#)] have proposed an objective systematic determination process for the RVE size of concrete material, and assessed the influential parameters on both the procedure and the size. However, these studies dealt with a purely mechanical response, and the extension of the RVE size determination to a coupled physics (such as magneto-elasticity) was not addressed.

In the method proposed by Gitman et al. [111, 112], the existence of the RVE was first addressed before the introduction of the size determination by using a statistical analysis based on the mathematical expectation and standard deviation in linear-elastic, hardening and softening regimes for concrete material. It was concluded that an RVE exists in case of linear elasticity and hardening. However, an RVE cannot be found in case of softening since the material behaves differently for the increased unit cell size. In this thesis, MRE was subjected to small variations of external magnetic and mechanical stimulus around bias conditions which lead to modelling the MRE as a linear piezomagnetic material as discussed in the first chapter. Thus, it can be assumed that the material will follow the linear piezomagnetic material behaviour, and the RVE will exist and can be found in this regime for an MRE. This hypothesis will be tested further in this chapter.

Since an RVE denotes the minimum size of the microscopic cell, it can be defined as a lower bound, and it must have statistical homogeneity. This means that larger microscopic cells present similar behaviours while the smaller microscopic cells behave differently which also depicts lack of sufficient information about the microstructure.

In a conventional elastic material that does not exhibit a coupling behaviour, only one RVE related to elastic properties can be defined. However, the response of a material that shows magneto-elastic coupling will not only be mechanical, and thus there should be more than one RVE for such a material. Hence, it is assumed that an MRE has different RVEs depending on the considered phenomenon. The idea of defining different RVEs is one of the novelties proposed in this study, and this assumption has been made due to different (mechanical, coupling and magnetic) types of possible responses that can be observed in a coupling (e.g. magneto-elastic) nature. Therefore,  $V_{RVE}^{elastic}$  and  $V_{RVE}^{magnetic}$  represent the volumes of the RVEs for a purely mechanical and purely magnetic phenomenon. It is also assumed for completeness that the “coupling phenomenon” itself results in a new different  $V_{RVE}^{coupling}$ .

For each aforementioned RVE, the minimum unit cell size showing converging response (within the given tolerance) will be determined as the lower bound of the corresponding RVE. Overall, four different RVE sizes for each phenomenon (elasticity, magnetism, elasto-magnetic coupling, magneto-elastic coupling) will be assessed and determined for an MRE in this study. Two different RVEs for coupling phenomenon were defined to assess the response of an MRE separately for external mechanical and magnetic effects. Thus, elasto-magnetic coupling refers to magnetic response due to external mechanical effects. For instance, magnetic induction developed in the unit cell of MRE due to applied mechanical

deformations will refer to elasto-magnetic coupling. Similarly, magneto-elastic coupling refers to mechanical response due to external magnetic effects. For instance, mechanical stresses developed in the unit cell because of an applied magnetic field.

The details of these RVEs' definitions and determination process will be explained in further sections. It must be also noted that RVE size can be understood as length (1D), area (2D) or volume (3D) according to considered application. In this study, 2D MRE samples under plane stress and static magnetic field conditions will be analysed. Therefore, RVE size should be understood as 2D area unless otherwise stated.

### 2.1.1 Microscopic characterisation of MRE

As discussed above, the MRE is modelled as a heterogeneous material on the micro-scale. The constitutive equations of the components (i.e. magnetostrictive particles and polymer matrix) can be written in the same form of Eq. (1.1) as follows:

$$\sigma_{ij}^m = C_{ijkl}^m \varepsilon_{kl} - q_{kij}^m H_k^m \quad (2.1a)$$

$$B_i^m = q_{ikl}^m \varepsilon_{kl} + \mu_{ik}^m H_k^m \quad (2.1b)$$

where superscript m denotes the micro-scale. Note that compared to Table 1.1 and Table 1.2, superscripts H and  $\varepsilon$  are omitted, in order to keep equations more readable.

**Note 1:** *As mentioned, the polymer material is not a magnetostrictive medium, but piezomagnetic constitutive equations (Eq. (2.1)) are also assumed for this material here. For the clarity, this point will be addressed and non-magnetisable polymer material will be explained in further sections.*

Kinematic relations, equilibrium equations and governing equations on the micro-scale can be derived as follow:

$$\varepsilon_{ij}^m = \frac{1}{2}(u_{i,j}^m + u_{j,i}^m) \quad (2.2a)$$

$$H_i^m = -\varphi_{,i}^m \quad (2.2b)$$

$$\sigma_{ij,j}^m = 0 \quad (2.3a)$$

$$B_{i,i}^m = 0 \quad (2.3b)$$

$$C_{ijkl}^m (u_{k,jl}^m) + q_{kij}^m (\varphi_{,jk}^m) = 0 \quad (2.4a)$$

$$q_{ikl}^m (u_{k,il}^m) - \mu_{ik}^m (\varphi_{,ik}^m) = 0 \quad (2.4b)$$

where  $u_i^m$  is the displacement, and  $\varphi^m$  is the scalar magnetic potential on the micro-level.

It is assumed that the unit cell is polarized along the  $z$ -direction, and all internal forces act on the  $xz$ -plane. It is believed that the reduction of the general constitutive equation (Eq. (1.2)) to the plane stress condition will be useful and leads a better understanding of the material matrices on the micro-level. Adopting a plane stress assumption as well as matrix-vector notation, the stiffness, piezomagnetic coupling and permeability matrices of the transversely isotropic material read

$$\mathbf{C}^m = \begin{bmatrix} C_{11} & C_{13} & 0 \\ C_{13} & C_{33} & 0 \\ 0 & 0 & C_{55} \end{bmatrix}, \quad \mathbf{q}^m = \begin{bmatrix} 0 & q_{31} \\ 0 & q_{33} \\ q_{15} & 0 \end{bmatrix}, \quad \boldsymbol{\mu}^m = \begin{bmatrix} \mu_{11} & 0 \\ 0 & \mu_{33} \end{bmatrix} \quad (2.5)$$

Thus, Eq. (2.6) with superscripts  $m$  can be written as the constitutive equations on the micro-scale.

$$\begin{Bmatrix} \sigma_1^m \\ \sigma_3^m \\ \sigma_5^m \end{Bmatrix} = \begin{bmatrix} C_{11} & C_{13} & 0 \\ C_{13} & C_{33} & 0 \\ 0 & 0 & C_{55} \end{bmatrix} \begin{Bmatrix} \varepsilon_1^m \\ \varepsilon_3^m \\ 2\varepsilon_5^m \end{Bmatrix} - \begin{bmatrix} 0 & q_{31} \\ 0 & q_{33} \\ q_{15} & 0 \end{bmatrix} \begin{Bmatrix} H_1^m \\ H_3^m \end{Bmatrix} \quad (2.6a)$$

$$\begin{Bmatrix} B_1^m \\ B_3^m \end{Bmatrix} = \begin{bmatrix} 0 & 0 & q_{15} \\ q_{31} & q_{33} & 0 \end{bmatrix} \begin{Bmatrix} \varepsilon_1^m \\ \varepsilon_3^m \\ 2\varepsilon_5^m \end{Bmatrix} + \begin{bmatrix} \mu_{11} & 0 \\ 0 & \mu_{33} \end{bmatrix} \begin{Bmatrix} H_1^m \\ H_3^m \end{Bmatrix} \quad (2.6b)$$

Here, material properties are taken for a polymer matrix and magnetic particles accordingly. The constitutive equations of micro stress and induction have the same form for both particles and polymer, but they will be calculated depending on their material properties. The properties have been adopted from [78, 113] and are given in Table 2.1. In contrast to magnetic particles, polymer materials cannot be magnetised and they do not exhibit magneto-elastic coupling as well. The assumed material properties for coupling coefficients and magnetic permeability of the polymer will lead to an ordinary non-magnetisable linearly isotropic polymer.

	$C_{11}$	$C_{13}$	$C_{33}$	$C_{55}$	$q_{31}$	$q_{33}$	$q_{15}$	$\mu_{11}$	$\mu_{33}$
<b>Terfenol-D [78]</b>	27	11.8	31.4	4.2	-15.2	217	68	9	1.86
<b>Polymer [113]</b>	7.8	4.7	7.8	1.6	0	0	0	$\mu_0$	$\mu_0$

$C_{ij}$  in GPa,  $q_{ij}$  in N/Am,  $\mu_{ij}$  in  $10^{-6}$ N/A<sup>2</sup>

**Table 2.1:** Material properties

Similarly, the kinematic relations, balance equations and governing equations can be written in matrix-vector notation as follow:

$$\boldsymbol{\varepsilon}^m = \mathbf{L}_u \mathbf{u}^m \quad (2.7a)$$

$$\mathbf{H}^m = -\mathbf{L}_\varphi \varphi^m \quad (2.7b)$$

$$\mathbf{L}_u^T \boldsymbol{\sigma}^m = \mathbf{0} \quad (2.8a)$$

$$\mathbf{L}_\varphi^T \mathbf{B}^m = \mathbf{0} \quad (2.8b)$$

$$\mathbf{L}_u^T \mathbf{C}^m \mathbf{L}_u \mathbf{u}^m + \mathbf{L}_u^T \mathbf{q}^m \mathbf{L}_\varphi \varphi^m = \mathbf{0} \quad (2.9a)$$

$$\mathbf{L}_\varphi^T \mathbf{q}^{mT} \mathbf{L}_u \mathbf{u}^m - \mathbf{L}_\varphi^T \boldsymbol{\mu}^m \mathbf{L}_\varphi \varphi^m = 0 \quad (2.9b)$$

where  $\mathbf{L}_\varphi = \nabla$  and  $\mathbf{L}_u$  is the usual strain-displacement derivative operator.

The boundary value problems for the 2D unit cell will be solved by using the finite element method.

### 2.1.2 Finite element equations

To obtain the finite element formulation, the weak form of governing equation [Eq. \(2.9\)](#) can be written for domain  $\Omega$  and boundary  $\Gamma$  after integration by parts<sup>2</sup> as follows:

$$\int_{\Omega} (\mathbf{L}_u \mathbf{w}_u)^T \mathbf{C}^m \mathbf{L}_u \mathbf{u}^m d\Omega + \int_{\Omega} (\mathbf{L}_u \mathbf{w}_u)^T \mathbf{q}^m \mathbf{L}_\varphi \varphi^m d\Omega = \int_{\Gamma} \mathbf{w}_u^T \mathbf{t} d\Gamma \quad (2.10a)$$

$$\int_{\Omega} (\mathbf{L}_\varphi \mathbf{w}_\varphi)^T \mathbf{q}^{mT} \mathbf{L}_u \mathbf{u}^m d\Omega - \int_{\Omega} (\mathbf{L}_\varphi \mathbf{w}_\varphi)^T \boldsymbol{\mu}^m \mathbf{L}_\varphi \varphi^m d\Omega = \int_{\Gamma} \mathbf{w}_\varphi^T \mathbf{B}_\perp d\Gamma \quad (2.10b)$$

where  $\mathbf{w}_u$  and  $w_\varphi$  are the test functions,  $\mathbf{t}$  are the boundary tractions, and  $\mathbf{B}_\perp$  is the magnetic traction on the boundary. By introducing the standard finite element shape functions  $\mathbf{N}_u$  and  $\mathbf{N}_\varphi$  for displacements and magnetic potential, i.e. 3 noded triangle element in 2D:

$$\mathbf{N}_u = \begin{bmatrix} N_1 & 0 & N_2 & 0 & N_3 & 0 \\ 0 & N_1 & 0 & N_2 & 0 & N_3 \end{bmatrix} \quad (2.11a)$$

$$\mathbf{N}_\varphi = \begin{bmatrix} N_1 & N_2 & N_3 \end{bmatrix} \quad (2.11b)$$

Thus, the following system of equations is obtained:

---

<sup>2</sup>The detailed formulation of the weak form has been given in [Appendix A](#)

$$\begin{bmatrix} \mathbf{K}_{uu} & \mathbf{K}_{u\varphi} \\ \mathbf{K}_{\varphi u} & -\mathbf{K}_{\varphi\varphi} \end{bmatrix} \begin{bmatrix} \mathbf{d}^m \\ \Psi^m \end{bmatrix} = \begin{bmatrix} \mathbf{F} \\ \Phi \end{bmatrix} \quad (2.12)$$

where  $\mathbf{d}^m$  and  $\Psi^m$  are micro-scale nodal displacement and nodal scalar magnetic potential vectors via  $\mathbf{u}^m = \mathbf{N}_u \mathbf{d}^m$  and  $\varphi^m = \mathbf{N}_\varphi \Psi^m$ . Moreover,  $\mathbf{F}$  and  $\Phi$  are nodal mechanical force and nodal magnetic flux vectors. Lastly, stiffness matrices are given by

$$\begin{aligned} \mathbf{K}_{uu} &= \int_{\Omega} \mathbf{B}_u^T \mathbf{C}^m \mathbf{B}_u d\Omega & \mathbf{K}_{u\varphi} &= \int_{\Omega} \mathbf{B}_u^T \mathbf{q}^m \mathbf{B}_\varphi d\Omega \\ \mathbf{K}_{\varphi u} &= \int_{\Omega} \mathbf{B}_\varphi^T \mathbf{q}^{mT} \mathbf{B}_u d\Omega & \mathbf{K}_{\varphi\varphi} &= \int_{\Omega} \mathbf{B}_\varphi^T \boldsymbol{\mu}^m \mathbf{B}_\varphi d\Omega \end{aligned} \quad (2.13)$$

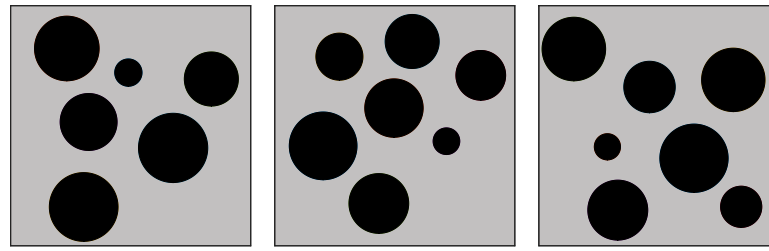
with  $\mathbf{B}_u = \mathbf{L}_u \mathbf{N}_u$ ,  $\mathbf{B}_\varphi = \mathbf{L}_\varphi \mathbf{N}_\varphi$ .

After obtaining the nodal degrees of freedom from boundary value problem on the unit cell, stresses and magnetic inductions in Eq. (2.6) can be calculated by following standard FE post-processing methods to be used for statistical analysis in the next section.

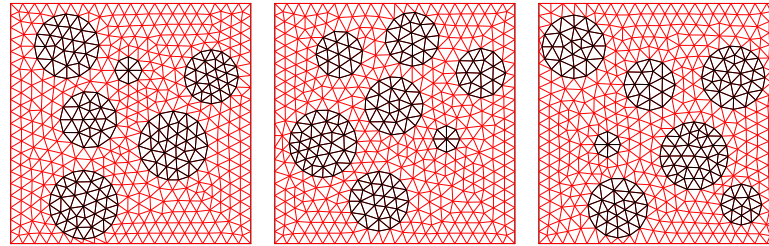
### 2.1.3 Definition and determination procedure of RVEs

As it has been argued earlier in Section 2.1, it is essential to determine the size of the RVE since it becomes a model parameter in the constitutive equations on the macro-scale which will be explored in Chapter 3. At this point, the behaviour of a unit cell can be investigated by using the FE equations derived in the previous section. Equations (2.1-2.13) will be used to solve the boundary value problem on a unit cell to obtain its response. Consequently, a systematic statistical method can be proposed to analyse unit cell sizes. The statistical procedure to determine a lower bound of the related RVE size is built on sets of numerical experiments performed for increasing unit cell sizes. The procedure can be summarised by the steps shown below.

1. Creation and meshing of different realisations for the tested unit cell size with fixed inclusion diameter (Uniform distribution of 100–300  $\mu\text{m}$  in diameter is assumed) and volume fraction ( $V_f = 30\%$ ) as seen in Figure 2.1. Different realisations have been considered, since an RVE must represent any part of the composite material as well as increasing the accuracy of statistical analysis. In each realisation, numbers and positions of the inclusions are randomly created for the given volume fraction and inclusion size. In this study, for an accurate statistical analysis, 200 realisations were created.



(a) Examples of different realisations of the unit cell



(b) FE mesh of different realisations of the unit cell

**Figure 2.1:** Different realisations of the unit cell and FE discretisation (size  $1 \times 1 \text{ mm}^2$  and  $V_f = 30\%$ )

2. Application of loading conditions such as a tension test and/or magnetic loading as shown in [Figure 2.2](#). The tension test is applied via prescribed nodal values of displacement  $U$  on the two corners on the left and right of the sample. Magnetic loading (static magnetic field in positive  $z$  direction in this study) was created via the magnetic potentials  $\varphi_l$  and  $\varphi_r$  on the left and right edges, respectively.

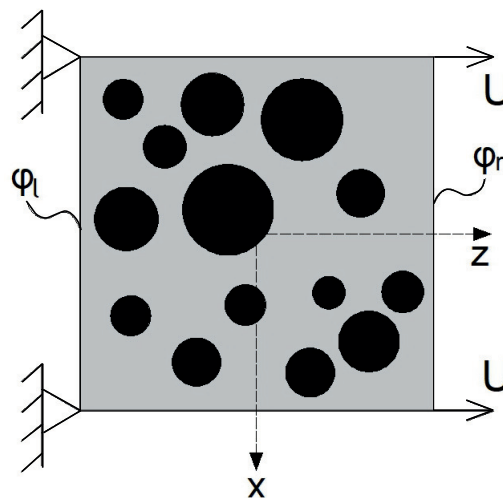


**Figure 2.2:** An RVE under external loadings

Furthermore, the periodicity in the deformation of an RVE might be a suitable kinematic condition, and it was shown that periodic boundary conditions can result in reasonable estimation of the effective properties for the unit cell [114, 115]. Here, the periodicity refers to construction of a particular FE mesh to ensure the continuity inside the material. As depicted in Figure 2.3, this specific mesh construction has been established via nodes on the corner of the unit cell identically having same position before and after the deformation. Additionally, each boundary pair (opposing edges) has equal deformation under tension and magnetic loading. This behaviour has been created by using tying constraints via penalty functions as given in [116]. These particular type of constraints relate two or more degrees of freedom to one another, and they are generally used to model periodicity. In a linear system of equation  $\mathbf{K}\mathbf{u} = \mathbf{f}$ , a tying is established between degrees of freedom  $n$  and  $m$  (positioned on opposite edges) via  $u_n - u_m = \bar{u}$  where  $\bar{u}$  is a prescribed number. With this relation, the energy potential leads to an extended  $\mathbf{K}$  and  $\mathbf{f}$  with a penalty function that accounts for tying  $\bar{u}$ . In the literature, the scalar  $\alpha$  is often known as the penalty parameter, and the linear system of equation becomes

$$[\mathbf{K} + \mathbf{K}^P]\mathbf{u} = \mathbf{f} + \mathbf{f}^P \quad (2.14)$$

where  $\mathbf{K}^P$  and  $\mathbf{f}^P$  are zero except for related  $m$  and  $n$  degrees of freedom,  $K_{mm}^P = K_{nn}^P = \alpha$ ,  $K_{mn}^P = K_{nm}^P = -\alpha$ ,  $f_m^P = -\alpha\bar{u}$  and  $f_n^P = \alpha\bar{u}$  (see [116] for more details).

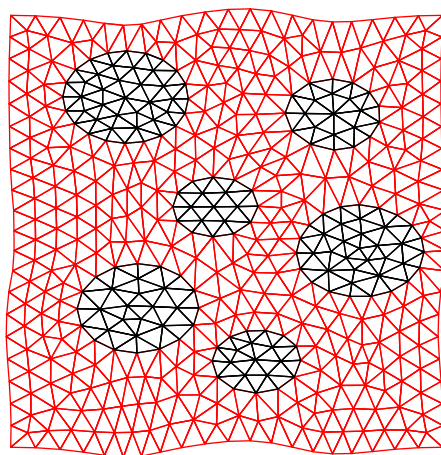


**Figure 2.3:** Periodic boundary conditions

3. Performing the FE analysis and obtaining the parameter of interest, that is the averaged stress or the averaged magnetic induction along the  $z$  direction over the

unit cell. At this point, the  $z$  components of averaged stress and magnetic induction are evaluated since the maximum magnetostriction response is expected in this direction. Here, the different unit cell sizes namely  $L_1, L_2, L_3$  and  $L_4$  are assessed separately as discussed previously in [Section 2.1](#). In particular,  $L_1$ , which is the unit cell size for purely mechanical response, is determined by applying the tension test and calculating the averaged stress in  $z$  direction due to this loading. Similarly, the unit cell size for a purely magnetic response,  $L_4$ , is assessed by calculating the averaged magnetic induction in  $z$  direction due to only the external magnetic loading. Lastly, the unit cell sizes for coupling response  $L_2$  and  $L_3$  are evaluated by obtaining the averaged stress results from external magnetic loading, and obtaining the averaged magnetic induction results from tension test, respectively. Note, that these two conceptually different effects lead to two different "coupling" RVEs as discussed earlier in [Section 2.1](#).

4. After calculating the parameter of interest for each realisation of a unit cell size, statistical analysis can be conducted on these data. Various statistical approaches can be used. In this study, the coefficient of variation value for the FE results will be used. This coefficient presents the deviation of a single unit cell from the mean of all realisations of the same unit cell size, and it is calculated as the ratio of standard deviation to the mean of investigated parameter.

$$CV = \frac{\sqrt{\frac{\sum_{i=1}^n (x_i - \langle x_i \rangle)^2}{n}}}{\langle x_i \rangle} \quad (2.15)$$

where  $n$  is the number of realisations (200) and  $x_i$  is either averaged  $\sigma_z$  or  $B_z$ .

5. Comparison of statistical analysis accuracy with the desired accuracy (which was taken 97% here).
6. Defining the tested size of the unit cell as the RVE size, if the desired accuracy is achieved. In this case, it must be remembered that unit cell sizes  $L_1$  and  $L_4$  become the corresponding RVEs sizes of  $V_{RVE}^{elastic}$  and  $V_{RVE}^{magnetic}$ . Similarly, unit cell sizes  $L_2$  and  $L_3$  are considered as two different RVE sizes for coupling effects. If the accuracy is not achieved, increasing the unit cell size (see [Figure 2.4](#)) and repeating the process from step 1.

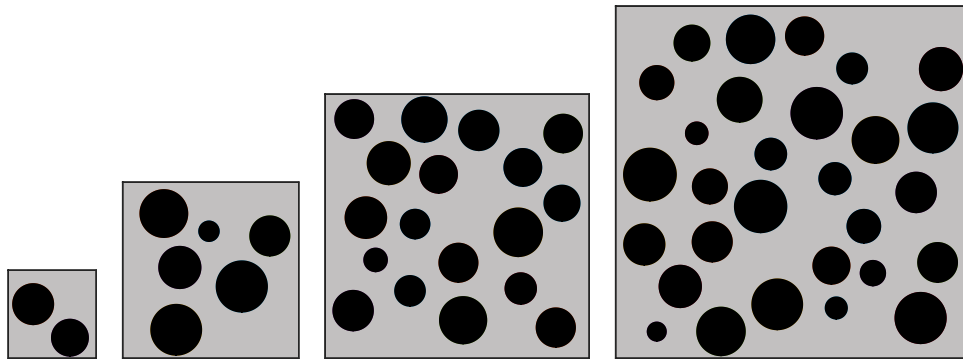


**Figure 2.4:** Different sizes of unit cells (from left to right:  $0.5 \times 0.5 \text{ mm}^2$ ,  $1 \times 1 \text{ mm}^2$ ,  $1.5 \times 1.5 \text{ mm}^2$ ,  $2 \times 2 \text{ mm}^2$  and  $V_f = 30\%$ )

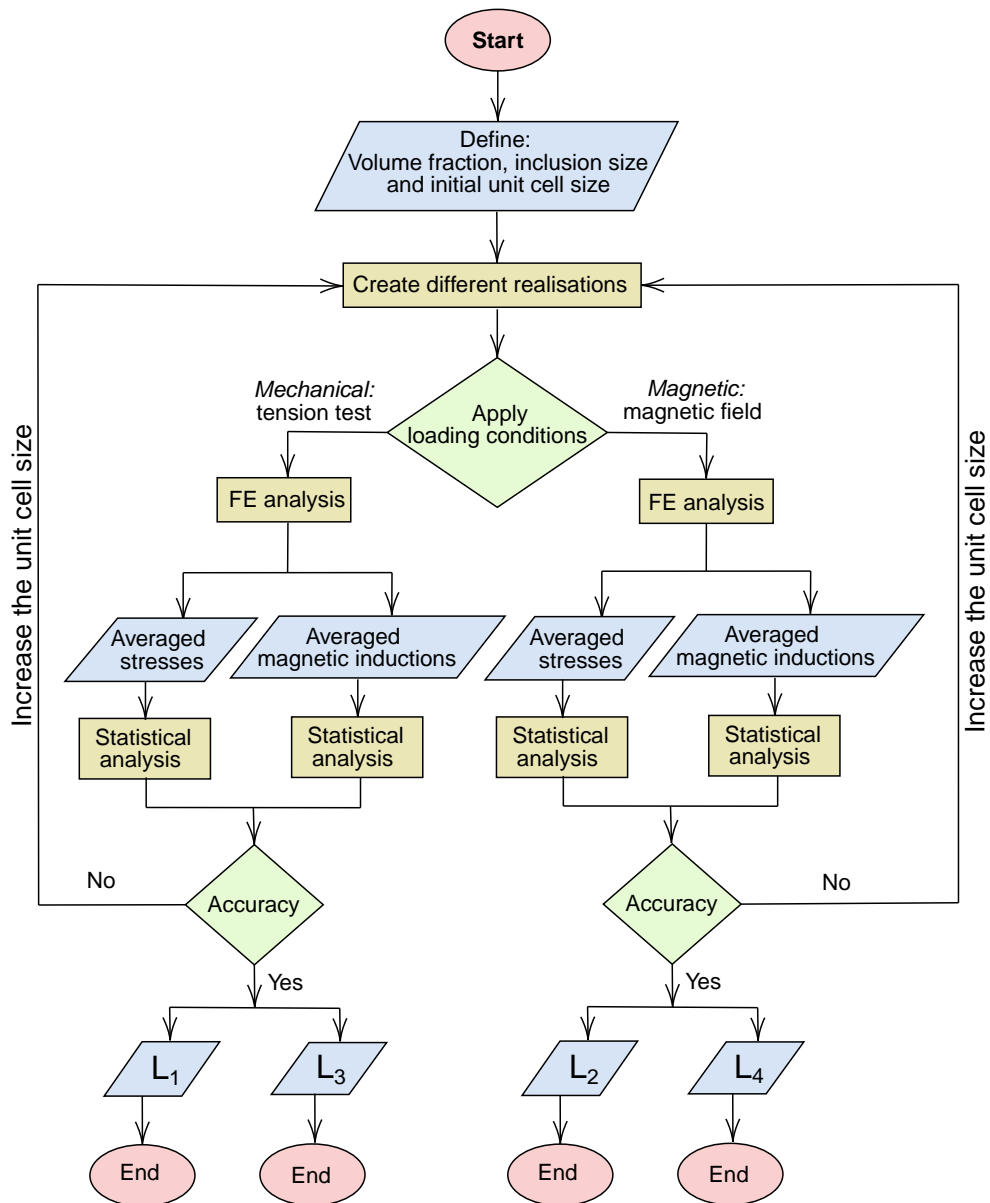


**Figure 2.5:** Procedure of RVEs sizes determination

**Note 2:** *These RVE sizes will be employed as model parameters in the governing equations of the macroscopic magneto-elastic continua in the next chapter (see Eq. (3.15) for purely mechanical, magnetic and coupling terms.)*

## 2.2 Numerical results and influence of material properties on RVEs

The numerical experiments were conducted with a MATLAB code developed in-house. For the magnetic particles, Terfenol-D material was chosen due to some of its advantages discussed in the first chapter. In the calculation of the material constants for the magnetic particles, the relationships given in Table 1.1 was followed. As mentioned, the matrix (polymer) was assumed as a non-magnetisable material. Because of this assumption, piezomagnetic constants were taken as zero to represent this behaviour. Also, the magnetic permeability of the matrix has been assumed to equal the magnetic permeability of the free space ( $\mu_0 = 4\pi 10^{-6} \text{N/A}^2$ ) due to the same assumption.

Two hundred different realisations of each unit cell size (ranging from 0.5 to 2.5 mm) have been considered. The size of Terfenol-D particles have been chosen to be uniformly distributed between of 100–300  $\mu\text{m}$  in diameter. The responses of the unit cells have been obtained via finite element analysis by using three-node triangular elements. Following numerical analysis of all realisations, coefficients of variation have been calculated for each sample size to investigate the convergence of the results. It is expected that a lower value of coefficient of variation and a convergent trend should be observed for increasing unit cell size since the unit cells larger than the lower bound of the RVE will present a similar response. Coefficient of variation is a statistical measure of relative variability, and it is a useful statistic for comparing the degree of variation between data series. A lower value of the coefficient of variation means a more precise estimation. It is calculated as the ratio of the standard deviation of the investigated parameter ( $\sigma_{zz}$  or  $B_z$ ) to the mean (see Eq. (2.15)). By comparing the coefficients of variation of computed parameters with the desired value, i.e. it is 0.03 for 97% accuracy, a lower bound of the RVE can be defined as seen in Figure 2.6. As shown in the figure, once the desired accuracy and the results from the numerical tests have been plotted on the same graph, the intersection of the obtained values and chosen allowed variability can be evaluated to define the related representative sizes.

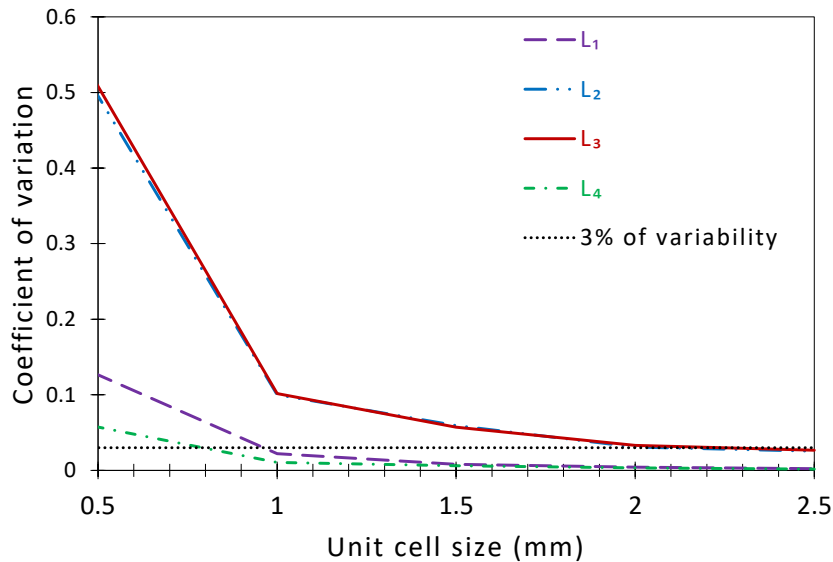


**Figure 2.6:** Convergence of the results

Realisations of each cell size (Figure 2.2) were subjected to mechanical ( $U = 0.1$  mm) loading. Scalar magnetic potentials  $\varphi_l$  and  $\varphi_r$  have been assigned on the left and right edges to create the magnetic field ( $H_z = 20$  kA/m) that corresponds to a small variation around bias field used in the measurement of material properties of Terfenol-D [78]. The steps given in Subsection 2.1.3 were followed. Figure 2.6 shows converging trends around different unit cell size values for  $L_1$ ,  $L_2$ ,  $L_3$  and  $L_4$ . It can be seen that the lower bound of the RVE can be considered as 1 mm for  $L_1$ , 0.9 mm for  $L_4$ , and 2.3 mm for  $L_2$  and  $L_3$ . Furthermore, it is remarkable how small the difference between  $L_2$  and  $L_3$  is. This confirms the thermodynamic consistency requirements discussed later in the next chapter. As shown above, it is now possible to determine the lower bound of the RVE sizes for an MRE material. In the coupling framework, four different RVE sizes have been defined and determined to represent different phenomena rather than only one RVE size as given for purely elastic framework.

It has already been shown for purely elastic material that the lower bound of the RVE size is affected by the stiffness ratio of the constituents [41]. Notably, changing the stiffness ratio, which also means increased heterogeneity, causes an increase in the lower bound of RVE size in purely elastic case. For this reason, it is worthwhile to conduct a parametric study to investigate the effect of material parameters on the different RVE sizes such as contrast in stiffness, coupling and permeability properties of the constituents. Hence, a formalistic approach was established, and theoretical test specimens were created to study the aforementioned contrasts.

### 2.2.1 Contrast in elastic properties

Contrast in elastic properties was the first parameter to investigate the increased heterogeneity in elastic properties of the constituents. The stiffness ratio  $\beta_c$  was defined as a ratio between inclusions and matrix stiffnesses, see Eq. (2.16). The ratio  $\beta_c$  was achieved by decreasing the stiffness constants of matrix physically representing relatively softer polymers.  $\beta_c$  ranges (5, 25, 100) introduce the change in heterogeneity. This setup ensures that there will be factors of 5, 25 and 100 between the components' stiffness properties. Piezomagnetic coupling and magnetic permeability of the constituents were considered as given in Table 2.1 to investigate influence of the stiffness contrast only.

$$\beta_c = \frac{C_{\text{inclusion}}}{C_{\text{matrix}}} \quad (2.16)$$

Numerical experiments and statistical analysis were performed for all stiffness contrast ratios. Figure 2.7 demonstrates the effect of the elastic stiffness ratios on the RVE sizes. It can be seen that there is a positive correlation between the contrast and the lower bound of the RVE size up to a certain value of  $L_1$  that represents the purely mechanical RVE size. When the contrast ratio is increased from 5 to 25, the lower bound of RVE size has values of around 1 and 1.3 mm, respectively (Figure 2.7a). However, increasing the stiffness contrast to more than 25 does not lead a notable further change. Furthermore, it was found that different contrast values in stiffness result in near identical RVE sizes for the coupling and purely magnetic RVE sizes  $L_2$ ,  $L_3$  and  $L_4$  (Figure 2.7(b-d)), which means that the stiffness contrast does not affect those RVE sizes.

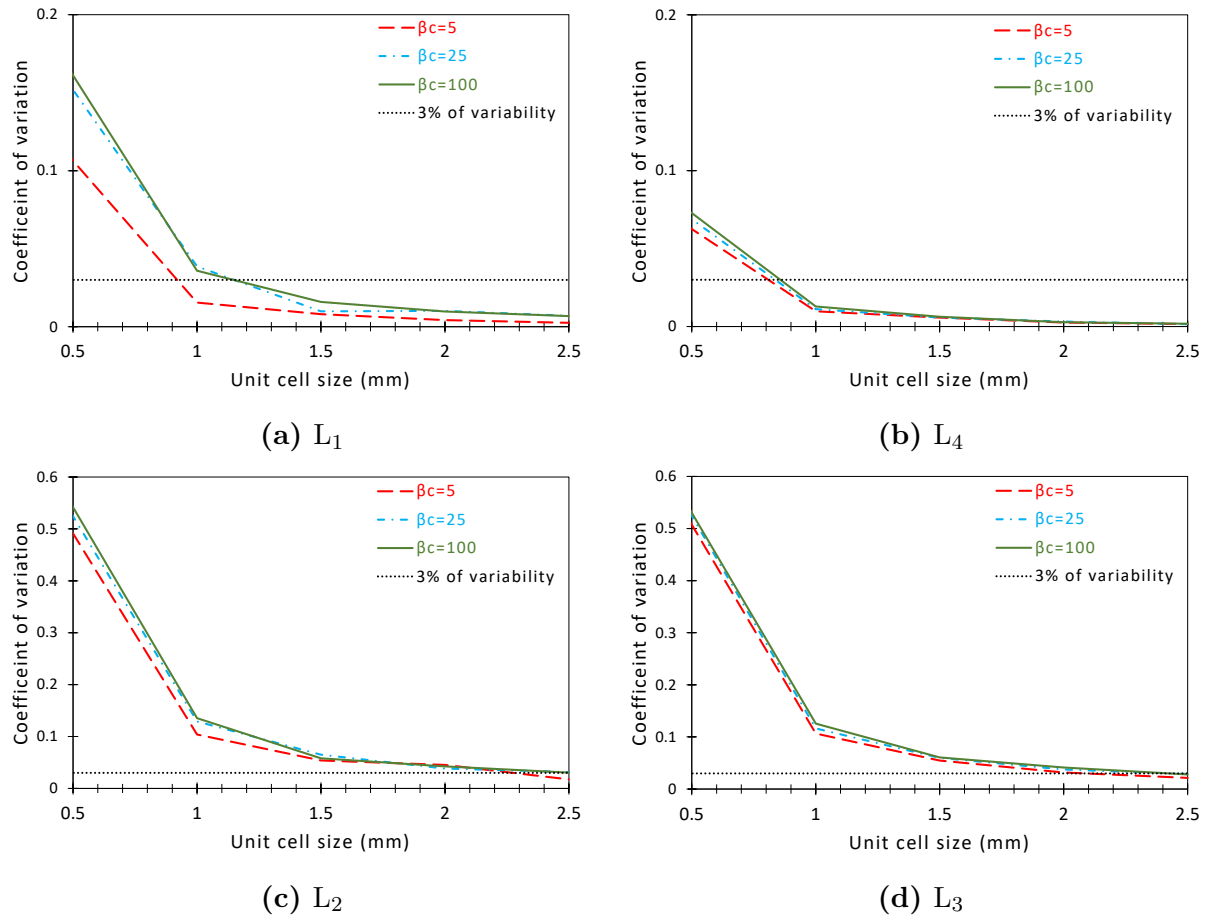


**Figure 2.7:** RVE sizes for different stiffness contrast values.  $L_1$  (a),  $L_4$  (b),  $L_2$  (c), and  $L_3$  (d).

### 2.2.2 Contrast in piezomagnetic coupling properties

Similarly, the influence of the contrast in piezomagnetic coupling has been analysed via the ratio  $\beta_q$  as given in see Eq. (2.17). The ratio  $\beta_q$  was obtained by changing the piezomagnetic coupling constants of matrix, and factors of 5, 25 and 100 between the components' piezomagnetic coupling properties have been tested. Here, the stiffness and the magnetic permeability properties were kept constant and as given Table 2.1 to study only piezomagnetic coupling effects.

$$\beta_q = \frac{q_{\text{inclusion}}}{q_{\text{matrix}}} \quad (2.17)$$

Numerical analysis were conducted in the same way, and Figure 2.8 depicts the influence of the piezomagnetic coupling contrast on the RVE sizes. It has been observed that more contrast in coupling properties of the constituents leads to larger coupling RVE sizes

$L_2$  and  $L_3$  only (Figure 2.8(c,d)), with minimal effects on  $L_1$  and  $L_4$  (Figure 2.8(a,b)). By increasing the coupling contrast ratio from 5 to 100, the lower bounds of those coupling RVE sizes  $L_2$  and  $L_3$  continuously increase, and have values around 1, 1.5 and 2.1 mm respectively (Figure 2.8(c,d)). A distinct difference between the coupling and elastic contrast results was observed here. In the previous case, the elastic contrast values 25 and 100 resulted in same RVE sizes for affected  $L_1$  (Figure 2.7a). However, same values of coupling contrast (25 and 100) led to notably different RVE sizes for affected  $L_2$  and  $L_3$  (Figure 2.8(c,d)). It was also observed that different contrast values in piezomagnetic coupling presented identical RVE sizes for the purely elastic and purely magnetic RVE sizes  $L_1$  and  $L_4$  (Figure 2.8(a,b)) which means that the coupling contrast does not affect those RVE sizes. This result is similar to the elastic contrast results that have an influence only on the the purely elastic RVE size.

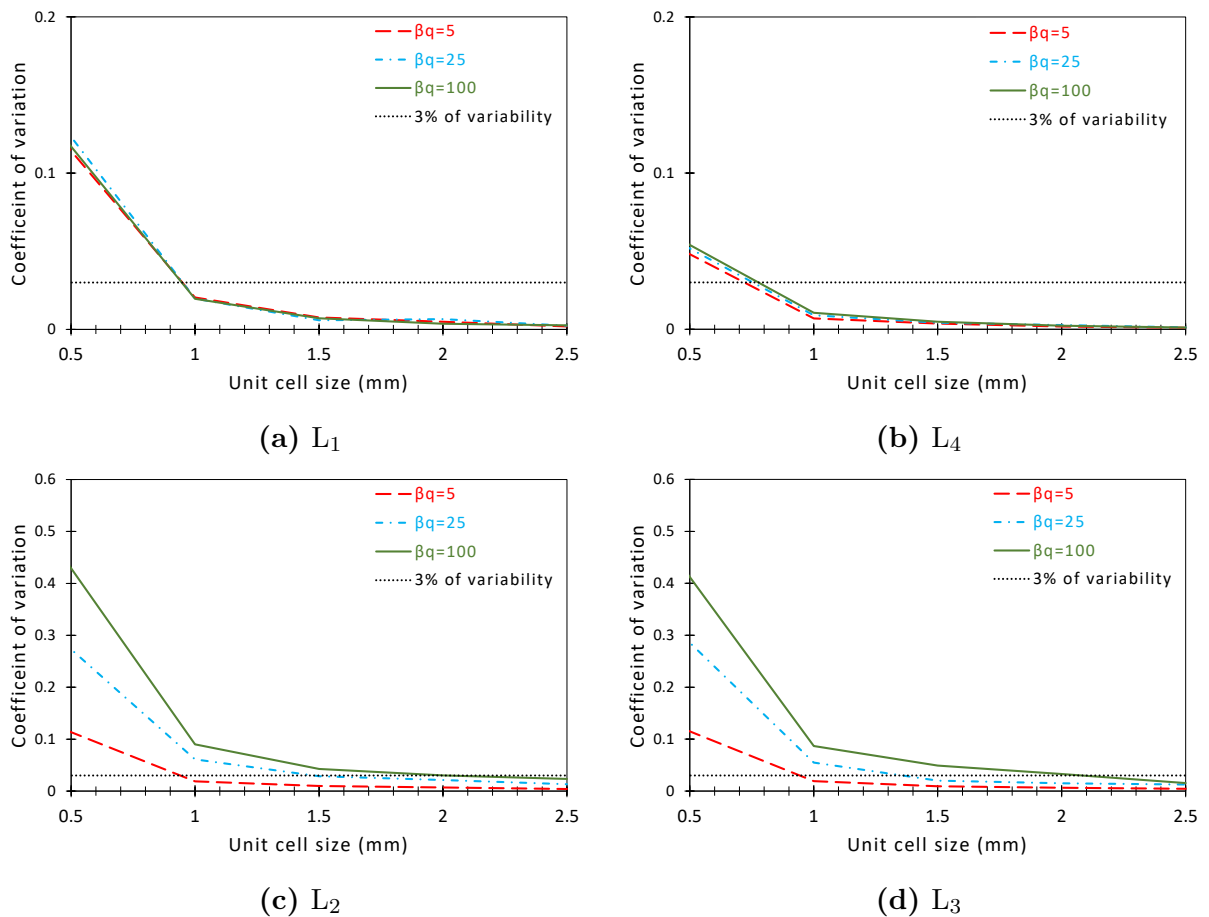


**Figure 2.8:** RVE sizes for different piezomagnetic contrast values.  $L_1$  (a),  $L_4$  (b),  $L_2$  (c), and  $L_3$  (d).

### 2.2.3 Contrast in magnetic permeability properties

The contrast in magnetic permeability is the basis of the next test setup. This contrast has been introduced via the ratio  $\beta_\mu$ . This ratio has been established by changing the magnetic permeability constants of particles, since the matrix has the magnetic permeability of the free space as discussed in beginning of [Section 2.2](#). The same factors (5, 25 and 100) between the constituents' magnetic permeability properties have been achieved. Analogous to the previous cases, piezomagnetic coupling and the stiffness constants at the values given in [Table 2.1](#) were chosen to study only the effect of the permeability.

$$\beta_\mu = \frac{\mu_{\text{inclusion}}}{\mu_{\text{matrix}}} \quad (2.18)$$

[Figure 2.9](#) presents the result of these configurations. The results show that contrast in magnetic permeability has an effect on the RVE size  $L_4$ , and this trend is similar to stiffness contrast for  $L_1$  ([section 2.2.1](#)). The lower bound of RVE size has values of around 1 and 1.3 mm for the contrast ratio increased from 5 to 25, respectively ([Figure 2.9b](#)). Also, magnetic permeability contrast more than 25 does not lead a significant further change for  $L_4$  as seen in the elastic contrast case for  $L_1$  ([Figure 2.9a](#)). In addition, identical RVE sizes for the coupling and purely elastic RVE sizes  $L_1$ ,  $L_2$  and  $L_3$  have been observed again ([Figure 2.9\(a,c,d\)](#)), which shows that the magnetic permeability contrast does not have an influence on those RVE sizes.

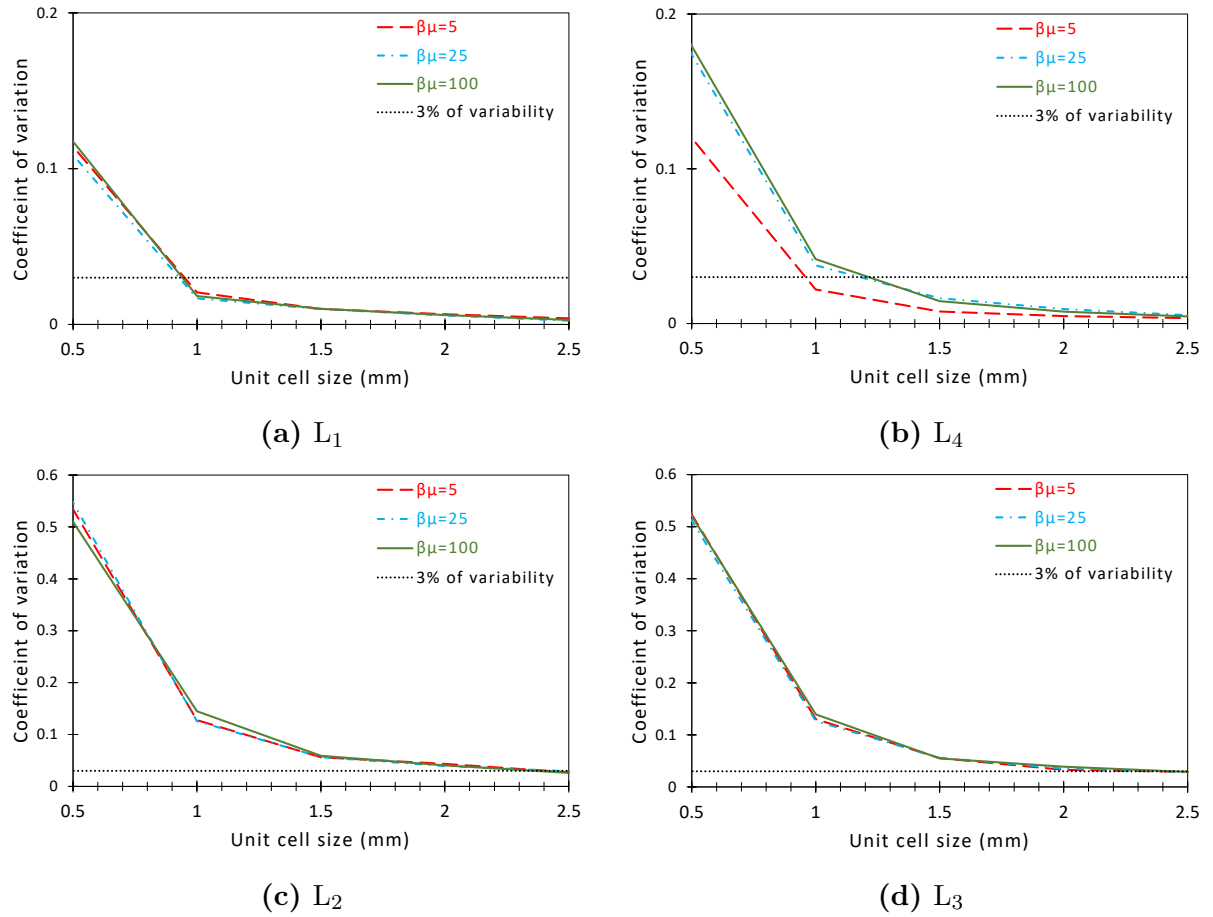


**Figure 2.9:** RVE sizes for different permeability contrast values.  $L_1$  (a),  $L_4$  (b),  $L_2$  (c), and  $L_3$  (d).

## 2.2.4 Larger contrast in elastic and magnetic properties

In addition to contrasts of 5, 25 and 100, it is relevant to investigate larger contrast values to understand the influence better since there is almost no difference between 25 and 100 values for  $L_1$  and  $L_4$  in case of stiffness and permeability contrasts, respectively. To study this point in more details, additional contrast values were created in the same ways (for  $\beta_c$ ,  $\beta_q$  and  $\beta_\mu$ ), and influence of each contrast configuration analysed for the related RVE size.

As seen in [Figure 2.10](#), the results for more contrast values 10, 100, 1000, 10000 and 100000 have been plotted on the same graph for each RVE size. The pattern in the coupling contrast increase for  $L_2$  and  $L_3$  is different and it shows a continuously increasing RVE sizes. However, the difference between the RVE sizes for larger permeability and stiffness contrasts for  $L_4$  and  $L_1$  is relatively insignificant compared to other cases beyond a value of 100. For the higher values, the purely mechanical and magnetic RVE sizes have

been determined to be around 1 and 1.1 mm, respectively. Here, it can be concluded that RVE sizes are dependent on the stiffness, coupling and permeability contrast of the constituents which means heterogeneity in these properties is an effective parameter for the related RVE size. The case of a large contrast in coupling could represent a material with (a) component with pronounce magnetostrictive behaviour and (b) component with almost negligible magnetostrictive response. In this case, representative volume elements related to coupling indeed will be larger (but still will exist and be measurable).

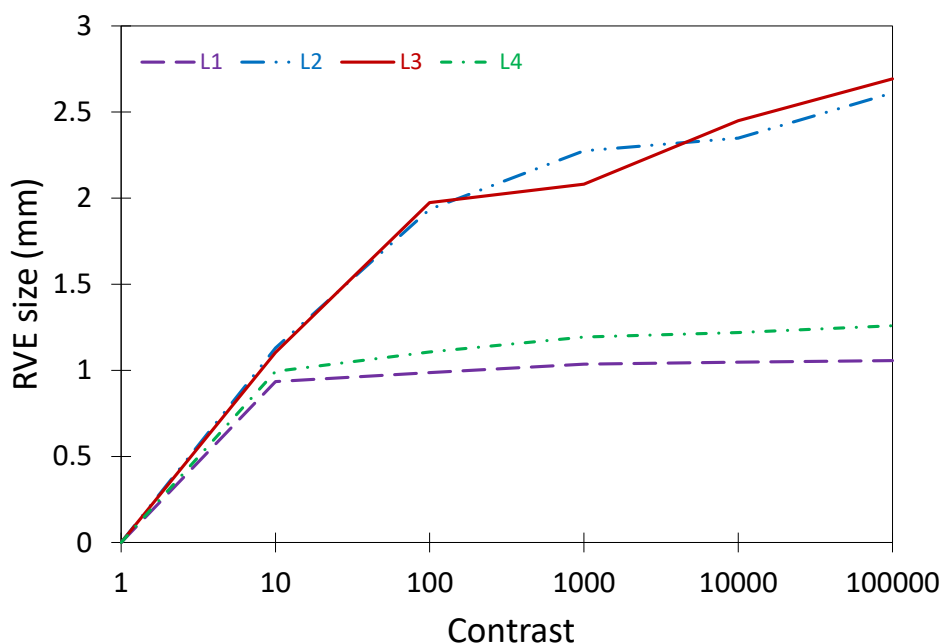


**Figure 2.10:** RVE sizes for larger contrast values

## 2.3 Discussion

In this chapter, the significance of the representative volume element (RVE) size as a model parameter, and motivations for determination of this size have been discussed. Next, definition and determination process of the RVE size for a magnetorheological material have been established. A systematic statistical method has been proposed for an MRE material on the micro-level to determine the defined RVE sizes depending on different phenomena in magneto-elastic framework. Finite element method has been used to solve the microscopic boundary value problems to conduct a statistical analysis on the response of the unit cells. After establishing the procedure and determining the RVE sizes for a Terfenol-D/Polymer sample, the influence of some parameters such as contrasts in stiffness, coupling and permeability properties of the constituents have also been studied.

The proposed statistical analysis can be used to determine lower bounds of the RVE sizes for an MRE material. Here, four different RVE sizes were postulated for different phenomena namely  $L_1$  for purely elastic,  $L_4$  for purely magnetic, and  $L_2$  and  $L_3$  for coupling behaviour in the material. In line with thermodynamic consistency, the difference between the lower bound of  $L_2$  and  $L_3$  was found to be negligible, however the determined RVE sizes for  $L_1$  and  $L_4$  are clearly smaller and different. As a practical conclusion, it may be suggested that using the largest determined RVE sizes for  $L_2$  or  $L_3$  also covers the lower bound condition of the other RVE sizes and only this size can be used. It is specifically relevant in gradient enriched governing equations discussed in the next chapter.

Moreover, the formalistic approach also showed that the contrast in material properties of the constituents can affect the minimum RVE sizes. It was found that the increase in stiffness contrast leads to larger values of  $L_1$ , whereas there is no influence on the other RVE sizes. Similarly, the same trend was observed for an increase in coupling and permeability contrasts for the RVE sizes  $L_2$  or  $L_3$ , and  $L_4$ , respectively. It can be concluded that for more heterogeneity in these material properties, larger sizes of the associated RVE are obtained. It was also previously shown that an increased stiffness contrast can lead larger RVE sizes for a purely elastic model [41], and the results in this chapter also confirms this conclusion for not only purely elastic, but also for a coupling model. Finally, a converging trend was observed for  $L_1$  and  $L_4$ , but  $L_2$  and  $L_3$  show a non-convergent trend in the range of assumed larger contrast values. Given that the difference between convergent  $L_1$  and  $L_4$  and non-convergent  $L_2$  and  $L_3$  occurs for extremely large contrast, for practical purposes one may assume  $L_1 = L_2 = L_3 = L_4 = \max(L_i) \equiv L$ . This conclusion remark will also be used in the next chapter.

Overall, separately considered RVE sizes for an MRE material can be determined by following the statistical analysis as given in this chapter. Moreover, it has been shown that the contrast between the elastic and magnetic properties of the constituents is an effective parameter for the related RVE sizes. However, the pattern of this effectiveness is different for coupling and purely elastic/magnetic RVEs. With these elaborations, the first step of introducing the microstructural information to the macroscopic behaviour of a magneto-elastic model is completed. As the next step, the constitutive and governing equations of the macroscopic continua will be derived with the model parameters RVE sizes. Thus, the conclusions and determined RVE sizes can be used in this macro-level model to present the efficiency of the gradient formulation enriched with the RVE sizes.

# Chapter 3

## RVE Sizes and Length-Scale Identification in Generalised Magneto-Elasticity

In this chapter <sup>1</sup>, the link between model parameter RVE size and material parameter length-scale in magneto-elastic coupling framework will be derived by using an analytical homogenisation scheme. In particular, the second-order homogenisation technique will be used. Kouznetsova et al. presented this terminology in a numerical homogenisation scheme [110, 118]. Later, Gitman et al. established the link between those parameters in decoupled elasticity framework [41, 44]. In this chapter, a generalised magneto-elastic continuum model with gradients of strain, magnetic field, and piezomagnetic coupling terms will be presented. Characteristic length-scale parameters, accompanying the higher order components in the model, will be identified in terms of representative volume element (RVE) sizes discussed in [Chapter 2](#) in order to introduce the microstructural information to material properties on the macro-level.

Another aim of this chapter is to present the influence of identified length-scale parameters in removing mechanics and magnetic singularities by using determined RVE sizes ([Chapter 2](#)) as a model parameter in the generalised magneto-elasticity, thereby bridging the gap between RVE-based approaches and generalised/non-local continuum approaches

---

<sup>1</sup>This chapter is partly adopted from:

Eraslan, S., Gitman, I.M., Xu, M., Askes, H., de Borst, R. (2023). Representative Volume Element Size and Length Scale Identification in Generalised Magneto-Elasticity. In: Altenbach, H., Berezovski, A., dell'Isola, F., Porubov, A. (eds) *Sixty Shades of Generalized Continua*. Advanced Structured Materials, vol 170. Springer, Cham. [117]

on the macro-level. For this, the macro-level magneto-elastic constitutive formulation with identified length-scale parameters and determined RVE sizes will be implemented. Further, numerical results will be presented for a two-dimensional in-plane problem to remove singularities in mechanics and magnetic fields.

### 3.1 Non-local homogenisation

As has been stated in Introduction, various approaches can be followed to model and analyse the behaviour of heterogeneous materials. In particular, a phenomenological multi-scale approach can be used. In this approach, microstructural material information is introduced via phenomenological (but related to material) parameters: length- and/or time-scale in non-local continuum theories, contrary to classical (local) continuum theories that do not take microstructure into account [84,106,107,119–122]. On the other hand, another approach: homogenisation-based multi-scale frameworks that considers the interaction of different scales explicitly can be used. In this approach, the unit cell representing micro-level is denoted as RVE and its size becomes model parameter. The aforementioned links between the parameters of different approaches have been presented for materials with periodic and random microstructures [42–44, 108, 109]

Gitman et al. [42–44], and Kouznetsova et al. [110]. have introduced a non-local homogenisation technique in purely elastic context to establish this link. Homogenisation describes the relation between the quantities on micro- and macro-scale, and the proposed non-local homogenisation scheme was built on averaging the stresses in the RVE. The macroscopic stresses (superscript M) were defined as the volume average of microscopic counterparts (superscript m) that leads

$$\sigma_{ij}^M = \langle \sigma_{ij}^m \rangle = \frac{1}{V_{RVE}} \int_{V_{RVE}} \sigma_{ij}^m dV \quad (3.1)$$

Thus, by also considering the microscopic constitutive equations, macroscopic stresses can be written as

$$\sigma_{ij}^M = \frac{1}{V_{RVE}} \int_{V_{RVE}} C_{ijkl}^m \epsilon_{kl}^m dV \quad (3.2)$$

As the next step, linearisation of microscopic stiffness and strains were expressed around the values at the centre of the RVE by assuming small perturbations compared to the average values.

$$C_{ijkl}^m = C_{ijkl}^M + C_{ijkl,o}^M \delta x_o \quad (3.3a)$$

$$\varepsilon_{kl}^m = \varepsilon_{kl}^M + \varepsilon_{kl,p}^M \delta x_p \quad (3.3b)$$

Combining Eq. (3.2) and Eq. (3.3) yields

$$\begin{aligned} \sigma_{ij}^M = \frac{1}{V_{RVE}} \int_{V_{RVE}} & (C_{ijkl}^M \varepsilon_{kl}^M + C_{ijkl}^M \varepsilon_{kl,p}^M \delta x_p + C_{ijkl,o}^M \varepsilon_{kl}^M \delta x_o \\ & + C_{ijkl,o}^M \varepsilon_{kl,p}^M \delta x_o \delta x_p) dV \end{aligned} \quad (3.4)$$

Finally, non-local homogenisation can be performed via integration of Eq. (3.4) with the assumptions of periodic boundary conditions, symmetric domain and 2D context. As seen in Eq. (3.3), the quantities  $C_{ijkl}^M$ , and  $\varepsilon_{kl}^M$  are equal to their microscopic counterparts  $C_{ijkl}^m$ , and  $\varepsilon_{kl}^m$  calculated at the centre of the RVE. Therefore, these quantities can be taken out of the integral in Eq. (3.4) since they become constant with the values at the centre of the RVEs. Assuming a square RVE with its centre acting as origin of a Cartesian coordinate system, the linear terms of  $\delta x$  are cancelled as they consist of odd functions integrated over a symmetric domain. The only quadratic term are integrated by parts as follows

$$\begin{aligned} \int_{V_{RVE}} C_{ijkl,o}^M \varepsilon_{kl,p}^M \delta x_o \delta x_p dV = \int_S C_{ijkl}^M \varepsilon_{kl,p}^M n_o \delta x_o \delta x_p dS - \int_{V_{RVE}} & (C_{ijkl}^M \varepsilon_{kl,op}^M \delta x_o \delta x_p \\ & + C_{ijkl}^M \varepsilon_{kl,p}^M \delta x_{o,o} \delta x_p + C_{ijkl}^M \varepsilon_{kl,p}^M \delta x_o \delta x_{p,o}) dV \end{aligned} \quad (3.5)$$

where  $n_o$  is a normal vector to surface of domain  $S$ .

Next, the boundary integral vanish due to assumption of periodic boundary conditions, and the last two terms in Eq. (3.5) are also cancelled since they consist of odd functions again. The integral of the quadratic term can be evaluated for two-dimensional context as follow

$$\int_{V_{RVE}} \delta x_o \delta x_p dV = \int_{-\frac{L}{2}}^{\frac{L}{2}} \int_{-\frac{L}{2}}^{\frac{L}{2}} \delta x_o \delta x_p dx_1 dx_3 \quad (3.6a)$$

$$= \frac{1}{12} L^4 \delta_{op} \quad (3.6b)$$

where  $\delta_{op}$  is the Kronecker delta,  $V_{RVE} = L^2$  and  $L$  is the size of the RVE.

After this integration, macroscopic constitutive equation Eq. (3.4) can be obtained as

$$\sigma_{ij}^M = C_{ijkl}^M \left( \varepsilon_{kl}^M - \frac{L^2}{12} \varepsilon_{kl,pp}^M \right) \quad (3.7)$$

As seen, Eq. (3.7) includes a coefficient in terms of RVE size  $L$  with gradients of macroscopic strains in addition to usual macroscopic parameters. As a result, an analogy was observed between Eq. (3.7) provided by Gitman et al. [42–44] from non-local homogenisation and the constitutive equation for the gradient elasticity model presented by Aifantis and co-workers. [123, 124].

$$\sigma_{ij} = C_{ijkl} \left( \varepsilon_{kl} - \ell^2 \varepsilon_{kl,mm} \right) \quad (3.8)$$

where  $\ell$  is the length-scale parameter. Thus, the link between the phenomenological parameter length-scale and RVE size was established as

$$\ell^2 = \frac{L^2}{12} \quad (3.9)$$

As discussed above, this relationship between the length-scale and the RVE size was obtained and analysed for purely elastic context. Here, the non-local homogenisation scheme will be extended to a coupled framework, particularly for a generalised magneto-elastic continua. Macroscopic constitutive and governing equations for a piezomagnetic model will be derived by including length-scale parameters expressed in terms of the related RVE sizes following the discussion in Chapter 2. With these elaborations, microstructural information obtained in previous chapter will be taken into account in a 2D magneto-elastic system.

## 3.2 Homogenisation and macroscopic length-scale parameter in MREs

In contrast to heterogeneous micro-level, MRE is modelled as a piezomagnetic material with homogeneous effective material properties and model parameters on the macro-level. This approach brings the advantage of computational efficiency with an accurate description of the material behaviour on the macro-level. In the multi-scale analysis of an MRE, the macroscopic stress and induction on the integration point can be defined as the volume average of the microscopic counterparts in the RVE:

$$\sigma_{ij}^M = \frac{1}{V_{RVE}} \int_{V_{RVE}} \sigma_{ij}^m dV = \frac{1}{V_{RVE_1}} \int_{V_{RVE_1}} C_{ijkl}^m \epsilon_{kl}^m dV - \frac{1}{V_{RVE_2}} \int_{V_{RVE_2}} q_{kij}^m H_k^m dV \quad (3.10a)$$

$$B_i^M = \frac{1}{V_{RVE}} \int_{V_{RVE}} B_i^m dV = \frac{1}{V_{RVE_3}} \int_{V_{RVE_3}} q_{ikl}^m \epsilon_{kl}^m dV + \frac{1}{V_{RVE_4}} \int_{V_{RVE_4}} \mu_{ik}^m H_k^m dV \quad (3.10b)$$

where the superscripts m and M denote the micro and macro-level, respectively. After determining and analysing the properties of the RVE sizes as presented in previous chapter, it is now possible to derive the macroscopic constitutive and governing equations by using Eq. (3.10) and the second-order (non-local) homogenisation scheme. Consequently, the formulation of a fully coupled magneto-mechanical model with gradients in terms of RVE sizes can be obtained to introduce the microstructural information to the macro-scale model. Before applying non-local homogenisation, linearisation of spatially dependent stiffness, strain, coupling, permeability and magnetic field can be expressed around the values at the centre of the RVEs as follow

$$C_{ijkl}^m = C_{ijkl}^M + C_{ijkl,o}^M \delta x_o \quad (3.11a)$$

$$\epsilon_{kl}^m = \epsilon_{kl}^M + \epsilon_{kl,p}^M \delta x_p \quad (3.11b)$$

$$q_{kij}^m = q_{kij}^M + q_{kij,o}^M \delta x_o \quad (3.11c)$$

$$H_k^m = H_k^M + H_{k,p}^M \delta x_p \quad (3.11d)$$

$$\mu_{ik}^m = \mu_{ik}^M + \mu_{ik,o}^M \delta x_o \quad (3.11e)$$

It must be noted that first-order (local) homogenisation can be obtained if only the first terms on the right hand-sides of Eq. (3.11) are considered. This yields  $X^m = X^M$ , where X is stiffness, strain, piezomagnetic coupling, magnetic permeability or magnetic field. In this case, material parameters: length- and time-scale do not appear in the macroscopic

continua, and local homogenisation results in classical form of the constitutive equations (see also in [41]). However, non-local homogenisation requires the introduction of second-order terms with  $\delta x$ . Now the constitutive relation for the macroscopic stress and magnetic induction (Eq. (3.10)) can be rewritten as

$$\begin{aligned} \sigma_{ij}^M &= \frac{1}{V_{\text{RVE}_1}} \int_{V_{\text{RVE}_1}} (C_{ijkl}^M \varepsilon_{kl}^M + C_{ijkl}^M \varepsilon_{kl,p}^M \delta x_p + C_{ijkl,o}^M \varepsilon_{kl}^M \delta x_o + C_{ijkl,o}^M \varepsilon_{kl,p}^M \delta x_o \delta x_p) dV \\ &\quad - \frac{1}{V_{\text{RVE}_2}} \int_{V_{\text{RVE}_2}} (q_{kij}^M H_k^M + q_{kij}^M H_{k,p}^M \delta x_p + q_{kij,o}^M H_k^M \delta x_o + q_{kij,o}^M H_{k,p}^M \delta x_o \delta x_p) dV \end{aligned} \quad (3.12a)$$

$$\begin{aligned} B_i^M &= \frac{1}{V_{\text{RVE}_3}} \int_{V_{\text{RVE}_3}} (q_{ikl}^M \varepsilon_{kl}^M + q_{ikl}^M \varepsilon_{kl,p}^M \delta x_p + q_{ikl,o}^M \varepsilon_{kl}^M \delta x_o + q_{ikl,o}^M \varepsilon_{kl,p}^M \delta x_o \delta x_p) dV \\ &\quad + \frac{1}{V_{\text{RVE}_4}} \int_{V_{\text{RVE}_4}} (\mu_{ik}^M H_k^M + \mu_{ik}^M H_{k,p}^M \delta x_p + \mu_{ik,o}^M H_k^M \delta x_o + \mu_{ik,o}^M H_{k,p}^M \delta x_o \delta x_p) dV \end{aligned} \quad (3.12b)$$

In Eq. (3.11), it can be seen that the quantities  $C_{ijkl}^M$ ,  $\varepsilon_{kl}^M$ ,  $q_{kij}^M$ ,  $q_{ikl}^M$ ,  $\mu_{ik}^M$  and  $H_k^M$  are equal to their counterparts  $C_{ijkl}^m$ ,  $\varepsilon_{kl}^m$ ,  $q_{kij}^m$ ,  $q_{ikl}^m$ ,  $\mu_{ik}^m$  and  $H_k^m$  calculated at the centre of the RVE. Hence, these quantities are constant and they can be taken out of the integral in Eq. (3.12) since they are the values at the centre of the RVEs. Assuming a square RVE with its centre acting as origin of a Cartesian coordinate system, the linear terms of  $\delta x$  are cancelled as they consist of odd functions integrated over a symmetric domain. The quadratic terms are integrated by parts as follows

$$\begin{aligned} \int_{V_{\text{RVE}_1}} C_{ijkl,o}^M \varepsilon_{kl,p}^M \delta x_o \delta x_p dV &= \int_S C_{ijkl}^M \varepsilon_{kl,p}^M n_o \delta x_o \delta x_p dS - \int_{V_{\text{RVE}_1}} (C_{ijkl}^M \varepsilon_{kl,op}^M \delta x_o \delta x_p \\ &\quad + C_{ijkl}^M \varepsilon_{kl,p}^M \delta x_{o,o} \delta x_p + C_{ijkl}^M \varepsilon_{kl,p}^M \delta x_o \delta x_{p,o}) dV \end{aligned} \quad (3.13a)$$

$$\begin{aligned} \int_{V_{\text{RVE}_2}} q_{kij,o}^M H_{k,p}^M \delta x_o \delta x_p dV &= \int_S q_{kij}^M H_{k,p}^M n_o \delta x_o \delta x_p dS - \int_{V_{\text{RVE}_2}} (q_{kij}^M H_{k,op}^M \delta x_o \delta x_p \\ &\quad + q_{kij}^M H_{k,p}^M \delta x_{o,o} \delta x_p + q_{kij}^M H_{k,p}^M \delta x_o \delta x_{p,o}) dV \end{aligned} \quad (3.13b)$$

$$\begin{aligned} \int_{V_{\text{RVE}_3}} q_{ikl,o}^M \varepsilon_{kl,p}^M \delta x_o \delta x_p dV &= \int_S q_{ikl}^M \varepsilon_{kl,p}^M n_o \delta x_o \delta x_p dS - \int_{V_{\text{RVE}_3}} (q_{ikl}^M \varepsilon_{kl,op}^M \delta x_o \delta x_p \\ &\quad + q_{ikl}^M \varepsilon_{kl,p}^M \delta x_{o,o} \delta x_p + q_{ikl}^M \varepsilon_{kl,p}^M \delta x_o \delta x_{p,o}) dV \end{aligned} \quad (3.13c)$$

$$\begin{aligned} \int_{V_{\text{RVE}_4}} \mu_{ik,o}^M H_{k,p}^M \delta x_o \delta x_p dV &= \int_S \mu_{ik}^M H_{k,p}^M n_o \delta x_o \delta x_p dS - \int_{V_{\text{RVE}_4}} (\mu_{ik}^M H_{k,op}^M \delta x_o \delta x_p \\ &\quad + \mu_{ik}^M H_{k,p}^M \delta x_{o,o} \delta x_p + \mu_{ik}^M H_{k,p}^M \delta x_o \delta x_{p,o}) dV \end{aligned} \quad (3.13d)$$

where  $n_o$  is a normal vector to surface of domain  $S$ .

Assuming periodic boundary conditions, the boundary integrals vanish and the last two terms in each of Eq. (3.13) are also cancelled since they consist of odd functions. Furthermore, the integrals<sup>2</sup> with  $\delta x_o \delta x_p$  can be evaluated for two-dimensional context as follow

$$\int_{V_{RVE_i}} \delta x_o \delta x_p dV = \int_{-\frac{L_i}{2}}^{\frac{L_i}{2}} \int_{-\frac{L_i}{2}}^{\frac{L_i}{2}} \delta x_o \delta x_p dx_1 dx_3 \quad (3.14a)$$

$$= \frac{1}{12} L_i^4 \delta_{op} \quad (i = 1, 2, 3, 4) \quad (3.14b)$$

where  $\delta_{op}$  is the Kronecker delta,  $V_{RVE_i} = L_i^2$  (for 2D case) and  $L_i$  is the size of the  $i$ th RVE. With these elaborations, the piezomagnetic macroscopic constitutive equations with gradients of strain, magnetic field, and piezomagnetic coupling terms can be expressed as

$$\sigma_{ij}^M = C_{ijkl}^M \left( \varepsilon_{kl}^M - \frac{L_1^2}{12} \varepsilon_{kl,pp}^M \right) - q_{kij}^M \left( H_k^M - \frac{L_2^2}{12} H_{k,pp}^M \right) \quad (3.15a)$$

$$B_i^M = q_{ikl}^M \left( \varepsilon_{kl}^M - \frac{L_3^2}{12} \varepsilon_{kl,pp}^M \right) + \mu_{ik}^M \left( H_k^M - \frac{L_4^2}{12} H_{k,pp}^M \right) \quad (3.15b)$$

In addition to the material coefficients of macroscopic constitutive equations, there are additional coefficients (characteristic length-scale parameters expressed in terms of RVE<sub>*i*</sub> size  $L_i$ ) in Eq. (3.15). It must be pointed out that Eqns. (3.10-3.15) have been derived to motivate and present the application of the determined RVE sizes in the previous chapter. In the current form of the macroscopic constitutive equations, microstructural information can now be taken into account explicitly via additional RVE size parameters in Eq. (3.15). This non-local macroscopic piezomagnetic model should exhibit some advantages over the classical piezomagnetic model (Eq. (1.1)) in accurately describing the material behaviour.

Note that Eq. (3.15) follows the structure of the gradient enriched piezomagnetic model proposed by Xu et al. [61], which is written in terms of phenomenological parameters  $\ell_i$ :

$$\sigma_{ij} = C_{ijkl} (\varepsilon_{kl} - \ell_1^2 \varepsilon_{kl,mm}) - q_{ijk} (H_k - \ell_2^2 H_{k,mm}) \quad (3.16a)$$

$$B_i = q_{ijk} (\varepsilon_{jk} - \ell_2^2 \varepsilon_{jk,mm}) + \mu_{ij} (H_j - \ell_4^2 H_{j,mm}) \quad (3.16b)$$

Comparing Eq. (3.15) and Eq. (3.16), it can be seen that the link between phenomenological parameters, representing internal characteristic length-scale parameter  $\ell_i$ , and RVE sizes  $L_i$  can be established similar to purely elastic context as follows:

$$\ell_i^2 = \frac{L_i^2}{12} \quad (3.17)$$

<sup>2</sup>The detailed integration has been given in Appendix B for the most general 3D case

### 3.3 RVE Sizes and Identification of Characteristic Length-Scale Parameter

In the previous [Chapter 2](#), the detailed methodology to determine the RVE sizes for a magneto-elastic composite material has been presented. It was demonstrated that lower bounds of the RVE sizes can be defined by following the proposed numerically-statistical analysis. As shown, for the analysed MRE material, the difference between the coupling RVE sizes  $L_2$  and  $L_3$  was negligible in line with thermodynamic consistency requirements. Similarly, Xu et al. [61] followed a variational formulation which led to  $\ell_2 = \ell_3$  for reasons of thermodynamic consistency. In this thesis, this issue has been explored by determining the same size for the coupling RVEs  $L_2$  and  $L_3$ , while purely elastic and magnetic RVE sizes  $L_1$  and  $L_4$  are clearly smaller and different. In this context, this chapter provides a novelty in addition to work of Xu et al. [61] by proposing a way to determine the parameter that was presented and prescribed as length-scale parameter ( $\ell$ ) to introduce the microstructural information.

According to numerical results in [Figure 2.6](#), it can be seen that the largest determined RVE size for  $L_2$  and  $L_3$  also covers the lower bound condition for  $L_1$  and  $L_4$ . Therefore, it was concluded and recommended that it is sufficient to use only these largest sizes for practical purposes and set  $L_1 = L_2 = L_3 = L_4 = \max(L_i) \equiv L$  to introduce the magneto-elastic information from micro-level. Eventually, the field equations of the problem on the macro-scale can be obtained by combining the kinematic relations, balance equations and constitutive equations:

$$\varepsilon_{ij}^M = \frac{1}{2}(u_{i,j}^M + u_{j,i}^M) \quad (3.18a)$$

$$H_i^M = -\varphi_{,i}^M \quad (3.18b)$$

$$\sigma_{ij,j}^M = 0 \quad (3.19a)$$

$$B_{i,i}^M = 0 \quad (3.19b)$$

where  $u_i^M$  is the displacement field and  $\varphi^M$  is the scalar magnetic potential on the macro-level. The governing equations in terms of the primary unknowns  $u$  and  $\varphi$  are now:

$$C_{ijkl}^M \left( u_{k,jl}^M - \frac{L^2}{12} u_{k,jlpp}^M \right) + q_{kij}^M \left( \varphi_{,jk}^M - \frac{L^2}{12} \varphi_{,jkpp}^M \right) = 0 \quad (3.20a)$$

$$q_{ikl}^M \left( u_{k,il}^M - \frac{L^2}{12} u_{k,ilpp}^M \right) - \mu_{ik}^M \left( \varphi_{,ik}^M - \frac{L^2}{12} \varphi_{,ikpp}^M \right) = 0 \quad (3.20b)$$

with  $L$  chosen as the largest of the four RVE sizes as discussed above. Here, by using the finite element implementation given for gradient magneto-elasticity by Xu et al. [61], the determined RVE sizes will be used instead of predefined phenomenological length-scale parameters in a generalised magneto-elasticity example.

### 3.4 Finite element formulations

To derive the finite element formulations of the macroscopic model, Eqs (3.18-3.20) are expressed in matrix-vector notation as follow:

$$\boldsymbol{\varepsilon}^M = \mathbf{L}_u \mathbf{u}^M \quad (3.21a)$$

$$\mathbf{H}^M = -\mathbf{L}_\varphi \varphi^M \quad (3.21b)$$

$$\mathbf{L}_u^T \boldsymbol{\sigma}^M = \mathbf{0} \quad (3.22a)$$

$$\mathbf{L}_\varphi^T \mathbf{B}^M = \mathbf{0} \quad (3.22b)$$

$$\mathbf{L}_u^T \mathbf{C}^M \mathbf{L}_u \left( \mathbf{u}^M - \frac{L^2}{12} \nabla^2 \mathbf{u}^M \right) + \mathbf{L}_u^T \mathbf{q}^M \mathbf{L}_\varphi \left( \varphi^M - \frac{L^2}{12} \nabla^2 \varphi^M \right) = \mathbf{0} \quad (3.23a)$$

$$\mathbf{L}_\varphi^T \mathbf{q}^{MT} \mathbf{L}_u \left( \mathbf{u}^M - \frac{L^2}{12} \nabla^2 \mathbf{u}^M \right) - \mathbf{L}_\varphi^T \boldsymbol{\mu}^M \mathbf{L}_\varphi \left( \varphi^M - \frac{L^2}{12} \nabla^2 \varphi^M \right) = 0 \quad (3.23b)$$

where  $\nabla^2 \equiv \nabla^T \cdot \nabla$  is the Laplace operator,  $\mathbf{L}_u$  is the usual strain-displacement derivative operator, and  $\mathbf{L}_\varphi = \nabla$ . It can be realised that finite element implementation of Eq. (3.23) is not straightforward because of the increased continuity requirements of shape functions enforced by gradients.

At this point, Ru and Aifantis [123] developed an approach to solve the certain boundary problems of gradient elasticity in terms of solutions of classical elasticity. As they stated, the fourth-order partial differential equation needs to be solved to obtain the solution (displacement vector) in gradient theory. However, they also showed that various derivatives in gradient theory can be factorised to enable the usage of standard  $C^0$  interpolation functions. This procedure was applied to numerical examples without any magnetic or coupling effects. Afterwards, Askes and co-workers [61, 125] have extended the concept to magneto-elasticity to implement the finite element formulation in gradient piezomagnetic theory. In this method, displacements and magnetic potentials are defined as two different sets by factorising the derivatives.

$$\mathbf{u}^M \text{ and } \mathbf{u}^m = \mathbf{u}^M - \frac{L^2}{12} \nabla^2 \mathbf{u}^M \quad (3.24a)$$

$$\varphi^M \text{ and } \varphi^m = \varphi^M - \frac{L^2}{12} \nabla^2 \varphi^M \quad (3.24b)$$

Here, again superscripts m and M denotes the micro- and macro-scale, respectively. Subsequently, the governing Eq. (3.23) can be expressed as two sets of decoupled equations following the Ru-Aifantis theorem as seen below.

$$\mathbf{L}_u^T \mathbf{C}^M \mathbf{L}_u \mathbf{u}^m + \mathbf{L}_u^T \mathbf{q}^M \mathbf{L}_\varphi \varphi^m = \mathbf{0} \quad (3.25a)$$

$$\mathbf{L}_\varphi^T \mathbf{q}^{MT} \mathbf{L}_u \mathbf{u}^m - \mathbf{L}_\varphi^T \boldsymbol{\mu}^M \mathbf{L}_\varphi \varphi^m = 0 \quad (3.25b)$$

$$\mathbf{u}^m = \mathbf{u}^M - \frac{L^2}{12} \nabla^2 \mathbf{u}^M \quad (3.26a)$$

$$\varphi^m = \varphi^M - \frac{L^2}{12} \nabla^2 \varphi^M \quad (3.26b)$$

Thus, fourth-order governing Eq. (3.23) is now reduced to two sets of second-order equations (3.25) and (3.26). Note that the original form of Eq. (3.23) can be retrieved by substituting (3.26) into (3.25). In this operator split, there are now two distinct displacement and magnetic potential fields: one follows the equations of classical piezomagnetism (3.25), and other influenced by gradient activity (3.26). Under the appropriate boundary conditions, one can obtain the same solution from the decoupled sets as in the original form. For this, Eq. (3.25) is solved first, and the results can be used as input in Eq. (3.26). This approach significantly simplifies analytical and numerical solution strategies [61, 123, 125].

To begin with the solution of the first set of the equations, the weak form of Eq. (3.25) can be derived for domain  $\Omega$  and boundary  $\Gamma$  after integration by parts as follows:

$$\int_{\Omega} (\mathbf{L}_u \mathbf{w}_u)^T \mathbf{C}^M \mathbf{L}_u \mathbf{u}^m d\Omega + \int_{\Omega} (\mathbf{L}_u \mathbf{w}_u)^T \mathbf{q}^M \mathbf{L}_\varphi \varphi^m d\Omega = \int_{\Gamma} \mathbf{w}_u^T \mathbf{t} d\Gamma \quad (3.27a)$$

$$\int_{\Omega} (\mathbf{L}_\varphi \mathbf{w}_\varphi)^T \mathbf{q}^{MT} \mathbf{L}_u \mathbf{u}^m d\Omega - \int_{\Omega} (\mathbf{L}_\varphi \mathbf{w}_\varphi)^T \boldsymbol{\mu}^M \mathbf{L}_\varphi \varphi^m d\Omega = \int_{\Gamma} \mathbf{w}_\varphi^T \mathbf{B}_\perp d\Gamma \quad (3.27b)$$

where  $\mathbf{w}_u$  and  $w_\varphi$  are the test functions,  $\mathbf{t}$  are the boundary tractions, and  $\mathbf{B}_\perp$  is the magnetic traction on the boundary. It must be noted that the weak form (Eq. (3.27)) and finite element equations (Eq. (3.28)) of the first set are the same as Eq. (2.10) and Eq. (2.12) given in the micro-scale analysis for RVE size determination. However, the ma-

terial properties in Eqns. (3.25-3.29) are not described individually for the components, but they are effective macroscopic material properties. Similarly, the standard finite element shape functions of 3 noded triangle elements  $\mathbf{N}_u$  and  $\mathbf{N}_\varphi$  are used for displacements and magnetic potential in 2D. Thus, the finite element formulation is obtained as:

$$\begin{bmatrix} \mathbf{K}_{uu} & \mathbf{K}_{u\varphi} \\ \mathbf{K}_{\varphi u} & -\mathbf{K}_{\varphi\varphi} \end{bmatrix} \begin{bmatrix} \mathbf{d}^m \\ \Psi^m \end{bmatrix} = \begin{bmatrix} \mathbf{F} \\ \Phi \end{bmatrix} \quad (3.28)$$

where  $\mathbf{d}^m$  and  $\Psi^m$  are micro-scale nodal displacement and nodal scalar magnetic potential vectors via  $\mathbf{u}^m = \mathbf{N}_u \mathbf{d}^m$  and  $\varphi^m = \mathbf{N}_\varphi \Psi^m$ . Moreover,  $\mathbf{F}$  and  $\Phi$  are nodal mechanical force and nodal magnetic flux vectors. Lastly, stiffness matrices are given by

$$\begin{aligned} \mathbf{K}_{uu} &= \int_{\Omega} \mathbf{B}_u^T \mathbf{C}^M \mathbf{B}_u d\Omega & \mathbf{K}_{u\varphi} &= \int_{\Omega} \mathbf{B}_u^T \mathbf{q}^M \mathbf{B}_\varphi d\Omega \\ \mathbf{K}_{\varphi u} &= \int_{\Omega} \mathbf{B}_\varphi^T \mathbf{q}^{MT} \mathbf{B}_u d\Omega & \mathbf{K}_{\varphi\varphi} &= \int_{\Omega} \mathbf{B}_\varphi^T \boldsymbol{\mu}^M \mathbf{B}_\varphi d\Omega \end{aligned} \quad (3.29)$$

with  $\mathbf{B}_u = \mathbf{L}_u \mathbf{N}_u$ ,  $\mathbf{B}_\varphi = \mathbf{L}_\varphi \mathbf{N}_\varphi$ .

When the system of equations (3.28) is solved, microscopic displacements and magnetic potentials will be obtained. Afterwards, macroscopic displacements and magnetic potentials in the second set of the equations Eq. (3.26) can be found. As stated, the singularity removing in mechanical and magnetic fields will be addressed in this chapter, and thus macroscopic strains  $\boldsymbol{\varepsilon}$  and magnetic field  $\mathbf{H}$  needs to be calculated in the numerical example. For this purpose, strain and magnetic field based Ru-Aifantis  $\boldsymbol{\varepsilon}$  &  $\mathbf{H}$  – RA approach can be used as proposed by Xu et al. [61]. In this approach, macroscopic strain and magnetic field can be calculated by using the known microscopic displacements and magnetic potentials from the solution of (3.28). As the first step, the derivative of Eq. (3.26) is taken, and then the result are multiplied by relevant constitutive matrices as below:

$$\mathbf{C}^M \mathbf{L}_u \mathbf{u}^m = \mathbf{C}^M \left( \boldsymbol{\varepsilon}^M - \frac{L^2}{12} \nabla^2 \boldsymbol{\varepsilon}^M \right) \quad (3.30a)$$

$$-\boldsymbol{\mu}^M \mathbf{L}_\varphi \varphi^m = \boldsymbol{\mu}^M \left( \mathbf{H}^M - \frac{L^2}{12} \nabla^2 \mathbf{H}^M \right) \quad (3.30b)$$

The weak form of Eq. (3.30) can be derived after integration by parts:

$$\begin{aligned}
 & \int_{\Omega} \mathbf{w}_{\epsilon}^T \mathbf{C}^M \boldsymbol{\epsilon}^M d\Omega + \frac{L^2}{12} \left( \frac{\partial \mathbf{w}_{\epsilon}^T}{\partial x} \mathbf{C}^M \frac{\partial \boldsymbol{\epsilon}^M}{\partial x} + \frac{\partial \mathbf{w}_{\epsilon}^T}{\partial z} \mathbf{C}^M \frac{\partial \boldsymbol{\epsilon}^M}{\partial z} \right) d\Omega \\
 &= \int_{\Omega} \mathbf{w}_{\epsilon}^T \mathbf{C}^M \mathbf{L}_u \mathbf{u}^m d\Omega + \frac{L^2}{12} \int_{\Gamma} \mathbf{w}_{\epsilon}^T (\mathbf{n} \cdot \nabla \mathbf{C}^M \boldsymbol{\epsilon}^M) d\Gamma
 \end{aligned} \tag{3.31a}$$

$$\begin{aligned}
 & \int_{\Omega} \mathbf{w}_H^T \boldsymbol{\mu}^M \mathbf{H}^M d\Omega + \frac{L^2}{12} \left( \frac{\partial \mathbf{w}_H^T}{\partial x} \boldsymbol{\mu}^M \frac{\partial \mathbf{H}^M}{\partial x} + \frac{\partial \mathbf{w}_H^T}{\partial z} \boldsymbol{\mu}^M \frac{\partial \mathbf{H}^M}{\partial z} \right) d\Omega \\
 &= \int_{\Omega} \mathbf{w}_H^T \boldsymbol{\mu}^M \mathbf{L}_{\varphi} \varphi^m d\Omega + \frac{L^2}{12} \int_{\Gamma} \mathbf{w}_H^T (\mathbf{n} \cdot \nabla \boldsymbol{\mu}^M \mathbf{H}^M) d\Gamma
 \end{aligned} \tag{3.31b}$$

where  $\mathbf{w}_{\epsilon}$  and  $\mathbf{w}_H$  are test functions. Next, the finite element equations can be obtained by assuming homogeneous natural boundary conditions for (Eq. (3.31))

$$\begin{bmatrix} \mathbf{G}_{\epsilon} + \frac{L^2}{12} \mathbf{A}_{\epsilon} & 0 \\ 0 & \mathbf{G}_H + \frac{L^2}{12} \mathbf{A}_H \end{bmatrix} \begin{bmatrix} \boldsymbol{\epsilon}^M \\ \mathbf{h}^M \end{bmatrix} = \begin{bmatrix} \mathbf{T}_{\epsilon} & 0 \\ 0 & -\mathbf{T}_H \end{bmatrix} \begin{bmatrix} \mathbf{d}^m \\ \boldsymbol{\Psi}^m \end{bmatrix} \tag{3.32}$$

where  $\boldsymbol{\epsilon}^M$  and  $\mathbf{h}^M$  are macro-scale nodal strains and nodal magnetic field vectors via  $\boldsymbol{\epsilon}^M = \mathbf{N}_{\epsilon} \boldsymbol{\epsilon}^M$  and  $\mathbf{H}^M = \mathbf{N}_h \mathbf{h}^M$ . Additionally, stiffness matrices are:

$$\begin{aligned}
 \mathbf{G}_{\epsilon} &= \int_{\Omega} \mathbf{N}_{\epsilon}^T \mathbf{C}^M \mathbf{N}_{\epsilon} d\Omega & \mathbf{A}_{\epsilon} &= \left( \frac{\partial \mathbf{N}_{\epsilon}^T}{\partial x} \mathbf{C}^M \frac{\partial \mathbf{N}_{\epsilon}}{\partial x} + \frac{\partial \mathbf{N}_{\epsilon}^T}{\partial z} \mathbf{C}^M \frac{\partial \mathbf{N}_{\epsilon}}{\partial z} \right) d\Omega \\
 \mathbf{G}_H &= \int_{\Omega} \mathbf{N}_H^T \boldsymbol{\mu}^M \mathbf{N}_H d\Omega & \mathbf{A}_H &= \left( \frac{\partial \mathbf{N}_H^T}{\partial x} \boldsymbol{\mu}^M \frac{\partial \mathbf{N}_H}{\partial x} + \frac{\partial \mathbf{N}_H^T}{\partial z} \boldsymbol{\mu}^M \frac{\partial \mathbf{N}_H}{\partial z} \right) d\Omega \\
 \mathbf{T}_{\epsilon} &= \int_{\Omega} \mathbf{N}_{\epsilon}^T \mathbf{C}^M \mathbf{B}_u d\Omega & \mathbf{T}_H &= \int_{\Omega} \mathbf{N}_H^T \boldsymbol{\mu}^M \mathbf{B}_{\varphi} d\Omega
 \end{aligned} \tag{3.33}$$

Finally, the solution for the decoupled sets of equations can be obtained by solving Eq. (3.28) first, and then the results (micro-scale displacements  $\mathbf{d}^m$  and magnetic potentials  $\boldsymbol{\Psi}^m$ ) are used as input in Eq. (3.32) to calculate the macroscopic strains and magnetic field in a macro-scale model. Now, the effectiveness of using a gradient piezo-magnetic model which includes determined RVE sizes can be addressed.

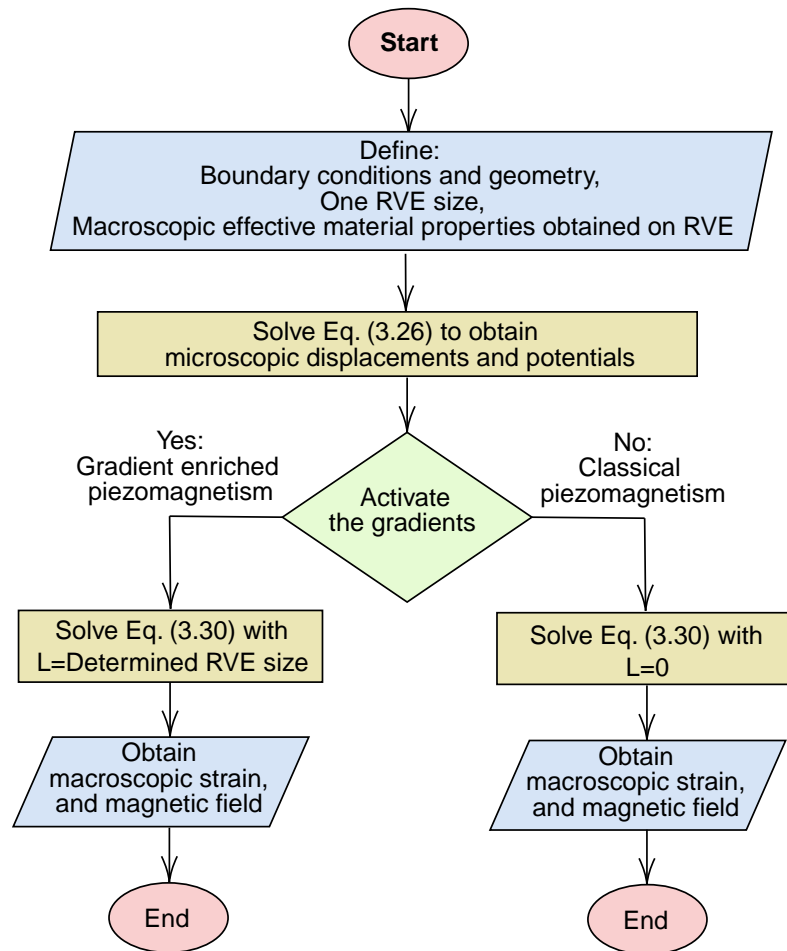


**Figure 3.1:** Procedure of gradient enriched piezomagnetic model solution

### 3.5 Removal of singularities

In this section, the standard benchmark numerical example, demonstrating the removal of singularities in mechanical and magnetic fields, will be analysed to demonstrate the performance of the model. The detailed finite element implementation of gradient enriched piezomagnetic continuum model considering microstructural information via the RVE size has been presented in previous section.

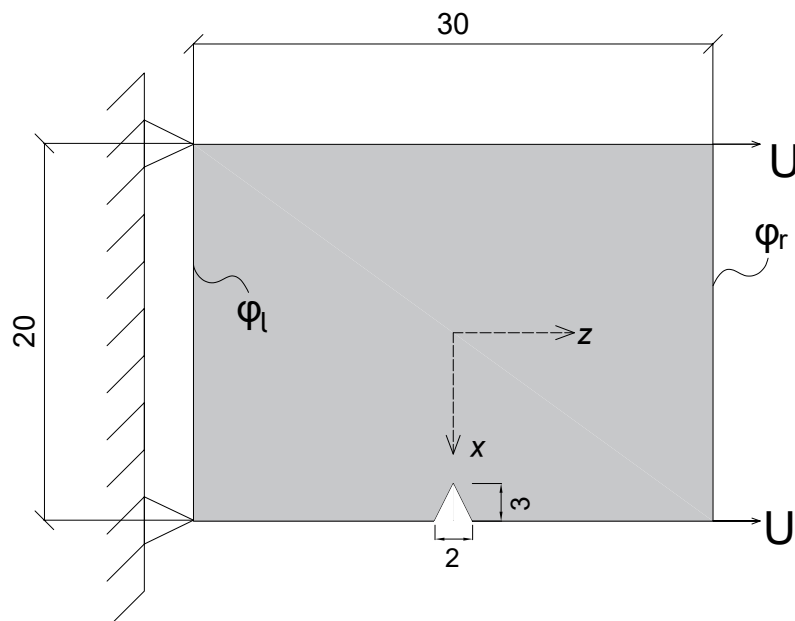
It is well-known that singularities can be observed in case of sudden changes in the boundary conditions or at the sharp corners in a model when the classical elasticity is used. On the contrary, gradient elasticity with appropriate boundary conditions can prevent these singularities as shown by researchers [123, 124, 126, 127]. Therefore, a numerical example will be presented demonstrating the removing of singularities to study the influence of gradient piezomagnetic formulation, and investigate the difference from the classical piezomagnetic formulation. Accordingly, a MATLAB code has been developed in-house to create an MRE plate with a notch, and solve the finite element formulations (see Figure 3.1). Singularities are expected to appear at the tip of the notch if classical theory is employed.

In the numerical example, a homogeneous MRE plate (Terfenol-D-epoxy composite) was modelled on the macro-scale, with the effective properties as given in Table 3.1. The effective material properties have been calculated via homogenisation of the constituents's properties (Table 2.1) on the determined RVE given in the previous Chapter. Plane stress condition is considered, and external loadings were applied as shown in Figure 3.2a. The plate is polarized along the  $z$  direction with prescribed displacements  $U = 0.1$  mm and scalar magnetic potentials on the left and right edges to create an external magnetic field of  $H_z = 20$  kA/m. Finite element discretisation was achieved by using linear triangular elements, and the mesh was created as seen in Figure 3.2b. As discussed, it was assumed that  $L_1 = L_2 = L_3 = L_4 \equiv L$  in Eq. (3.20), and  $L$  is the size of the RVE determined as 2.3 mm (see Figure 2.6). The notch in the plate has been modelled as an inclusion with vacuum permeability, and zero values for elastic constants, piezomagnetic constants and RVE size  $L$  to represent a void. Under these conditions, the distributions of strain  $\boldsymbol{\varepsilon}$  and magnetic field  $\mathbf{H}$  components was calculated along  $z$  axis to analyse the singularities at the tip of the notch.

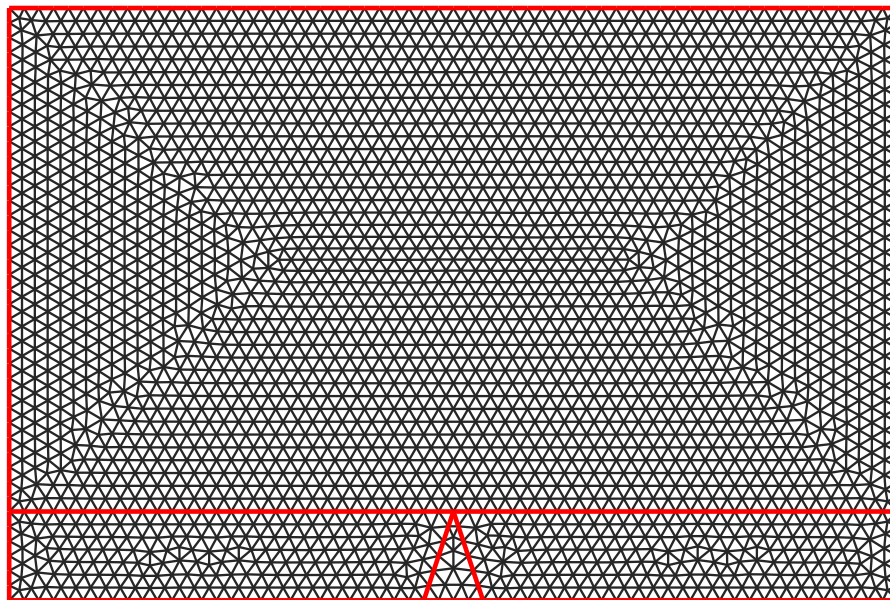
	$C_{11}$	$C_{13}$	$C_{33}$	$C_{55}$	$q_{31}$	$q_{33}$	$q_{15}$	$\mu_{11}$	$\mu_{33}$
<b>MRE Plate</b>	15.5	10	19	2.3	-9	57	20.3	3.4	1.4

$C_{ij}$  in GPa,  $q_{ij}$  in N/Am,  $\mu_{ij}$  in  $10^{-6}$ N/A<sup>2</sup>

**Table 3.1:** Effective material properties of MRE plate



(a) Macro-scale MRE Plate with a crack



(b) Mesh of the plate

**Figure 3.2:** MRE Plate with a crack and finite element discretisation (Units: mm and thickness=5 mm)

Figure 3.3 presents the distributions of  $\boldsymbol{\varepsilon}$  and  $\mathbf{H}$  components in the  $z$ -direction, indicated by a solid red line, passing through the notch tip in Figure 3.2. To investigate the effectiveness of the gradient formulation, two different cases have been considered: one with the RVE size  $L = 2.3$  mm that considers the gradients, and the other with the RVE size  $L = 0$  that represents the classical piezomagnetism in which the microstructural information is absent. It can be seen (Figure 3.3) that using the gradient enhanced, RVE-based piezomagnetic formulation can effectively remove the singularities of all  $\boldsymbol{\varepsilon}$  and  $\mathbf{H}$  components, while singularities appear at the notch tip for the classical formulation.

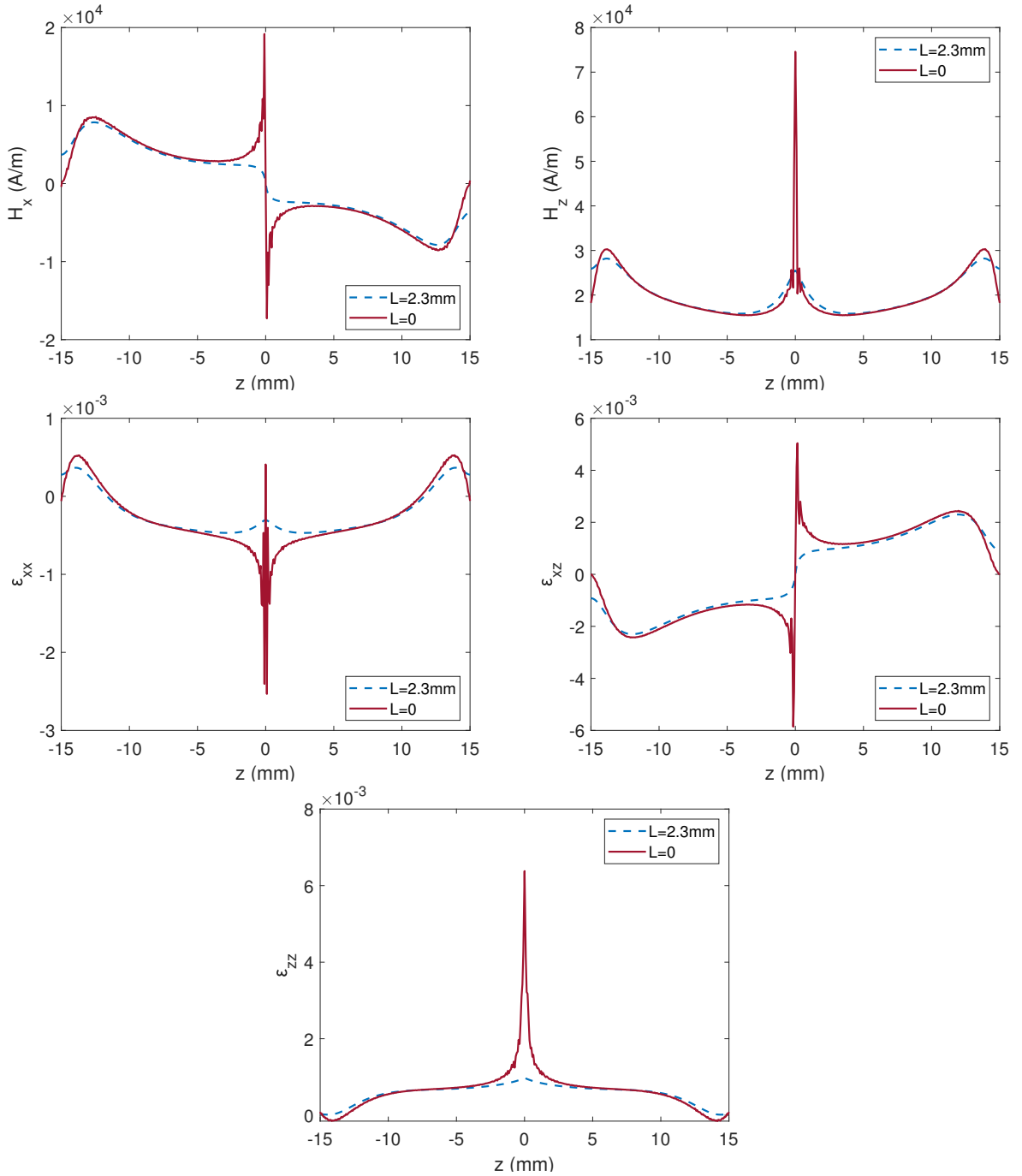


Figure 3.3:  $\boldsymbol{\varepsilon}$  and  $\mathbf{H}$  distributions along  $z$ -axis based on  $\boldsymbol{\varepsilon}\&\mathbf{H} - \text{RA}$  approach

It must also be noted that a similar problem has been addressed by Xu et al. [61] by using predefined characteristic length-scale parameter  $\ell = 0.5$  mm instead of the RVE size  $L$  for an MRE material. Their work have also provided qualitatively similar results by removing the mechanical and magnetic singularities. Therefore, the result of this chapter also verifies the appropriateness of using the RVE size as a model parameter in gradient formulation.

## 3.6 Discussion

In this chapter, a piezomagnetic continuum model has been developed with gradients of strain, piezomagnetic coupling and magnetic field whereby the microstructural characteristic length-scale parameters are expressed in terms of RVE sizes. Second-order (or non-local) homogenisation scheme has been summarised, and adopted in magneto-elastic framework. This technique results in the appearance of length-scale parameters as linear functions of the related RVE size in macroscopic piezomagnetic constitutive relations. By establishing this link, the second and final step of considering the microstructural information on the macro-level magneto-elastic behaviour was achieved.

According to the conclusions of RVE size determination study given in Chapter 2, previously defined RVE sizes have been assumed to be same and equal to  $L = 2.3$  mm. It was shown that gradient enriched piezomagnetic model (with RVEs) presents more accurate description of material behaviour compared to a classical piezomagnetic model. For this, an in-plane problem has been addressed with this generalised magneto-elastic continuum model. A solution scheme was formulated and implemented based on the finite element method and the extended Ru-Aifantis theorem adopted from the study given by Xu et al. [61]. In the continuum model, representative volume elements (RVEs) were included to introduce the microstructural information to the macroscopic behaviour of the material. By using the determined model parameter RVE size  $L$ , it was observed that the singularities can be removed at the tip of a notch in mechanical and magnetic fields for a homogenised MRE (Terfenol-D/polymer) plate on the macro-scale. However, classical piezomagnetic model with  $L = 0$  mm, which also means not considering the microstructure, has presented spiky values (singularities) at the notch tip for macroscopic mechanical strain and magnetic field distributions. Additionally, a comparison has been made between using determined RVE size and predefined length-scale as given by Xu et al. [61] for the same problem in the work of Eraslan et al. [117]. It was seen that both

approach very present similar results (remove singularities), and thus it was suggested that a length scale can also be prescribed quantitatively by using the relation with the RVE size as given in [Eq. \(3.17\)](#).

In summary, significance of the microstructural influence on a macro-level modelling in a magnetostrictive composite material has been demonstrated, and the static aspect of this thesis can now be concluded. The motivation in statics analysis was to remove the singularities in mechanical and magnetic fields, and this was achieved by using RVE size as model parameter in macroscopic non-local piezomagnetic continua. Next, a dynamic aspect of the magneto-elastic composites motivated by a phenomenon called stop-band behaviour will be studied in the context of this study.

# Chapter 4

## Effects of randomness and piezomagnetic coupling on the appearance of stop-bands in MREs

It is well known that the behaviour of heterogeneous materials differs significantly from their homogeneous counterparts, when a dynamic loading is applied specifically when acoustic and/or elastic waves propagate through a material. This difference is attributed to existence of wave dispersion due to the change in medium properties, i.e. density and elastic constants of the constituents. A considerable effort has been put on the study of elastic wave propagation in composite materials by theoretical and experimental studies [92, 95–99, 128–132].

Composite materials with periodic arrangement of inclusions embedded in a matrix are called as phononic crystals (PCs) and they show a well-known phenomenon referred to as stop-band (or wave band-gap). Stop-band is a band of frequencies, where elastic wave propagation and vibrations are suppressed in certain frequency ranges [90, 91, 95–97, 133, 134]. In the case of magnetostrictive composites (or MREs), the arrangement of magnetic particles or fibres can be non-periodic. Magnetic inclusions can be distributed randomly (as discussed in previous chapters). It is thus of interest to analyse the wave propagation phenomenon and stop-bands in MREs in this chapter<sup>1</sup>. Complete frequency gaps have much potential for applications such as acoustic filters, reflectors, waveguides,

---

<sup>1</sup>This chapter is directly adopted from:

Eraslan, S., Gitman, I., Askes, H. et al. Effects of randomness and piezomagnetic coupling on the appearance of stop-bands in heterogeneous magnetorheological elastomers. Arch Appl Mech 93, 3259–3273 (2023) [135]

switches and vibration isolation [88–92]. Controlling and tuning the characteristics (e.g. position and the width) of stop-bands and analysing the effective parameters influencing these properties are therefore important topics for investigation, allowing to create more effective designs or enhance the functionality of composites. It is known that the stop-band attributes can be influenced by inclusion geometry, lattice pattern, volume fraction and elastic characteristics of the constituents [91,97,99,100]. Potential advantages of an MRE material over an elastic composite material that does not exhibit coupled behaviour will be investigated. Moreover, the influential parameters on the stop-bands characteristics will be analysed.

## 4.1 Magneto-elastic materials and wave band-gaps

Stimuli-responsive composite materials have also been extensively studied in wave propagation problems as they offer potential for superior features compared to conventional materials, in particular improved and controllable physical properties [89,90,99,101–104]. As has been mentioned, material and geometrical properties of a composite are influential parameters in wave propagation behaviour, and these features can be affected by the external stimuli in case of using responsive materials as inclusions in PCs. Consequently, the idea of tuning and optimising the stop-bands have taken a great interest, and thus these materials have become attractive and promising candidates for stop-band tunability purposes.

Specifically, PCs with piezoelectric or piezomagnetic constituents show some advantages compared to purely elastic PCs such as quick response, controllability and reversibility [101]. Bou et al. [91] pointed out that large magnitudes of stimuli are needed to tune stop-band characteristics for electrorheological materials (or indeed temperature change) while magneto-elastic materials are very sensitive to external magnetic fields and their magnetic state. This feature makes magneto-elastic materials suitable candidates for contactless controllable PCs. They have already shown contactless tunability of stop-bands via the magnetic field dependent piezomagnetic material model for 2D PCs composed of Terfenol-D and an epoxy matrix [91]. It was concluded that introduction of magneto-elastic coupling can lead to some potentially advantageous effects on the band gap properties, such as an increase in bandwidth of the first stop-band range and the creation of a second stop-band range [89,91,102].

The influence of an external static magnetic field on band gaps of Lamb waves in PC

slabs has been studied by Zhou et al. [88]. They concluded that the width of the first band gap can be changed significantly with a change in amplitude of the magnetic field, which can have potential applications in vibration isolation. Similarly, Ding et al. [90] have considered 1D magneto-elastic phononic crystals analysing and tuning longitudinal wave band gap properties. In addition to the static magnetic field, it was shown that filling fraction, pre-stress and thermal conditions can also influence band gap properties noticeably. Furthermore, elastic wave propagation in 2D magnetoelectroelastic materials has been investigated by Wang et al. [99, 113] to understand the effects of lattice geometry and coupling effects on the band gap characteristics. They demonstrated that the first band gap width is larger for triangular and square patterns as opposed to hexagonal geometries, and this difference increases with the filling ratio. On the other hand, piezoelectric and piezomagnetic effects have a significant influence (especially in high filling ratios) on the width of the higher band gaps.

Moreover, small size PCs have been developed with the advancements in micro- and nano-electromechanical systems [136–138]. Hence, non-local theories were also developed to study size-dependent wave propagation behaviour and stop-bands in magneto-elastic PCs. Hu et al. [136] have derived the governing equation of Terfenol-D/epoxy nano PCs considering the non-local effects and piezomagnetic coupling on the stop-band structures. They concluded that incorporating the non-local parameter in the model results in enlarged edges and width of the stop-band. Classical continuum theory is not sufficient to describe the dispersive wave propagation due to lack of terms incorporating microstructural information in macroscopic continua. Xu et al. [139, 140] have presented a dynamic piezomagnetic model with gradient enrichments and transient effects to describe the wave dispersion in generalised magneto-elastic continua. They showed that the model can predict the wave dispersion, and dispersive properties are controlled by the ratio of the length-scale parameters employed for strain and acceleration.

Besides the parameters influencing the stop-band characteristics of PCs as summarized above, Song et al. [97, 105] demonstrated that geometrical and mechanical randomness also affect the stop-band frequencies in an elastic material. In particular, these authors showed that randomness in the geometry causes much more significant changes on the stop-bands compared to randomness in mechanical properties. Even for moderate perturbations in the geometry, the second pass band decreases dramatically, both in width and in transmission coefficient, and ultimately the second pass-band can be turned into a stop-band for a sufficiently high degree of geometric randomness.

The aim of this chapter is to analyse longitudinal wave propagation and stop-band behaviour in magneto-elastic composite materials and to investigate the combined influence of magneto-elastic coupling and randomness. The influence of the size and volume fraction of magnetic inclusions will be studied with and without magneto-elastic coupling. Randomness will be introduced in the magnetic inclusions' sizes and positions separately as well as simultaneously to analyse possible effects of randomness. The finite element formulation will be described that has been used to simulate magneto-elastic wave propagation. The test setup and the algorithm of analysis will also be given to study the effects of periodicity, randomness, particles sizes, volume fraction, and coupled versus decoupled behaviour.

## 4.2 Continuum equations and discretisation aspects

To describe the longitudinal wave propagation in a heterogeneous MRE material, finite element discretisation of the equation of motion for a piezomagnetic material will be derived. For the ease of readability, some common points with the static formulation such as kinematic relations, stiffness matrices etc. will be reiterated. As discussed in [Chapter 1](#), magnetostrictive materials show non-linear material behaviour, but they can be described by linear piezomagnetic laws in a certain range of operation. This range can be obtained by considering only variations around the initial magnetic bias and the mechanical pre-stress conditions [78]. The constitutive equations of a linear piezomagnetic medium in vector notation are given as [18, 77–82]

$$\boldsymbol{\sigma} = \mathbf{C}\boldsymbol{\varepsilon} - \mathbf{q}\mathbf{H} \quad (4.1a)$$

$$\mathbf{B} = \mathbf{q}^T\boldsymbol{\varepsilon} + \boldsymbol{\mu}\mathbf{H} \quad (4.1b)$$

The equation of motion can be written as:

$$\mathbf{L}_u^T\boldsymbol{\sigma} = \rho\ddot{\mathbf{u}} \quad (4.2a)$$

$$\mathbf{L}_\varphi^T\mathbf{B} = 0 \quad (4.2b)$$

Combining Eqns. (4.1-4.2) with the kinematic relations  $\boldsymbol{\varepsilon}=\mathbf{L}_u\mathbf{u}$  and  $\mathbf{H} = -\mathbf{L}_\varphi\varphi$  yields

$$\mathbf{L}_u^T\mathbf{C}\mathbf{L}_u\mathbf{u} + \mathbf{L}_u^T\mathbf{q}\mathbf{L}_\varphi\varphi = \rho\ddot{\mathbf{u}} \quad (4.3a)$$

$$\mathbf{L}_\varphi^T\mathbf{q}^T\mathbf{L}_u\mathbf{u} - \mathbf{L}_\varphi^T\boldsymbol{\mu}\mathbf{L}_\varphi\varphi = 0 \quad (4.3b)$$

where  $\rho$  is the mass density, and a superimposed dot denotes a time derivative. As known,  $\mathbf{L}_\varphi = \nabla$  and  $\mathbf{L}_u$  is the usual strain-displacement derivative operator,  $\mathbf{u}$  is the displacement field,  $\varphi$  is the scalar magnetic potential.

Similarly, the weak form of Eq.(4.3) can be written for domain  $\Omega$  and boundary  $\Gamma$  after integration by parts to obtain the finite element formulation as follows:

$$\int_{\Omega} \mathbf{w}_u^T \rho \ddot{\mathbf{u}} d\Omega + \int_{\Omega} (\mathbf{L}_u \mathbf{w}_u)^T \mathbf{C} \mathbf{L}_u \mathbf{u} d\Omega + \int_{\Omega} (\mathbf{L}_u \mathbf{w}_u)^T \mathbf{Q} \mathbf{L}_\varphi \varphi d\Omega = \int_{\Gamma} \mathbf{w}_u^T \mathbf{t} d\Gamma \quad (4.4a)$$

$$\int_{\Omega} (\mathbf{L}_\varphi \mathbf{w}_\varphi)^T \mathbf{Q}^T \mathbf{L}_u \mathbf{u} d\Omega - \int_{\Omega} (\mathbf{L}_\varphi \mathbf{w}_\varphi)^T \boldsymbol{\mu} \mathbf{L}_\varphi \varphi d\Omega = \int_{\Gamma} \mathbf{w}_\varphi^T \mathbf{B}_\perp d\Gamma \quad (4.4b)$$

where  $\mathbf{w}_u$  and  $w_\varphi$  are the test functions,  $\mathbf{t}$  are the boundary tractions, and  $\mathbf{B}_\perp$  is the magnetic traction on the boundary. Thus, the following system of equations is obtained:

$$\begin{bmatrix} \mathbf{M} & \mathbf{0} \\ \mathbf{0} & \mathbf{0} \end{bmatrix} \begin{bmatrix} \ddot{\mathbf{d}} \\ \mathbf{0} \end{bmatrix} + \begin{bmatrix} \mathbf{K}_{uu} & \mathbf{K}_{u\varphi} \\ \mathbf{K}_{\varphi u} & -\mathbf{K}_{\varphi\varphi} \end{bmatrix} \begin{bmatrix} \mathbf{d} \\ \boldsymbol{\Psi} \end{bmatrix} = \begin{bmatrix} \mathbf{F} \\ \boldsymbol{\Phi} \end{bmatrix} \quad (4.5)$$

where  $\mathbf{d}$  and  $\boldsymbol{\Psi}$  are nodal displacement and nodal scalar magnetic potential vectors via  $\mathbf{u} = \mathbf{N}_u \mathbf{d}$ ,  $\ddot{\mathbf{u}} = \mathbf{N}_u \ddot{\mathbf{d}}$  and  $\varphi = \mathbf{N}_\varphi \boldsymbol{\Psi}$ . Moreover,  $\mathbf{F}$  and  $\boldsymbol{\Phi}$  are nodal mechanical force and nodal magnetic flux vectors. Lastly, stiffness and mass matrices are given by

$$\begin{aligned} \mathbf{M} &= \int_{\Omega} \rho \mathbf{N}_u^T \mathbf{N}_u d\Omega \quad , \quad \mathbf{K}_{uu} = \int_{\Omega} \mathbf{B}_u^T \mathbf{C} \mathbf{B}_u d\Omega \quad , \quad \mathbf{K}_{u\varphi} = \int_{\Omega} \mathbf{B}_u^T \mathbf{Q} \mathbf{B}_\varphi d\Omega \\ \mathbf{K}_{\varphi u} &= \int_{\Omega} \mathbf{B}_\varphi^T \mathbf{Q}^T \mathbf{B}_u d\Omega \quad , \quad \mathbf{K}_{\varphi\varphi} = \int_{\Omega} \mathbf{B}_\varphi^T \boldsymbol{\mu} \mathbf{B}_\varphi d\Omega \end{aligned} \quad (4.6)$$

with  $\mathbf{B}_u = \mathbf{L}_u \mathbf{N}_u$ ,  $\mathbf{B}_\varphi = \mathbf{L}_\varphi \mathbf{N}_\varphi$ . Similar to static case, the matrices  $\mathbf{N}_u$  and  $\mathbf{N}_\varphi$  contain the relevant shape functions of linear triangular finite elements.

In order to solve the finite element form of equations of motion (Eq. (4.5)) for the longitudinal wave propagation behaviour, a time integration method is required. Here, the constant average acceleration variant of the Newmark integration method has been used with the parameters  $\gamma = 0.5$  and  $\beta = 0.25$  since they provide unconditionally stable solutions:

$$\begin{aligned} \dot{\mathbf{u}}^{t+\Delta t} &= \dot{\mathbf{u}}^t + (1 - \gamma)\Delta t \ddot{\mathbf{u}}^t + \gamma\Delta t \ddot{\mathbf{u}}^{t+\Delta t} \\ \mathbf{u}^{t+\Delta t} &= \mathbf{u}^t + \Delta t \dot{\mathbf{u}}^t + (0.5 - \beta)\Delta t^2 \ddot{\mathbf{u}}^t + \beta\Delta t^2 \ddot{\mathbf{u}}^{t+\Delta t} \end{aligned} \quad (4.7)$$

where  $\mathbf{u}$ ,  $\dot{\mathbf{u}}$  and  $\ddot{\mathbf{u}}$  are displacement, velocity and acceleration respectively. The superscript  $t$  denotes the current time step,  $t + \Delta t$  the next time step, and  $\Delta t$  the time interval.

### 4.3 Numerical test setup

The numerical test setup has been constructed as given in Figure 4.1. In addition to test material (here - MRE), different artificial bodies namely perfectly matched layers (PMLs), source and receiver parts have been created to generate and simulate the propagation of the longitudinal wave. The test material (MRE) consists of polymer matrix and piezomagnetic particles. The details of the test material will be presented and discussed in the following sections.

It is known that reflections either from the interface between the parts or from the ends of the geometry can significantly affect the results in a wave propagation analysis. So-called perfectly matched layers (PMLs) are often used in numerical simulations to absorb the waves, so that unwanted reflections can be avoided [97]. Additionally, it was pointed out that spurious reflections can pollute the results, if the difference in compressional wave speeds between the PMLs and source/receiver parts is too large [97]. Therefore, two PMLs have been created in the test setup to reduce this numerical noise.

The roles of the source and receiver parts were to generate and record the incident wave during the simulation.

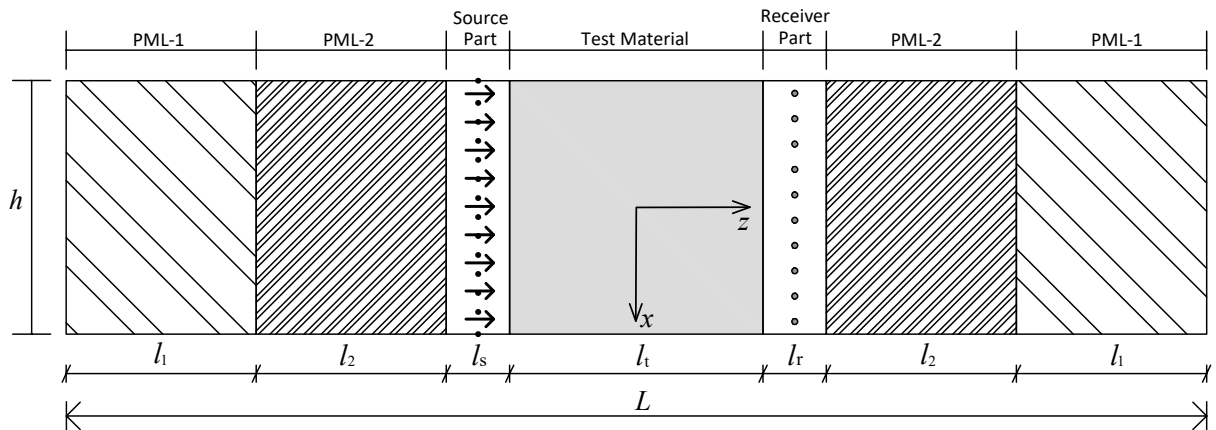


**Figure 4.1:** Numerical model of simulation

The test material (MRE) has been placed between PMLs and artificial source/receiver regions to simulate the longitudinal waves propagating in the test material along the  $z$  axis. Here, the superscripts 1, 2, s and r represent the first PML, the second PML, source and receiver regions respectively. The acoustic impedance of PMLs and source/receiver parts should be identical to provide a smooth transition between the various parts and low compressional wave speeds in the PMLs [97]. Therefore, the material properties have been taken as

$$\begin{aligned}
\rho^s &= \rho^r & \rho^2 &= 10\rho^s & \rho^1 &= 50\rho^s \\
\mathbf{C}^s &= \mathbf{C}^r & \mathbf{C}^2 &= 0.1\mathbf{C}^s & \mathbf{C}^1 &= 0.02\mathbf{C}^s
\end{aligned} \tag{4.8}$$

where  $\rho$  is the mass density and  $\mathbf{C}$  is the stiffness tensor. Thus, the compressional matching impedance has been achieved via  $\sqrt{\rho^s C_{33}^s} = \sqrt{\rho^r C_{33}^r} = \sqrt{\rho^1 C_{33}^1} = \sqrt{\rho^2 C_{33}^2}$ , where  $C_{33}$  is the stiffness in direction of longitudinal wave propagation along the  $z$  axis. Furthermore, the compressional wave speed in the various parts follows from

$$\begin{aligned}
v_{\text{comp.}}^s &= v_{\text{comp.}}^r \\
v_{\text{comp.}}^2 &= \sqrt{\frac{C_{33}^2}{\rho^2}} = 0.1v_{\text{comp.}}^s \\
v_{\text{comp.}}^1 &= \sqrt{\frac{C_{33}^1}{\rho^1}} = 0.02v_{\text{comp.}}^s
\end{aligned} \tag{4.9}$$

	Test material	Source/receiver	PML-1/PML-2
<b>Length (<math>l</math>)</b>	2	0.5	1.5
<b>Height (<math>h</math>)</b>	2	2	2

**Table 4.1:** Size of the parts in the test setup (sizes in mm).

The sizes of the parts in the test setup have been chosen as seen in [Table 4.1](#). With these elaborations, the numerical process to simulate the longitudinal wave propagation, and identify stop-bands/pass-bands can be given as follows:

1. Mechanical boundary conditions have been prescribed as  $u_z(-\frac{L}{2}) = u_z(\frac{L}{2}) = 0$ ,  $u_x(-\frac{L}{2}) = u_x(\frac{L}{2}) = 0$  and  $u_x(-\frac{h}{2}) = u_x(\frac{h}{2}) = 0$  where  $u_x$  and  $u_z$  are horizontal and vertical displacements. Magnetic boundary conditions have been set up by defining scalar magnetic potentials  $\varphi^s$  and  $\varphi^r$  on the nodes of source and receiver lines (at the middle of the source/receiver parts, see [Figure 4.1](#)) to create a static magnetic field  $H_z$  in the test material. Scalar magnetic potentials on the receiver/source lines have been assigned to create 5 kA/m of magnetic field that corresponds to a small variation around bias field [78]. Lastly, initial conditions at  $t = 0$  have been defined as  $\mathbf{v} = 0$ ,  $\mathbf{u} = 0$ ,  $\varphi^s = 0$ , and  $\varphi^r = 0$  where  $\mathbf{v}$  is the nodal velocity vector.

2. A continuous harmonic longitudinal sine wave is activated at the source line by applying nodal forces  $F_g = A_g \sin(\omega t)$  where  $A_g$  is the amplitude,  $\omega$  is the angular frequency and  $t$  is time. This longitudinal wave propagates in the positive  $z$  direction through the test material (MRE) and the displacements on the receiver line are recorded.
3. For each frequency, two simulations are set: one with a heterogeneous test material, and one with the equivalent homogeneous test material. In the homogenous setup, material properties of the test material are averaged from magnetic particle and polymer matrix according to the rule of mixtures. In the heterogeneous setup, constituents have their individual material properties. The material properties of the source and receiver parts are assigned to be the averaged properties in both simulations.
4. To have the amplitudes of propagated incident wave for both homogeneous ( $A_h$ ) and heterogeneous ( $A_c$ ) setup, a Fourier transform is applied to the recorded displacements at the end of each simulation. It is known that wave propagation is non-dispersive in homogeneous materials, and each individual harmonic travels with the same velocity. However, the wave propagation will show a dispersive behaviour in the case of heterogeneous materials, and an inability of certain harmonic components to propagate may occur. The amplitude variance between the homogeneous and heterogeneous configurations will be used to define the transmission coefficient. Displacements are recorded on ten equally spaced nodes (recording points) at the receiver line during the simulation. Finally, a transmission coefficient is defined as

$$T = \frac{A_c}{A_h} \quad (4.10)$$

In this thesis, it was assumed that if the transmission coefficient is less than 10%, the relevant harmonic component can be considered as “stopped”. This process has been followed for a range of frequencies to determine the stop-band frequencies. By varying microstructural properties of the test material and applying or switching off magnetic field, the effects of microstructure and magneto-elastic coupling can be measured and assessed in a systematic manner. The procedure of the numerical process has also been summarised in [Figure 4.2](#).

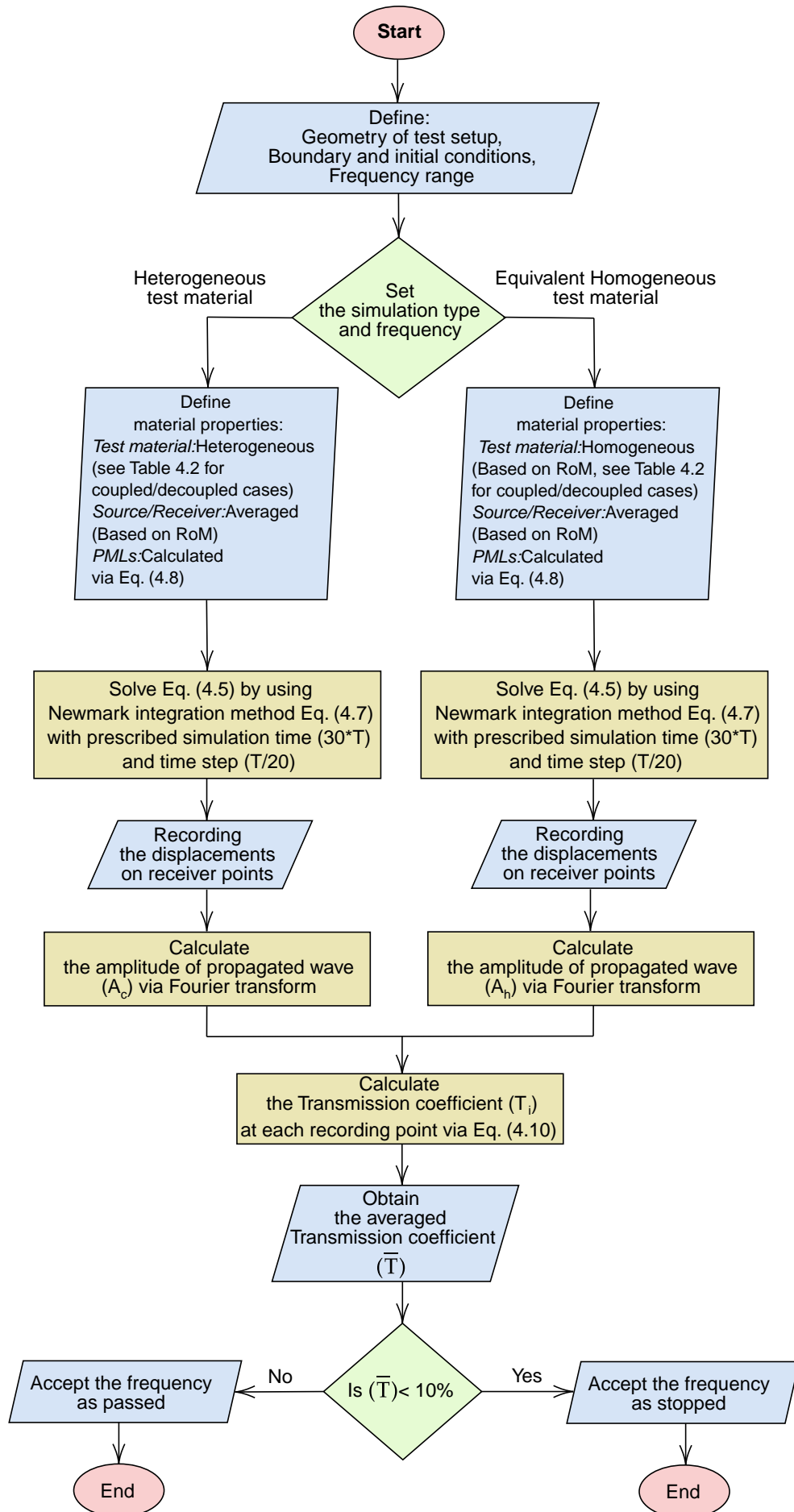


Figure 4.2: Procedure of wave propagation and stop-band analysis

## 4.4 Results and analysis of influential parameters on stop-bands

In the numerical analysis, material properties of magnetostrictive Terfenol-D particles and polymer matrix material have been adopted as given in Table 4.2 (note that this material is similar to the one analysed in previous chapters). The polymer matrix has been modelled to be a non-magnetisable material. To represent the non-magnetisable polymer, piezomagnetic constants of the matrix have been assumed as zero, and the magnetic permeability of the matrix has been taken as the magnetic permeability of air. Damping of the constituents have been assumed as zero to simplify the analysis [93], and volume fractions of particles  $V_f$  have been chosen as 30% and 45% (for different tests). A continuous harmonic force function has been applied with an amplitude ( $A_g$ ) of 1 Newton during the simulation time which has been set to be equal 30 periods of the wave to ensure that sufficient periods have propagated and been recorded. To describe the wave propagation accurately, approximately 6 finite elements per wavelength were used in the test material. The studied frequency range has been set to be 0.5 – 7.0 MHz.

		$C_{11}$	$C_{13}$	$C_{33}$	$C_{55}$	$q_{31}$	$q_{33}$	$q_{15}$	$\mu_{11}$	$\mu_{33}$	$\rho$
<b>Coupled</b>	<b>Terfenol-D [78]</b>	27	11.8	31.4	4.2	-15.2	217	68	9	1.86	9250
	<b>Polymer [113]</b>	7.8	4.8	7.8	1.6	0	0	0	$\mu_0$	$\mu_0$	1150
<b>Decoupled</b>	<b>Terfenol-D [78]</b>	27	11.8	31.4	4.2	0	0	0	$\mu_0$	$\mu_0$	9250
	<b>Polymer [113]</b>	7.8	4.8	7.8	1.6	0	0	0	$\mu_0$	$\mu_0$	1150

$C_{ij}$  in GPa,  $q_{ij}$  in N/Am,  $\mu_{ij}$  in  $10^{-6}$ N/A<sup>2</sup>,  $\rho$  in kg/m<sup>3</sup>

**Table 4.2:** Material properties of test material

As mentioned above, the effects of piezomagnetic coupling and microstructure of the MRE have been investigated in this chapter. To study the coupling effect, the piezomagnetic coupling properties of the particles have been assigned as zero and non-zero (see Table 4.2) to simulate decoupled and coupled physics. Moreover, the magnitude of the external magnetic field  $H_z$  has been set to be 0 kA/m for the decoupled case, and 5 kA/m for the coupled case in the  $z$  direction.

In the evaluation of the microstructure, attributing to earlier studies given in purely

elastic decoupled context [93,97,105], periodic and random particle distributions have been created for the test material. A Matlab code (by using PdeToolbox) developed in-house has been used to create the test geometries. To this end, alongside periodic material (a), randomness has been introduced in terms of particle size only (b), particle position only (c), and both size and position simultaneously (d) as depicted qualitatively in Figure 4.3.

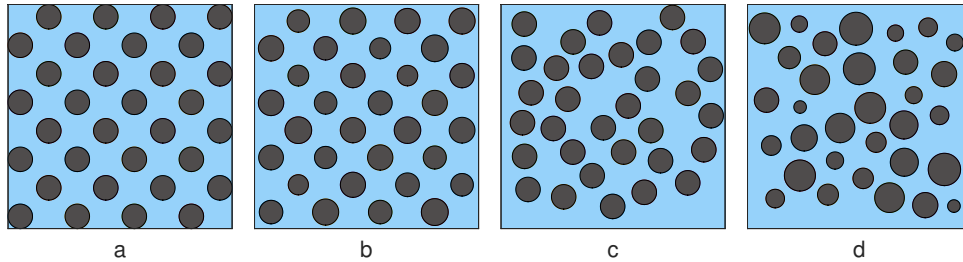


**Figure 4.3:** Example of test materials. Periodic (a), randomness in particle size (b), position (c) and both (d). ( $V_f = 30\%$ )

#### 4.4.1 Periodic microstructure

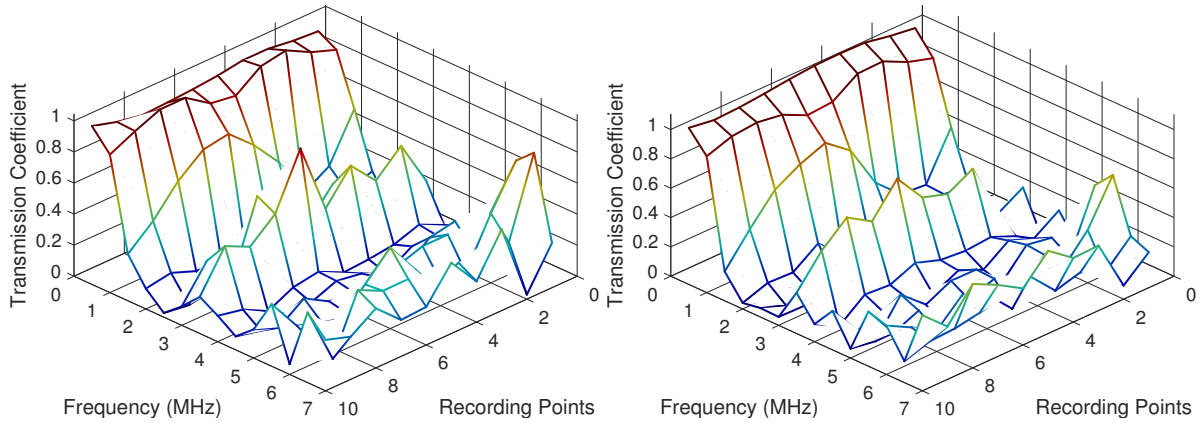
The first analysis has been done for a periodic test material (Figure 4.3a), which will serve as a benchmark for all subsequent tests.

##### Influence of magneto-elastic coupling

In this first study, the influence of piezomagnetic coupling on the wave propagation in periodic material has been evaluated. The transmission coefficients on the recording points have been calculated for each frequency as seen in Figure 4.4 for the decoupled (left) and the coupled (right) cases. On the recording points, the values of the transmission coefficients are relatively lower at some frequencies (around 2.5 and 4.5 MHz) in addition to being similar. Conversely, they have shown a varied and higher distribution at some other frequencies (around 1, 3.5 and 5.5 MHz).

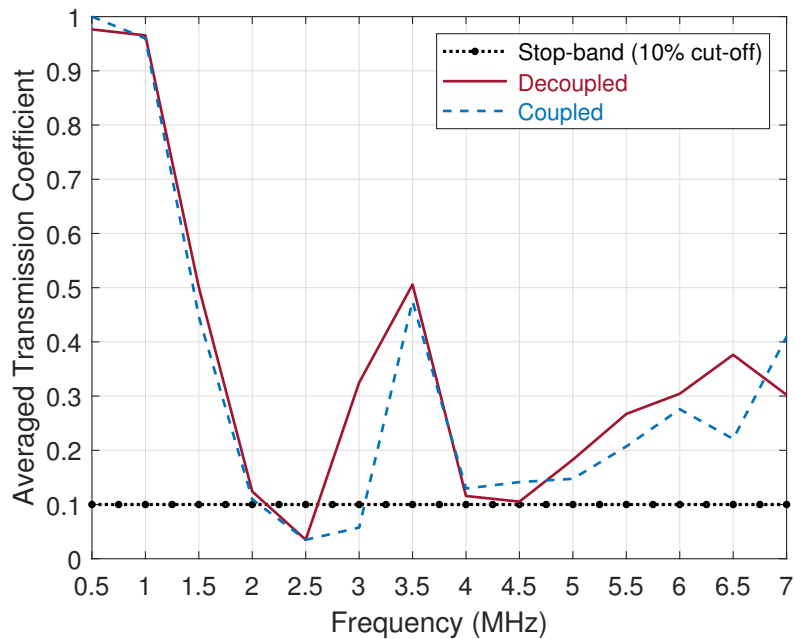
Furthermore, an averaged transmission coefficient  $\bar{T}$  has been determined for each frequency as the mean of the ten  $T_i$ , recorded in the ten receiver points to visualise and compare results more quantitatively as shown in Figure 4.5. It must be noted that these average values  $\bar{T}$  represent the change in the trend of transmission coefficients along the frequency range, and it should not be used as the only result to assess the propagation of the wave in the test material. However, since transmission coefficients  $T_i$  at the stop-band frequencies are very similar, the averaged value can represent the wave propagation and

transmission coefficients on the recording line.



**Figure 4.4:** Transmission coefficients on the recording points for a periodic structure. Decoupled (left) and coupled (right). ( $V_f = 30\%$ )

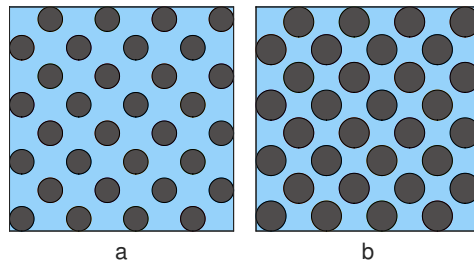
As seen in the averaged transmission coefficient graph [Figure 4.5](#), stop-band frequencies range of 2.1 – 2.6 MHz can be assumed for the case of pure elasticity (or decoupled with the absence of magnetic field). When the piezomagnetic coupling terms are introduced (or coupled with the presence of magnetic field), the width of the first stop-band increases to 2.1 – 3.1 MHz, presenting a slightly enlarged stop-band characteristic for the test material.



**Figure 4.5:** The average transmission coefficient  $\bar{T}$  and effect of magneto-elastic coupling on the stop-band frequencies in periodic microstructure.

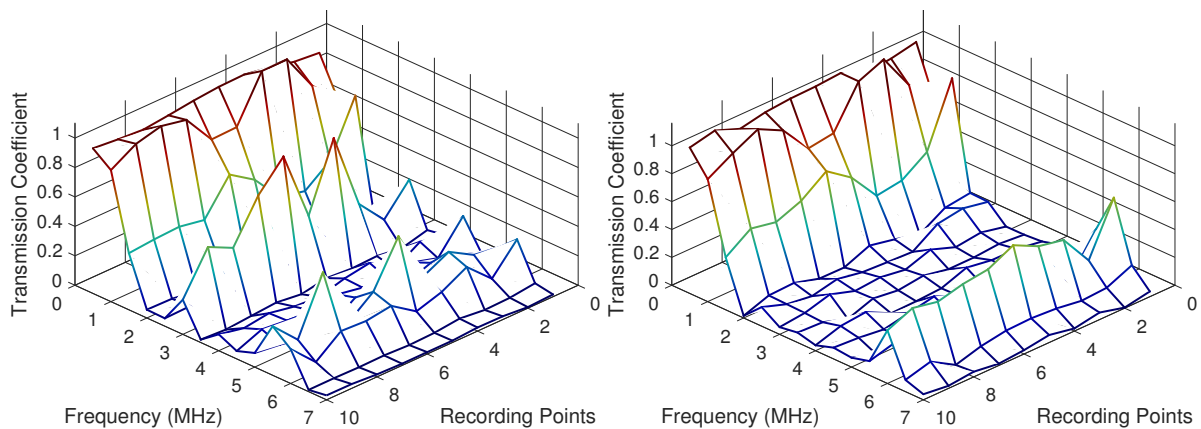
### Influence of volume fraction of inclusions

It is known that the volume fraction of the inclusions is an influential parameter on the static and dynamic behaviour of MREs [27, 89, 91, 99]. It was previously reported that a higher volume fraction of magnetic particles can lead to increased band width and transition of the stop-band frequencies. Therefore, it is worth investigating the effect of the volume fraction. To study this effect, another periodic test material has been created by increasing the volume fraction to 45% as seen in Figure 4.6.



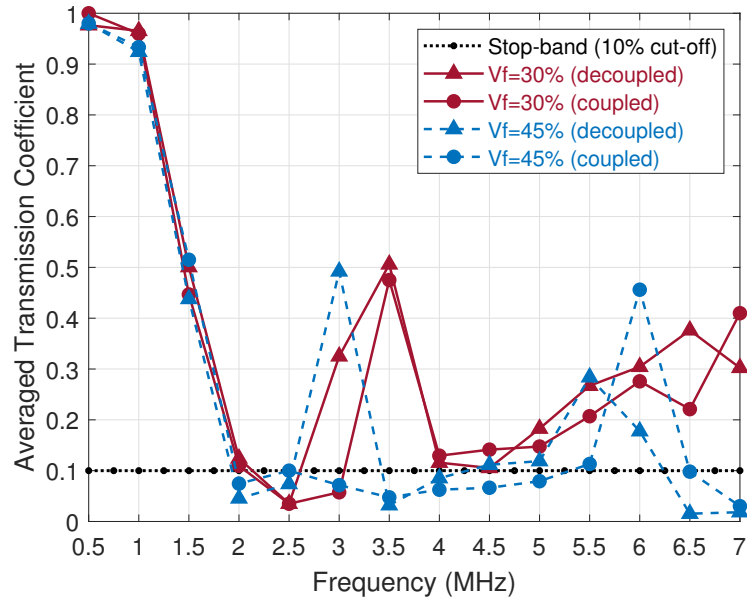
**Figure 4.6:** Increased volume fraction for periodic test material:  $V_f = 30\%$  (a),  $V_f = 45\%$  (b).

The results in Figure 4.7 show that while there is a relatively similar distribution of transmission coefficients in decoupled case compared to volume fraction of 30% (Figure 4.4(left)), the values in the middle region 2 – 5.5 MHz have significantly decreased in coupled case for increased volume fraction of inclusions (Figure 4.7(right) for 45% and Figure 4.4(right) for 30%) .



**Figure 4.7:** Transmission coefficients on the recording points for a periodic structure. Decoupled (left) and coupled (right). ( $V_f = 45\%$ )

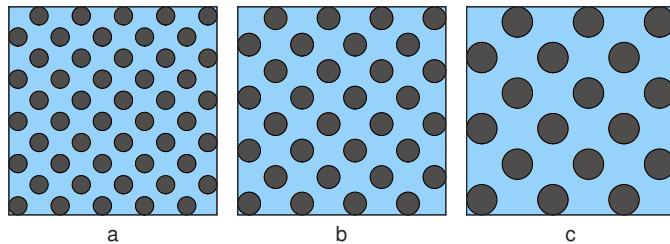
Further, Figure 4.8 presents the averaged transmission coefficient results of  $V_f = 45\%$  and  $V_f = 30\%$  together for comparison. An increase in volume fraction affects the wave propagation characteristics noticeably. Increasing the particle volume fraction moves the frequency ranges  $3.5 - 4.0$  MHz and  $6.5 - 7.0$  MHz into stop bands for the decoupled physics case. For the coupled physics case, increasing the particle volume fraction leads to a considerably wider first stop band of  $2.0 - 5.5$  MHz.



**Figure 4.8:** The average transmission coefficient  $\bar{T}$  and the effect of volume fraction on the wave propagation.

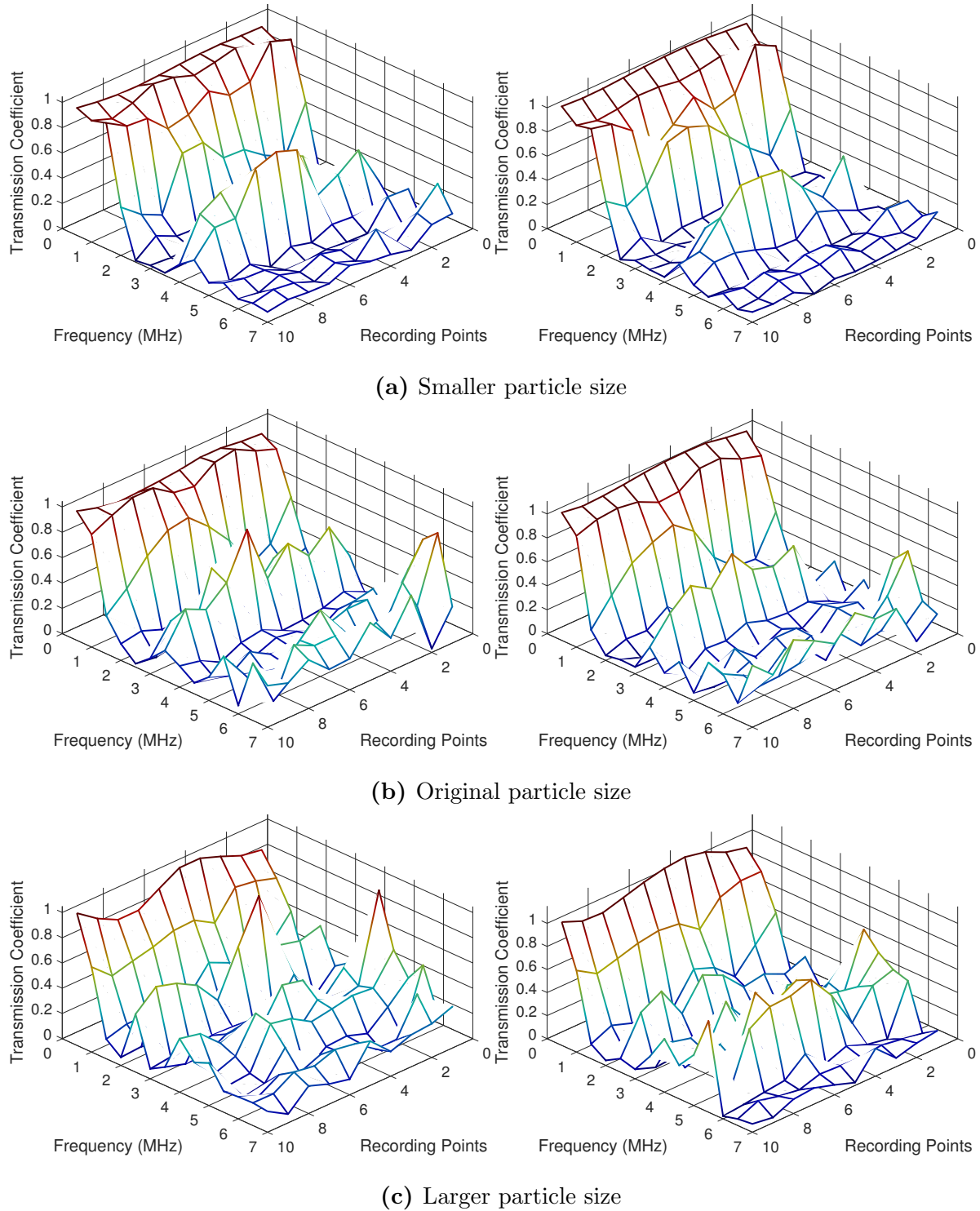
### Influence of particle sizes

The particle size for a given volume fraction is another geometric parameter influencing the wave propagation. To study this parameter, three different (but each uniform) size configurations have been created as seen Figure 4.9. The particle size used in the original configuration have been increased and decreased by keeping the volume fraction  $V_f = 30\%$ .



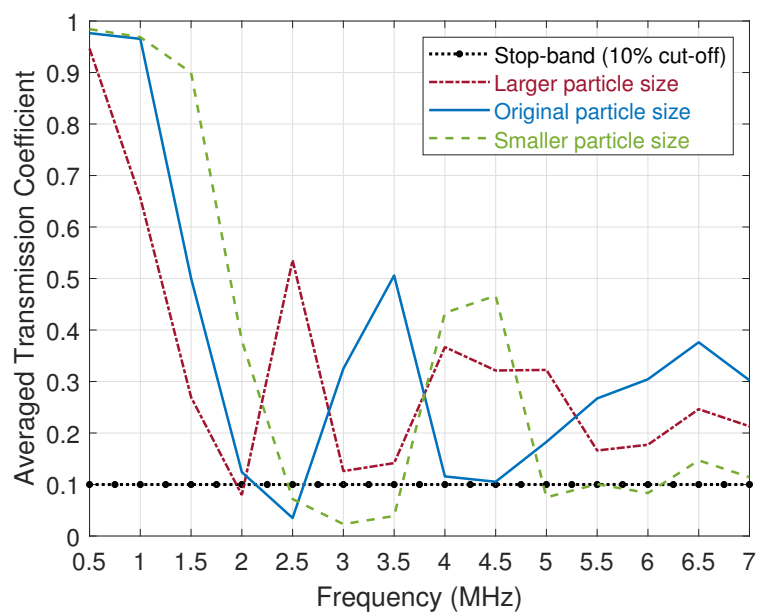
**Figure 4.9:** Different particle sizes: smaller (a), original (b), larger (c). ( $V_f = 30\%$ )

Figure 4.10 depicts that the particle size can significantly affect the stop-bands in the periodic test material. Note that changing the particle size for a fixed volume fraction in a periodic structure also means a change in the number of periodic arrays. Hence, the effect of particle sizes for a fixed volume fraction can also be considered as the effect of the numbers of periodic arrays.

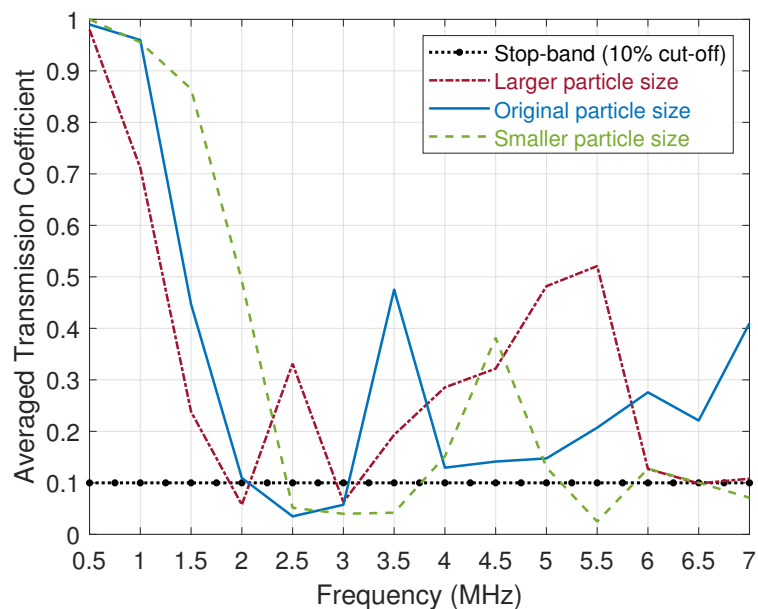


**Figure 4.10:** Transmission coefficients on the recording points for different particle sizes. Smaller (a), original (b), larger (c) particle for  $V_f = 30\%$ . Decoupled (left)/coupled (right).

The results shown in Figure 4.11 present the averaged transmission coefficient for smaller (dashed), original (solid) and larger (dash-dotted) particle size configurations. It can be seen that with decreasing particles sizes, the first stop-band frequency moves to higher values and the first stop-band widens for both coupled and decoupled cases. It is also useful to note, that coupled cases for each size configuration present increased first stop-band widths compared to their decoupled counterparts.



(a) Decoupled



(b) Coupled

**Figure 4.11:** The average transmission coefficient  $\bar{T}$  and the effect of particle size on the wave propagation in coupled/decoupled cases. Decoupled (top), coupled (bottom).

Here, it must be noted that there are two aspects of changing the particle diameter as

studied under the titles "influence of volume fractions" and "influence of particle size". These are:

- The effect of particle sizes for a fixed numbers of periodic arrays that can also be considered as the effect of the volume fraction. (which is the case in [Figure 4.6](#))
- The effect of the numbers of periodic arrays for a fixed volume fraction that can also be considered as the effect of particle sizes. (which is the case in [Figure 4.9](#))

#### 4.4.2 Random microstructure

Next, random microstructural configurations have been considered to study the effects of magneto-elastic coupling, and material's microstructure in more details and expand the analysis to the class of materials with random microstructure. Geometrical randomness has been introduced in terms of particle size only, particle position only, and both (see [Figure 4.3](#)). A volume fraction of inclusions of 30% has been assumed for all random microstructures.

##### Size or position randomness only

Initially, randomness in particle size or position has been considered separately as seen in [Figure 4.12](#). To investigate particle size randomness, a uniform particle diameter distribution of 110–240  $\mu\text{m}$  is assumed to create random sizes for particles in a periodic pattern ([Figure 4.12a](#)). For the next test, identical particles with random positions have been used for position randomness by using a MATLAB code developed in-house ([Figure 4.12b](#)). In this code, number of particles has been fixed, and the size or position of the particles have been set to be variable with some limitations to create the randomness.

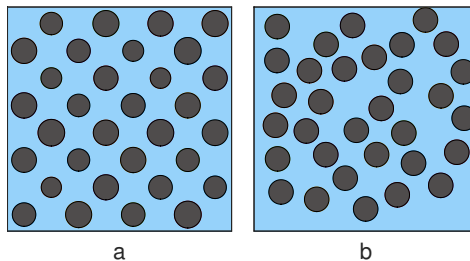


**Figure 4.12:** Randomness added to particles sizes (a) or particles positions (b). ( $V_f = 30\%$ )

The distributions of transmission coefficients in [Figure 4.13](#) and [Figure 4.14](#) indicate that randomness in particles sizes or positions can reduce the transmission coefficients in the second pass region compared to periodic microstructure ([Figure 4.4](#)). Note that the reduced wave propagation in the second pass region can be considered good or bad depending on the purpose. For instance, it can be considered as a desirable property for an absorbing purpose, while it can be undesirable for a filtering purpose that requires a distinct range of reduced (stopped) waves and then a pass region.

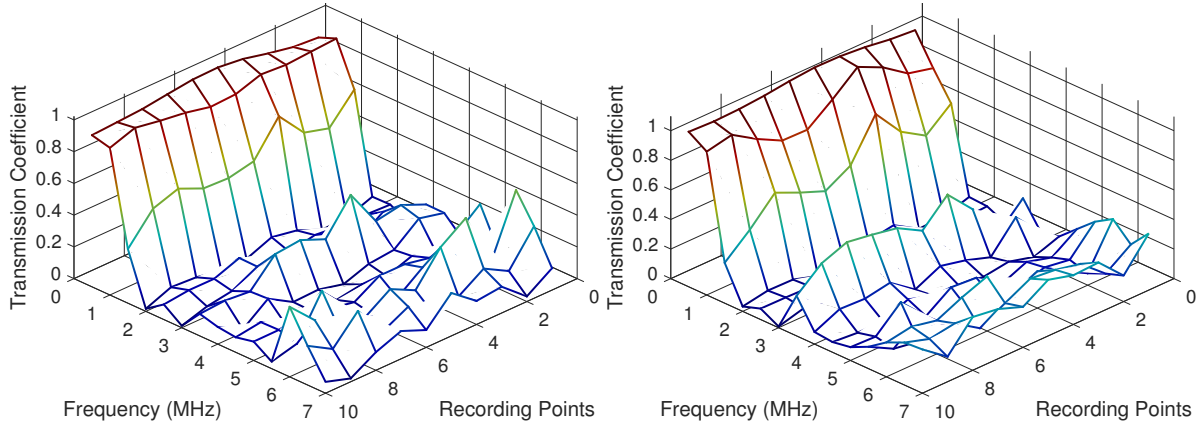


**Figure 4.13:** Transmission coefficients on the recording points for size randomness only. Decoupled (left) and coupled (right).

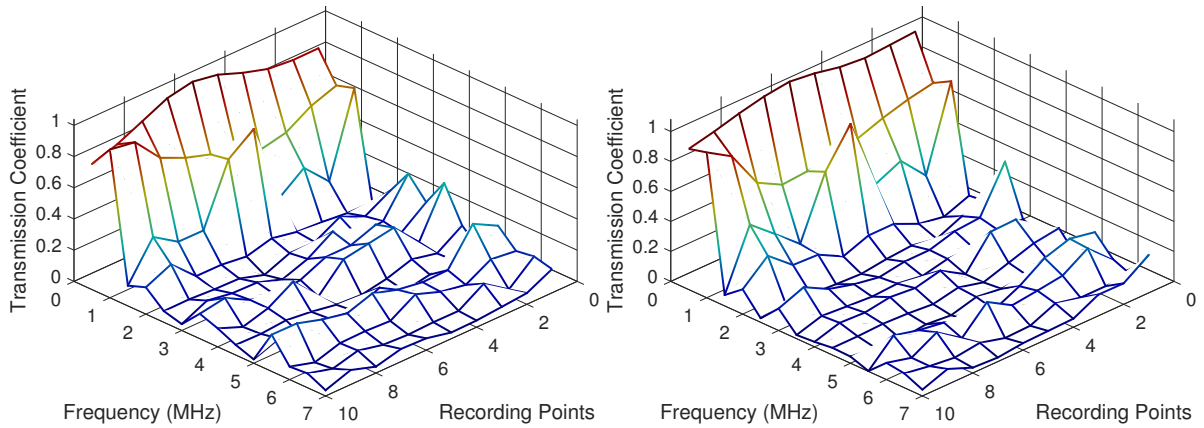
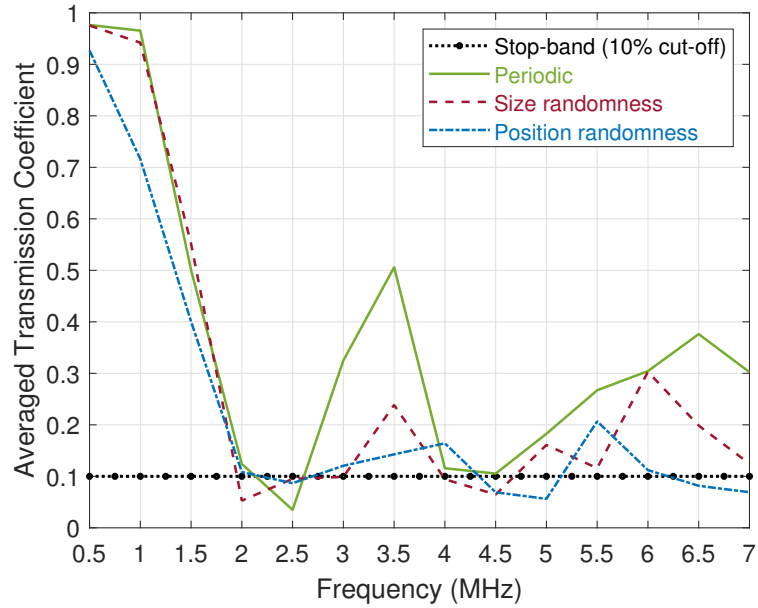


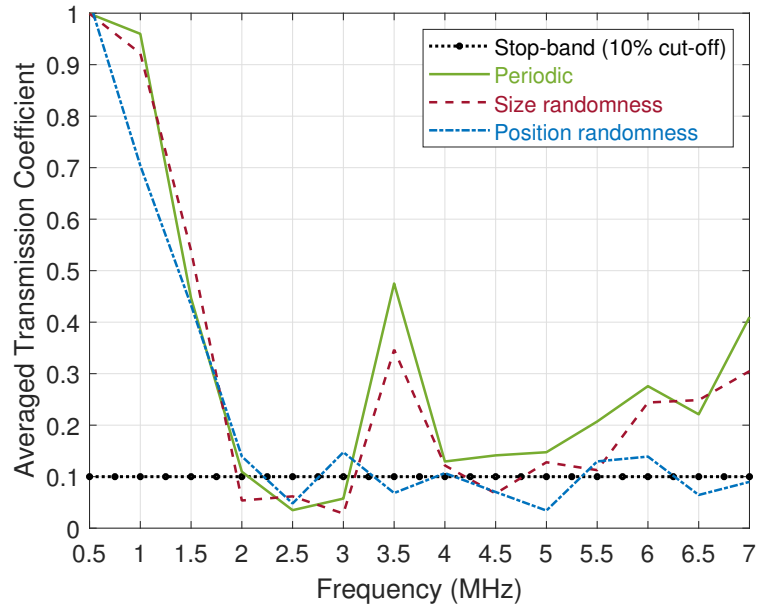
**Figure 4.14:** Transmission coefficients on the recording points for position randomness only. Decoupled (left) and coupled (right)

The average transmission coefficients of these configurations in [Figure 4.15](#) show that randomness added to particles sizes leads to a similar first stop-band range (2 – 3 MHz) for the coupled physics case and a slightly increased first stop-band width for the decoupled physics case. However, randomness added to particles positions has a much more

significant influence on the results by removing almost all the second pass-band frequencies and turning them into a stop-band in both coupled and decoupled cases. It can also be noted that randomness in positions leads to more dispersive wave propagation in the test material, and thus transmission coefficients in pass-band frequencies are generally significantly lower compared to the periodic benchmark case while randomness in particle size still maintains a level of geometric periodicity and, thus, it still provides distinct stop and pass-band regions.



(a) Decoupled



(b) Coupled

**Figure 4.15:** The average transmission coefficient  $\bar{T}$  and the effect of randomness in size, position and periodic on the wave propagation. Decoupled (top)/Coupled (bottom).

### Size and position randomness simultaneously

As the final analysis, randomness has been introduced to both particle size and position simultaneously. Three different *fully* random test material realisations have been created as seen in [Figure 4.16](#).

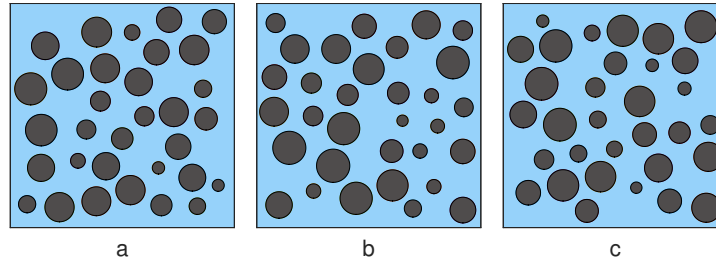
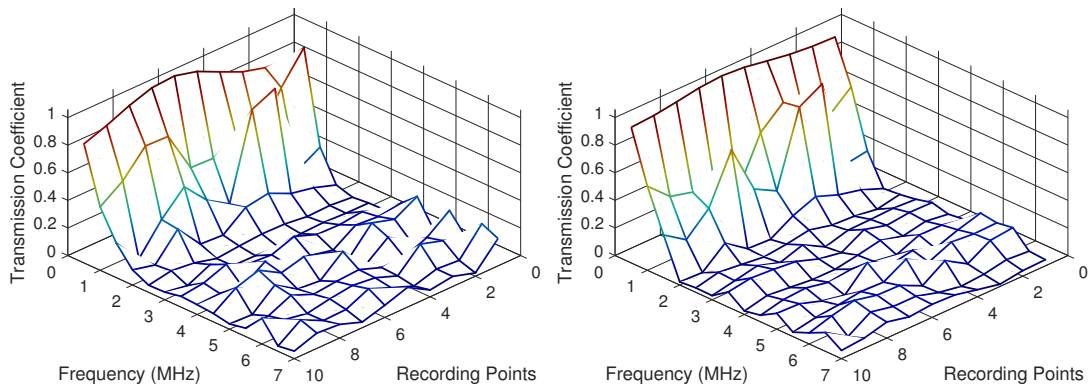


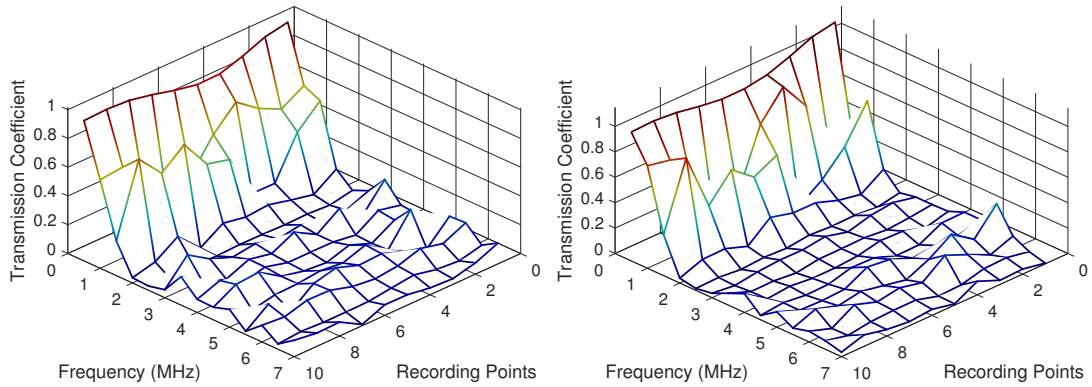
**Figure 4.16:** Randomness added to particles sizes and positions simultaneously. Three different realisations a, b and c from left to right. ( $V_f = 30\%$ )

It can be seen that the full randomness can lead to a higher dispersion of the wave and it can dramatically affect the stop-band behaviour for the material as given in 3D plots of the transmission coefficients  $T_i$  (see [Figure 4.17](#)). Moreover, [Figure 4.18](#) presents the distributions of the average transmission coefficients of random realisations, and shows the difference with the periodic test material. As seen, all three random realisations present very similar behaviour by removing the second pass-band compared to periodic arrangement. Furthermore, note that the difference between the coupled and decoupled cases has become negligible in a fully random test materials (see [Figure 4.18](#)).

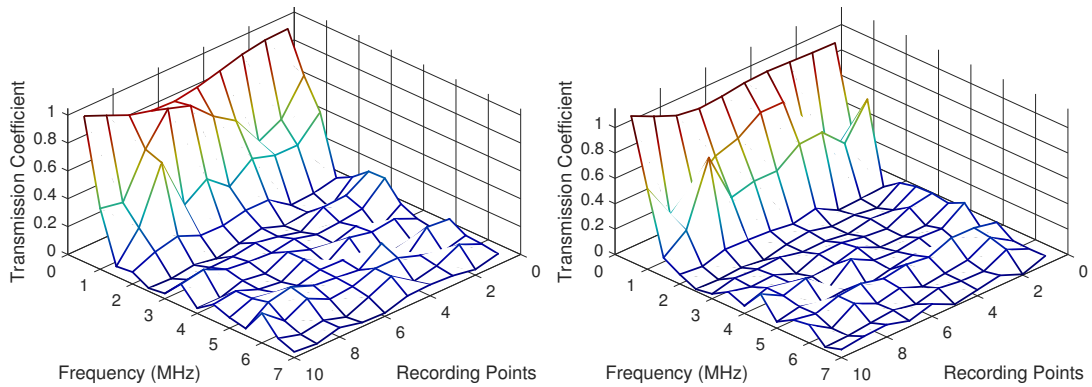
Note that the results of random test materials in [Figure 4.18](#) present similar wave propagation characteristics compared to the case of the randomness added to the position only (see [Figure 4.15](#)). However, the transmission coefficients in the second pass-band have been reduced slightly more than the position randomness, and the second pass-band has been turned into stopped frequencies.



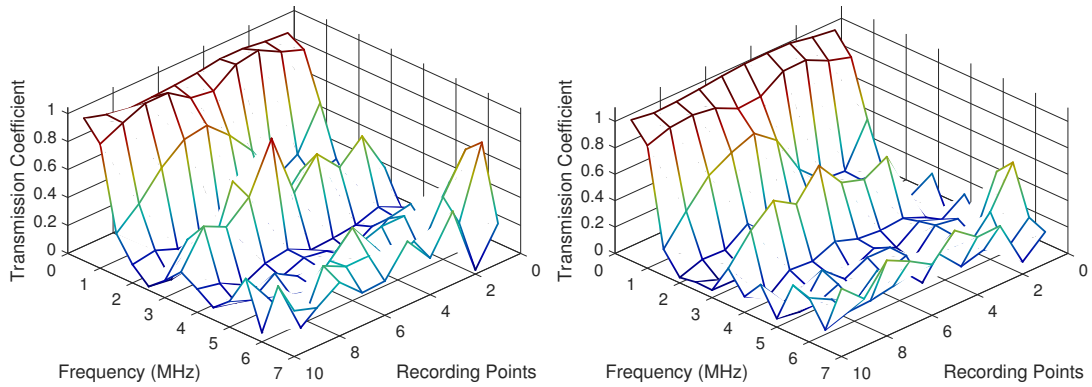
(a) Realisation-a



(b) Realisation-b

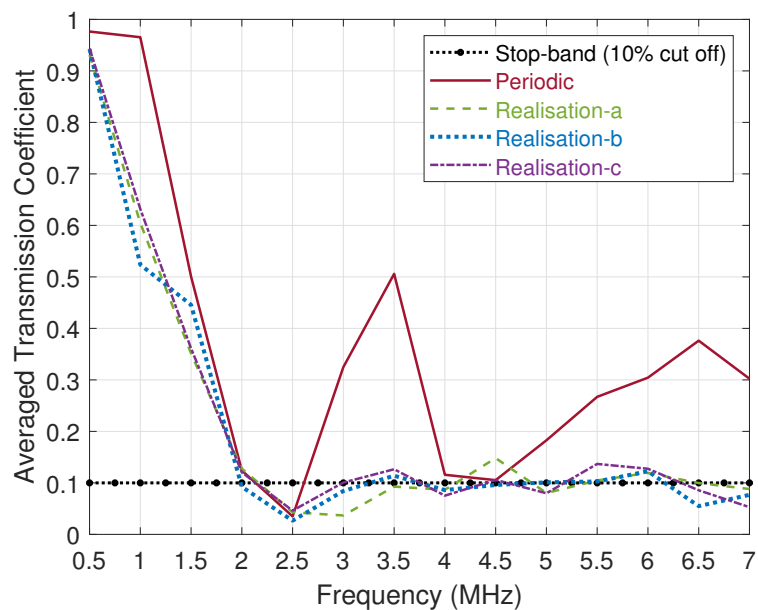


(c) Realisation-c

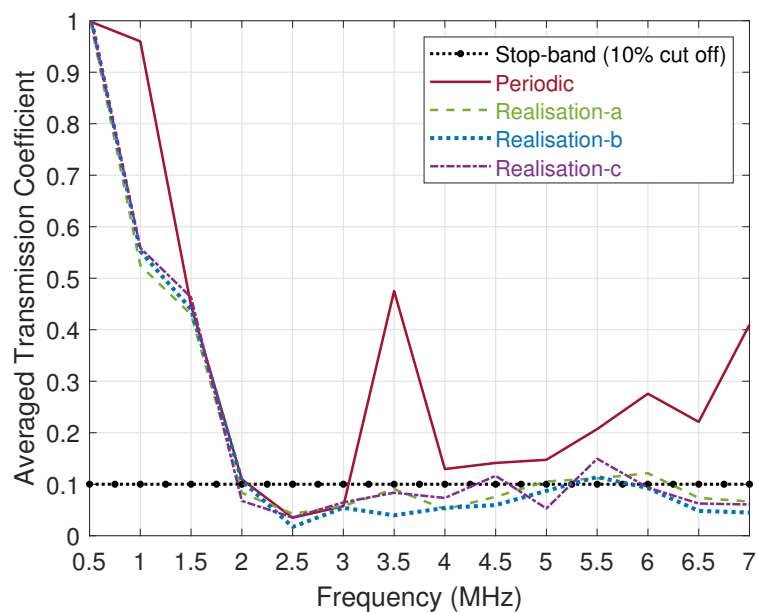


(d) Periodic structure

**Figure 4.17:** Transmission coefficients  $T_i$  in periodic and fully random test materials. Decoupled (left) and coupled (right).



(a) Decoupled



(b) Coupled

**Figure 4.18:** The average transmission coefficient  $\bar{T}$  in case of fully random material realisations and periodic material. Periodic, realisation-a, realisation-b, realisation-c. Decoupled (left)/Coupled (right).

## 4.5 Discussion

In this chapter, the effects of magneto-elastic coupling and variations in geometry of microstructures on the longitudinal wave propagation and stop-bands have been studied for a magnetorheological elastomer. Longitudinal sine waves have been created during the simulation time in the source region and these waves have been recorded in the receiver region after having propagated through the test material.

In a material with a periodic structure, it was seen that the particle size and volume fraction are important parameters in the stop-band frequencies. Furthermore, a distinct difference in the first band gap has been observed between coupled and decoupled considerations for these tests. When magneto-elastic coupling was introduced to the system, test geometries exhibited a wider band gap. For the same volume fraction, decreasing the particle size has resulted in a wider first stop-band gap and a shift of the first stop-band frequency to a higher frequency value. As has been stated, this configuration can also be considered as the effect of increased number of periodic arrays in the microstructure. The results for different particle size case have been attributed to more dispersive behaviour of the longitudinal wave due to those increased number of arrays. Moreover, the volume fraction of inclusions also has a notable effect on the characteristics: it was observed that pass-band frequencies can be transferred into the stop-band in case of higher volume fractions. The difference between coupled and decoupled formulations has also been significantly increased for higher volume fractions resulting in a possible second stop-band.

Next, materials with geometrically random microstructure have been analysed. It was observed that randomness added to particle size reduces the transmission coefficient in the second pass range although the first band gap remained similar to that of periodic materials. However, introduction of randomness to particle position leads to the complete removal of the pass-band ranges in both coupled and decoupled cases. Lastly, fully random test materials with randomness added to both sizes and positions have been investigated. Full randomness exhibited stop-band characteristics similar to those of randomness added to position only. It was observed that the pass-band ranges tend to be removed in case of full randomness similar to positions randomness. Therefore, it can be concluded that particle position randomness is much more significant than particle size randomness in wave propagation behaviour. Interestingly, the effects of magneto-elastic coupling compared to decoupled counterparts have been lost in the fully random structures, concluding that geometrical randomness, specifically positions randomness, is the most dominant parameter

characterising wave propagation and controlling stop/pass band behaviour.

# Chapter 5

## Conclusions

The main aim of this thesis was to provide numerical models to predict and investigate the behaviour of a responsive composite material, which can exhibit magneto-elastic coupling phenomenon, in a static and dynamic problem.

Responsive composite materials have been an active field of research in the last few decades. Magnetorheological elastomers (MREs) are examples of such responsive composites (also referred to as smart composite materials), and they consist of magnetic inclusions embedded in an elastomer. MREs are heterogeneous materials, and they show a coupling between magnetism and elasticity. This coupling behaviour is originated from a phenomenon called magnetostriction that occurs in magnetic component of the composite under an external magnetic field. As a result, this feature proposes various feasible and worthwhile applications in many engineering fields.

In the analysis of heterogeneous materials, the underlying microstructure needs to be taken into account in order to describe and predict the behaviour of a macroscopic continuum accurately. Several approaches can be used to describe the behaviour of a heterogeneous material by also considering the microstructural information. For instance, macroscopic modelling approaches introduce the micro-level effects to the model via phenomenological material parameters. A detailed and explicit material description of the constituents is followed in microscopic approaches. However, it may not be possible to measure or define the additional material parameter in macroscopic approaches, and computational cost/CPU time can significantly increase in microscopic approaches. Alternatively, a combined approach called multi-scale analysis considering various scales of observation simultaneously can be used to capture the micro-level influences and avoid potential disadvantages of those mono-scale methods. In the first part of this study, a

multi-scale approach was followed for an MRE model to introduce the microstructural information in a coupled physics framework.

This multi-scale approach describes the composite as a homogeneous material on the macro-scale and heterogeneous on the micro-scale. A non-local analytical homogenisation scheme was used to establish the proposed multi-scale model. In this method, the concept of representative volume element (RVE) was used to denote the micro-scale (or microstructural unit cell) as typically employed by multi-scale approaches. Thus, the size of the RVE have become a model parameter. On the other hand, non-local homogenisation scheme results in the appearance of additional material parameters: length-scale that can be expressed in terms of RVE size on the macro-level. These points have motivated the definition and determination of the RVE size in magneto-elastic coupling framework for an MRE material, and derivation of constitutive relations of macroscopic magneto-elastic continua with additional model parameter RVE size. Consequently, the microstructural information in an MRE can be taken into account via the RVE size in a static problem on the macro-scale.

To this end, an RVE size determination process has been addressed first in this thesis. A numerically-statistical analysis based on the coefficient of variation and finite element method have been used to determine lower bounds of the RVE size for an MRE material. In magneto-elastic coupling framework, four individual RVE sizes have been defined for different phenomena: purely elastic ( $L_1$ ), purely magnetic ( $L_4$ ), and coupling ( $L_2, L_3$ ) behaviour in the material. The results show that it is possible to determine a lower bound of the RVE sizes for an MRE sample by following the proposed numerically-statistical analysis. Furthermore, a parametric study has been conducted to examine the sensitivity of the RVE sizes to different material properties of the constituents, and following conclusions can be deduced:

- The numerically-statistical analysis results in different RVE sizes for each defined phenomenon, and the RVE size is primarily set by the contrast of the different material properties, i.e. the stiffness, permeability or magneto-elastic coupling. Moreover, negligible difference was observed between the coupling RVE sizes  $L_2$  and  $L_3$  in accordance with thermodynamic consistency.
- The formalistic approach showed that the contrast in material properties of the constituents (more heterogeneity in material properties) leads to larger sizes of the associated RVE. For instance, increased stiffness contrast results in larger purely

---

elastic RVE size ( $L_1$ ) while not showing an influence on the other RVE sizes. In the same way, an increase in coupling and permeability contrast presents the larger RVE sizes only for coupling ( $L_2, L_3$ ) and permeability ( $L_4$ ) respectively.

- Furthermore, while there is a converging trend for purely elastic and purely magnetic RVEs, coupling RVEs show a non-convergent trend in the range of assumed larger contrast values. Note that the difference between convergent and non-convergent trends occurs for extremely large contrast. Additionally, it was found that the determined coupling RVE sizes ( $L_2, L_3$ ) also covers the lower bound condition of the purely elastic and magnetic RVE sizes ( $L_1, L_4$ ). With these elaborations, it was concluded that same RVE size can be assumed for all ( $L_1, L_2, L_3$ , and  $L_4$ ) for practical purposes.

Once the definition and determination of the RVE size study has been addressed, a non-local analytical homogenisation scheme has been followed to derive a generalised magneto-elastic continuum model to complete the static aspect of this thesis. A piezomagnetic continuum model has been developed with gradients of strain, piezomagnetic coupling and magnetic field whereby the characteristic length-scale parameters are expressed in terms of RVE sizes. With this gradient enriched piezomagnetic model, a singularity removal study in mechanical and magnetic fields has been conducted to compare the results from those obtained via classical piezomagnetic model. Difference between aforementioned RVE sizes has been analysed and the largest determined RVE size was used as suggested in the gradient enriched governing equations to introduce the information from the underlying micro-level. A solution scheme has been employed and implemented based on the finite element method and extended Ru-Aifantis theorem. The results showed that:

- In case of using the determined RVE size in the gradient model, the singularities can be removed in mechanical strains and magnetic fields on the tip of a notch for a homogenised MRE plate on the macro-scale. However, the classical model has predicted spiky values (singularities) at the notch tip in the same problem. Thus, the improvement in accurately predicting the magneto-elastic material behaviour, and the significance of microstructural effects on the macro-level modelling has been demonstrated.

The behaviour of the magneto-elastic composites in dynamic problems is another major area of interest within the field. In particular, phononic crystals (PCs) consisting of a periodic arrangement of inclusions in a matrix material, have garnered a great deal of interest owing to a phenomenon known as band gap frequencies in which particular frequency ranges are not able to propagate through the PCs. The motivation of the dynamic aspect of this work was to study the effects of magneto-elastic coupling and other parameters such as randomness in geometrical properties, volume fraction and size of inclusions on longitudinal wave propagation and, in particular, on the appearance of stop-band frequencies for MRE materials. Longitudinal wave propagation through 2D MRE test material has been studied by using finite element method and the constant average acceleration variant of the Newmark integration scheme. In the numerical tests, magneto-elastic coupling has been introduced to test material by assuming zero or non-zero piezomagnetic coupling coefficients and magnetic permeability of the air or material to model the decoupled or coupled physics, respectively. Further, the influence of geometrical randomness has been analysed in different levels: randomness in particle size only, particle position only and both simultaneously. The results indicate that:

- The most important parameters deciding whether a frequency is in a stop-band or a pass-band were the randomness in geometrical properties and piezomagnetic coupling. For a periodic microstructure, it was observed that piezomagnetic coupling can lead to a wider first stop-band range compared to a elastic decoupled counterpart. Next, while randomness in particle size leads to a stop-band range and reduced wave transmission in the second pass region, randomness in particle position leads to removal of the pass band ranges compared to periodic structures. Lastly, full randomness exhibited similar stop-band characteristics to those from the position randomness by transferring the second pass range into the stop-bands. Therefore, it was concluded that randomness in particle position is more influential and significant than the randomness in particle size in wave propagation and controlling the stop/pass band behaviour. Additionally, the influence of piezomagnetic coupling becomes insignificant in fully random structures.
- Moreover, the influence of size and volume fraction of the inclusions in a periodic structure have also been investigated. It was seen that volume fraction of inclusions has also a notable influence on characteristics. In case of higher volume fraction, pass-band frequencies can be transferred into stop-band ranges for both coupled and

---

decoupled formulations. Further, the difference between the coupled and decoupled considerations has been increased for higher volume fractions. Finally, decreasing the particle size for the same volume fraction in the periodic test material leads to a widening of the first stop-band range and a transition of the first band gap frequency to a higher value.

# Chapter 6

## Future works

In this thesis, contributions have been made on the RVE size determination in a magneto-elastic composite, a multi-scale model incorporating determined RVE size to analyse the behaviour of the composite accurately, and longitudinal wave propagation analysis with influential parameters from band gap aspect. However, some adaptations, numerical tests and possible experimental work have been left aside for the future.

Firstly, randomly distributed Terfenol-D particles have been assumed in RVE size determination chapter in this work, however, Terfenol-D grains can have irregular shapes instead of being perfectly circular. Further, the orientation of the particles can also be random in a mechanically mixed MRE sample. Therefore, numerical tests can be conducted by also considering the shape and orientation randomness in RVE size determination process to investigate the potential differences and effects of these parameters.

Secondly, the static and dynamic aspect have been studied in 2D framework in this study. Another future work has been set to extend the finite element implementation of these chapters to 3D analysis. For this purpose, 3D cubic RVEs can be created and proposed size determination process can be followed to address the lower bound of the RVEs in 3D context. Additionally, the gradient enriched formulation can also be extended for a similar problem to study its efficiency in a 3D example. Further, the propagation of a longitudinal wave in 3D MRE bodies can be modelled to study stop-band frequencies. It is believed that extension of the models to 3D can be used for a future study that investigates the direct validation and comparison of the numerical modelling with an identical experimental sample.

As stated, the modelling approach in this study is based on linear piezomagnetic behaviour that is suitable for small strains, and time dependent response of these naturally

---

viscoelastic materials (MREs) has not been considered. These limitations are other points that can be improved in the future studies. By following the viscoelastic (time dependent) modelling approaches as summarised in the first chapter, it is worth to investigate the RVE size determination for MREs exhibiting large strains. In addition, developing a viscoelastic gradient model can also be a future research aim to capture the influence of microstructure and the real nature of MREs in their macroscopic behaviour.

Moreover, the gradient enriched magneto-elastic model and determined RVE sizes have been used in singularity removing application. Besides, size-dependent mechanical and magnetic response of a model can also be addressed to study the effectiveness of RVE sizes in the gradient model. Furthermore, an experimental work can be presented to compare the results from two numerical analysis: with or without RVE sizes in the gradient formulation to observe the accuracy of the numerical model with the real response of an MRE sample.

Finally, it is known that classical continuum theories are not capable of describing the wave dispersion. However, a gradient enriched dynamic piezomagnetic model has been presented by researches, and this model was able to predict the dispersive wave propagation in a magneto-elastic model. The main parameter controlling the dispersive properties was expressed as the ratio of the length- and time-scale parameter. Specifically, time-scale parameter must be larger than length-scale. Similar to length-scale, time-scale parameter can also be associated to a namely dynamic RVE size. At this point, a definition and determination of an RVE in case of dynamic loading can be studied in the future. If a *dynamic RVE* can also be determined, a validation can be made with these already presented dynamic piezomagnetic models.

# Appendix A

## Weak form derivation on micro-scale

The governing equations on the micro-level:

$$\mathbf{L}_u^T \mathbf{C}^m \mathbf{L}_u \mathbf{u}^m + \mathbf{L}_u^T \mathbf{q}^m \mathbf{L}_\varphi \varphi^m = \mathbf{0} \quad (\text{A.1a})$$

$$\mathbf{L}_\varphi^T \mathbf{q}^{mT} \mathbf{L}_u \mathbf{u}^m - \mathbf{L}_\varphi^T \boldsymbol{\mu}^m \mathbf{L}_\varphi \varphi^m = 0 \quad (\text{A.1b})$$

The weak form of Eq. (A.1) with domain  $\Omega$  and boundary  $\Gamma$  can be found by using test functions  $\mathbf{w}_u$ ,  $w_\varphi$  and integration by parts,

$$\mathbf{w}_u = \begin{Bmatrix} w_{ux} \\ w_{uy} \\ w_{uz} \end{Bmatrix}, \quad w_\varphi, \quad \text{and} \quad \int_{\Omega} uv' d\Omega = \int_{\Omega} (uv)' - \int_{\Omega} u'vd\Omega \quad (\text{A.2})$$

Firstly, Eq. (A.1a) can be multiplied by test function  $\mathbf{w}_u$  and integrated as follow:

$$\overbrace{\int_{\Omega} \underbrace{\mathbf{w}_u^T}_{\mathbf{u}} \underbrace{\mathbf{L}_u^T \mathbf{C}^m \mathbf{L}_u \mathbf{u}^m}_{\mathbf{v}'}}_{\textcircled{1}} d\Omega + \overbrace{\int_{\Omega} \underbrace{\mathbf{w}_u^T}_{\mathbf{u}} \underbrace{\mathbf{L}_u^T \mathbf{q}^m \mathbf{L}_\varphi \varphi^m}_{\mathbf{v}'}}_{\textcircled{2}} d\Omega = \mathbf{0} \quad (\text{A.3a})$$

$$\textcircled{1} \rightarrow \int_{\Omega} \mathbf{L}_u^T (\mathbf{w}_u^T \mathbf{C}^m \mathbf{L}_u \mathbf{u}^m) d\Omega - \int_{\Omega} (\mathbf{L}_u^T \mathbf{w}_u^T) \mathbf{C}^m \mathbf{L}_u \mathbf{u}^m d\Omega \quad (\text{A.3b})$$

$$\textcircled{2} \rightarrow \int_{\Omega} \mathbf{L}_u^T (\mathbf{w}_u^T \mathbf{q}^m \mathbf{L}_\varphi \varphi^m) d\Omega - \int_{\Omega} (\mathbf{L}_u^T \mathbf{w}_u^T) \mathbf{q}^m \mathbf{L}_\varphi \varphi^m d\Omega \quad (\text{A.3c})$$

$$\textcircled{1} + \textcircled{2} = \mathbf{0} \quad (\text{A.3d})$$

By considering Divergence theorem for the first integrals in  $\textcircled{1}$  and  $\textcircled{2}$ , the weak form of Eq. (A.1a) can be obtained as

$$\Rightarrow \int_{\Omega} (\mathbf{L}_u \mathbf{w}_u)^T \mathbf{C}^m \mathbf{L}_u \mathbf{u}^m d\Omega + \int_{\Omega} (\mathbf{L}_u \mathbf{w}_u)^T \mathbf{q}^m \mathbf{L}_\varphi \varphi^m d\Omega = \int_{\Gamma} \mathbf{w}_u^T \mathbf{t} d\Gamma \quad (\text{A.4})$$

where

$$\int_{\Gamma} \mathbf{w}_u^T \mathbf{t} d\Gamma = \int_{\Gamma} (\mathbf{w}_u^T \mathbf{C}^m \mathbf{L}_u \mathbf{u}^m) \hat{\mathbf{n}} d\Gamma + \int_{\Gamma} (\mathbf{w}_u^T \mathbf{q}^m \mathbf{L}_\varphi \varphi^m) \hat{\mathbf{n}} d\Gamma \quad (\text{A.5})$$

Secondly, Eq. (A.1b) can be multiplied by test function  $w_\varphi$  and integrated as follow:

$$\overbrace{\int_{\Omega} \underbrace{\mathbf{w}_\varphi^T}_{\mathbf{u}} \underbrace{\mathbf{L}_\varphi^T \mathbf{q}^{mT} \mathbf{L}_u \mathbf{u}^m}_{\mathbf{v}'} d\Omega}_{\textcircled{3}} - \overbrace{\int_{\Omega} \underbrace{\mathbf{w}_\varphi^T}_{\mathbf{u}} \underbrace{\mathbf{L}_\varphi^T \boldsymbol{\mu}^m \mathbf{L}_\varphi \varphi^m}_{\mathbf{v}'} d\Omega}_{\textcircled{4}} = 0 \quad (\text{A.6a})$$

$$\textcircled{3} \rightarrow \int_{\Omega} \mathbf{L}_\varphi^T (\mathbf{w}_\varphi^T \mathbf{q}^{mT} \mathbf{L}_u \mathbf{u}^m) d\Omega - \int_{\Omega} (\mathbf{L}_\varphi^T \mathbf{w}_\varphi^T) \mathbf{q}^{mT} \mathbf{L}_u \mathbf{u}^m d\Omega \quad (\text{A.6b})$$

$$\textcircled{4} \rightarrow - \int_{\Omega} \mathbf{L}_\varphi^T (\mathbf{w}_\varphi^T \boldsymbol{\mu}^m \mathbf{L}_\varphi \varphi^m) d\Omega + \int_{\Omega} (\mathbf{L}_\varphi^T \mathbf{w}_\varphi^T) \boldsymbol{\mu}^m \mathbf{L}_\varphi \varphi^m d\Omega \quad (\text{A.6c})$$

$$\textcircled{3} + \textcircled{4} = 0 \quad (\text{A.6d})$$

By considering Divergence theorem for the first integrals in  $\textcircled{3}$  and  $\textcircled{4}$ , the weak form of Eq. (A.1b) can be obtained as

$$\Rightarrow \int_{\Omega} (\mathbf{L}_\varphi \mathbf{w}_\varphi)^T \mathbf{q}^{mT} \mathbf{L}_u \mathbf{u}^m d\Omega - \int_{\Omega} (\mathbf{L}_\varphi \mathbf{w}_\varphi)^T \boldsymbol{\mu}^m \mathbf{L}_\varphi \varphi^m d\Omega = \int_{\Gamma} \mathbf{w}_\varphi^T \mathbf{B}_\perp d\Gamma \quad (\text{A.7})$$

where

$$\int_{\Gamma} \mathbf{w}_\varphi^T \mathbf{B}_\perp d\Gamma = \int_{\Gamma} (\mathbf{w}_\varphi^T \mathbf{q}^{mT} \mathbf{L}_u \mathbf{u}^m) \hat{\mathbf{n}} d\Gamma - \int_{\Gamma} (\mathbf{w}_\varphi^T \boldsymbol{\mu}^m \mathbf{L}_\varphi \varphi^m) \hat{\mathbf{n}} d\Gamma \quad (\text{A.8})$$

Thus, the weak form of governing equation Eq. (A.1) can be written as

$$\int_{\Omega} (\mathbf{L}_u \mathbf{w}_u)^T \mathbf{C}^m \mathbf{L}_u \mathbf{u}^m d\Omega + \int_{\Omega} (\mathbf{L}_u \mathbf{w}_u)^T \mathbf{q}^m \mathbf{L}_\varphi \varphi^m d\Omega = \int_{\Gamma} \mathbf{w}_u^T \mathbf{t} d\Gamma \quad (\text{A.9a})$$

$$\int_{\Omega} (\mathbf{L}_\varphi \mathbf{w}_\varphi)^T \mathbf{q}^{mT} \mathbf{L}_u \mathbf{u}^m d\Omega - \int_{\Omega} (\mathbf{L}_\varphi \mathbf{w}_\varphi)^T \boldsymbol{\mu}^m \mathbf{L}_\varphi \varphi^m d\Omega = \int_{\Gamma} \mathbf{w}_\varphi^T \mathbf{B}_\perp d\Gamma \quad (\text{A.9b})$$

# Appendix B

## Integrations of non-local homogenisation

Linearisation of spatially dependent stiffness, strain, coupling, permeability and magnetic field can be expressed around the values at the centre of the RVEs as follow

$$C_{ijkl}^m = C_{ijkl}^M + C_{ijkl,o}^M \delta x_o \quad (\text{B.1a})$$

$$\varepsilon_{kl}^m = \varepsilon_{kl}^M + \varepsilon_{kl,p}^M \delta x_p \quad (\text{B.1b})$$

$$q_{kij}^m = q_{kij}^M + q_{kij,o}^M \delta x_o \quad (o, p = 1, 2 \text{ or } 3) \quad (\text{B.1c})$$

$$H_k^m = H_k^M + H_{k,p}^M \delta x_p \quad (\text{B.1d})$$

$$\mu_{ik}^m = \mu_{ik}^M + \mu_{ik,o}^M \delta x_o \quad (\text{B.1e})$$

**Note:** In open form, this yields:  $X^m = X^M + X_{,1}^M \delta x_1 + X_{,2}^M \delta x_2 + X_{,3}^M \delta x_3$  where  $X$  is stiffness, strain, piezomagnetic coupling, magnetic permeability or magnetic field.

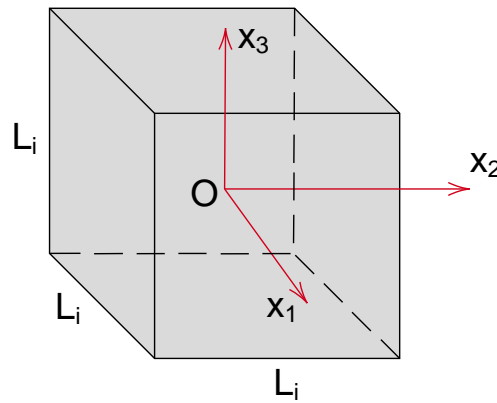


**Figure B.1:** Representative Volume Element

In non-local homogenisation, the constitutive relation for the macroscopic stress and magnetic induction can be given as

$$\sigma_{ij}^M = \frac{1}{V_{RVE}} \int_{V_{RVE}} \sigma_{ij}^m dV = \frac{1}{V_{RVE_1}} \int_{V_{RVE_1}} C_{ijkl}^m \varepsilon_{kl}^m dV - \frac{1}{V_{RVE_2}} \int_{V_{RVE_2}} q_{kij}^m H_k^m dV \quad (\text{B.2a})$$

$$B_i^M = \frac{1}{V_{RVE}} \int_{V_{RVE}} B_i^m dV = \frac{1}{V_{RVE_3}} \int_{V_{RVE_3}} q_{ikl}^m \varepsilon_{kl}^m dV + \frac{1}{V_{RVE_4}} \int_{V_{RVE_4}} \mu_{ik}^m H_k^m dV \quad (\text{B.2b})$$

By combining Eq. (B.1)-(B.2)

$$\sigma_{ij}^M = \underbrace{\frac{1}{V_{RVE_1}} \int_{V_{RVE_1}} (C_{ijkl}^M \varepsilon_{kl}^M + C_{ijkl}^M \varepsilon_{kl}^M \delta X_p + C_{ijkl,o}^M \varepsilon_{kl}^M \delta X_o + C_{ijkl,p}^M \varepsilon_{kl,p}^M \delta X_o \delta X_p)}_{\textcircled{1}} dV - \underbrace{\frac{1}{V_{RVE_2}} \int_{V_{RVE_2}} (q_{kij}^M H_k^M + q_{kij,o}^M H_k^M \delta X_o + q_{kij,p}^M H_k^M \delta X_p + q_{kij,o}^M H_{k,p}^M \delta X_o \delta X_p)}_{\textcircled{2}} dV \quad (\text{B.3a})$$

$$B_i^M = \underbrace{\frac{1}{V_{RVE_3}} \int_{V_{RVE_3}} (q_{fik}^M \varepsilon_{kl}^M + q_{fik,p}^M \varepsilon_{kl,p}^M \delta X_p + q_{fik,o}^M \varepsilon_{kl}^M \delta X_o + q_{fik,p}^M \varepsilon_{kl,p}^M \delta X_o \delta X_p)}_{\textcircled{3}} dV + \underbrace{\frac{1}{V_{RVE_4}} \int_{V_{RVE_4}} (\mu_{ik}^M H_k^M + \mu_{ik,p}^M H_k^M \delta X_p + \mu_{ik,o}^M H_k^M \delta X_o + \mu_{ik,p}^M H_{k,p}^M \delta X_o \delta X_p)}_{\textcircled{4}} dV \quad (\text{B.3b})$$

In Eq. (B.3), the format of the terms in  $\textcircled{1}$ ,  $\textcircled{2}$ ,  $\textcircled{3}$ , and  $\textcircled{4}$  is the same and it will be donated in the form as below to not repeat the same process for all.

$$\textcircled{1}, \textcircled{2}, \textcircled{3}, \textcircled{4} \Rightarrow \frac{1}{V_{RVE_i}} \int_{V_{RVE_i}} (X^M X^M + X^M X_p^M + X_{,o}^M X^M \delta X_o + X_{,o}^M X_{,p}^M \delta X_o \delta X_p) dV \quad (i = 1, 2, 3 \text{ or } 4) \quad (\text{B.4})$$

Thus, the integrations of the terms can be carried out as follow

$$\Rightarrow \frac{1}{V_{\text{RVE}_i}} \int_{V_{\text{RVE}_i}} \mathbf{X}^{\text{M}} \mathbf{X}^{\text{M}} dV = \frac{1}{L_i^3} \mathbf{X}^{\text{M}} \mathbf{X}^{\text{M}} \delta x_1 \delta x_2 \delta x_3 \Big|_{-\frac{L_i}{2}}^{\frac{L_i}{2}} \Big|_{-\frac{L_i}{2}}^{\frac{L_i}{2}} \Big|_{-\frac{L_i}{2}}^{\frac{L_i}{2}} = \mathbf{X}^{\text{M}} \mathbf{X}^{\text{M}} \quad (\text{constant}) \quad (\text{B.5a})$$

$$\Rightarrow \frac{1}{V_{\text{RVE}_i}} \int_{V_{\text{RVE}_i}} \mathbf{X}^{\text{M}} \mathbf{X}_{,p}^{\text{M}} \delta x_p dV = \frac{1}{L_i^3} \mathbf{X}^{\text{M}} \mathbf{X}_{,p}^{\text{M}} \frac{\delta x_p^2}{2} \delta x_m \delta x_n \Big|_{-\frac{L_i}{2}}^{\frac{L_i}{2}} \Big|_{-\frac{L_i}{2}}^{\frac{L_i}{2}} \Big|_{-\frac{L_i}{2}}^{\frac{L_i}{2}} = 0 \quad (\text{p, m, n} = 1, 2 \text{ or } 3) \quad (\text{linear}) \quad (\text{B.5b})$$

$$\Rightarrow \frac{1}{V_{\text{RVE}_i}} \int_{V_{\text{RVE}_i}} \mathbf{X}_{,o}^{\text{M}} \mathbf{X}^{\text{M}} \delta x_o dV = \frac{1}{L_i^3} \mathbf{X}_{,o}^{\text{M}} \mathbf{X}^{\text{M}} \frac{\delta x_o^2}{2} \delta x_m \delta x_n \Big|_{-\frac{L_i}{2}}^{\frac{L_i}{2}} \Big|_{-\frac{L_i}{2}}^{\frac{L_i}{2}} \Big|_{-\frac{L_i}{2}}^{\frac{L_i}{2}} = 0 \quad (\text{o, m, n} = 1, 2 \text{ or } 3) \quad (\text{linear}) \quad (\text{B.5c})$$

$$\begin{aligned} \Rightarrow \frac{1}{V_{\text{RVE}_i}} \int_{V_{\text{RVE}_i}} \underbrace{\mathbf{X}_{,o}^{\text{M}} \mathbf{X}_{,p}^{\text{M}} \delta x_o \delta x_p}_{\mathbf{u}} dV &= \frac{1}{V_{\text{RVE}_i}} \int_{V_{\text{RVE}_i}} \int_{V_{\text{RVE}_i}} (\mathbf{X}^{\text{M}} \mathbf{X}_{,p}^{\text{M}} \delta x_o \delta x_p)_{,o} dV - \frac{1}{V_{\text{RVE}_i}} \int_{V_{\text{RVE}_i}} (\mathbf{X}^{\text{M}} \mathbf{X}_{,op}^{\text{M}} \delta x_o \delta x_p + \underbrace{\mathbf{X}^{\text{M}} \mathbf{X}_{,p}^{\text{M}} \delta x_{o,o} \delta x_p + \mathbf{X}^{\text{M}} \mathbf{X}_{,p}^{\text{M}} \delta x_o \delta x_{p,o}}_{=0 \text{ (linear)}}) dV \\ &= \frac{1}{V_{\text{RVE}_i}} \underbrace{\oint_{\text{S}} (\mathbf{X}^{\text{M}} \mathbf{X}_{,p}^{\text{M}} \delta x_o \delta x_p) \mathbf{n}_o dS}_{=0 \text{ (periodic boundary conditions)}} - \frac{1}{V_{\text{RVE}_i}} \underbrace{\int_{V_{\text{RVE}_i}} (\mathbf{X}^{\text{M}} \mathbf{X}_{,op}^{\text{M}} \delta x_o \delta x_p) dV}_{\text{if } o=p, \text{ it is quadratic and } \neq 0} \\ &= -\frac{1}{L_i^3} \mathbf{X}_{,pp}^{\text{M}} \mathbf{X}^{\text{M}} \frac{\delta x_p^3}{3} \delta x_m x_n \Big|_{-\frac{L_i}{2}}^{\frac{L_i}{2}} \Big|_{-\frac{L_i}{2}}^{\frac{L_i}{2}} \Big|_{-\frac{L_i}{2}}^{\frac{L_i}{2}} = -\mathbf{X}_{,pp}^{\text{M}} \mathbf{X}^{\text{M}} \frac{1}{12} L_i^2 \quad (\text{p, m, n} = 1, 2 \text{ or } 3) \quad (\text{quadratic}) \quad (\text{B.5d}) \end{aligned}$$

With these elaborations, the piezomagnetic macroscopic constitutive equations with gradients of strain, magnetic field, and piezomagnetic coupling terms can be expressed as given in [Eq. \(3.15\)](#).

# Bibliography

- [1] J. Thévenot, H. Oliveira, O. Sandre, and S. Lecommandoux. Magnetic responsive polymer composite materials. *Chemical Society Reviews*, 42:7099–7116, 2013.
- [2] G. Filipcsei, I. Csetneki, A. Szilágyi, and M. Zrínyi. *Magnetic Field-Responsive Smart Polymer Composites*, pages 137–189. Springer Berlin Heidelberg, 2007.
- [3] B.S. Anthony Mortensen. Characterization, modeling and dynamic implementation of Terfenol-D particulate composites, 2005.
- [4] J. A. Hommema. Magnetomechanical Behavior of Terfenol-D Particulate Composites, 1999.
- [5] R. Elhajjar, C. Law, and A. Pegoretti. Magnetostrictive polymer composites: Recent advances in materials, structures and properties. *Progress in Materials Science*, 97:204 – 229, 2018.
- [6] L. Taixiang and X. Yangguang. Magnetorheological elastomers: Materials and applications. In *Smart and Functional Soft Materials*, chapter 4. IntechOpen, Rijeka, 2019.
- [7] B. D. Cullity. Fundamentals of magnetostriction. *JOM*, 23:35–41, 1971.
- [8] M. A. Moreno-Mateos, M. Hossain, P. Steinmann, and D. Garcia-Gonzalez. Hybrid magnetorheological elastomers enable versatile soft actuators. *npj Computational Materials*, 8, 2022.
- [9] N.B. Ekreem, A.G. Olabi, T. Prescott, A. Rafferty, and M.S.J. Hashmi. An overview of magnetostriction, its use and methods to measure these properties. *Journal of Materials Processing Technology*, 191:96 – 101, 2007.

- [10] C. Rodríguez, A. Barrio, I. Orue, J.L. Vilas, L.M. León, J. M. Barandiarán, and M.L. Fdez-Gubieda Ruiz. High magnetostriction polymer-bonded terfenol-d composites. *Sensors and Actuators A: Physical*, 142:538–541, 2008. The sixth European Magnetic Sensor and Actuator conference.
- [11] C. Rodríguez, M. Rodriguez, I. Orue, J.L. Vilas, J.M. Barandiarán, M.L.F. Gubieda, and L.M. Leon. New elastomer–terfenol-d magnetostrictive composites. *Sensors and Actuators A: Physical*, 149:251–254, 2009.
- [12] Z. Ran, B. Wang, Y. Li, S. Cao, and J. Yan. Mechanical-magneto coupled model of polymer-bonded magnetostrictive composites. *Functional materials*, 23:450–456, 2016.
- [13] S.H. Lim, S.R. Kim, S.Y. Kang, J.K. Park, J.T. Nam, and Derac Son. Magnetostrictive properties of polymer-bonded terfenol-d composites. *Journal of Magnetism and Magnetic Materials*, 191:113–121, 1999.
- [14] J. Kaleta, D. Lewandowski, and R. Mech. Magnetostriction of field-structural composite with terfenol-d particles. *Archives of Civil and Mechanical Engineering*, 15:897–902, 2015.
- [15] H. Böse, T. Gerlach, and J. Ehrlich. Magnetorheological elastomers — an underestimated class of soft actuator materials. *Journal of Intelligent Material Systems and Structures*, 32:1550–1564, 2021.
- [16] T. Y. Liu, T. Y. Chan, K. S. Wang, and H. M. Tsou. Influence of magnetic nanoparticle arrangement in ferrogels for tunable biomolecule diffusion. *RSC Adv.*, 5:90098–90102, 2015.
- [17] L. C. Davis. Model of magnetorheological elastomers. *Journal of Applied Physics*, 85(6):3348–3351, 1999.
- [18] J. A. Hommema. *Magnetomechanical behavior of terfenol-d particulate composites*. Master thesis, University of Illinois, 1997.
- [19] A. K Bastola, M. Paudel, L. Li, and W. Li. Recent progress of magnetorheological elastomers: a review. *Smart Materials and Structures*, 29(12):123002, nov 2020.
- [20] A. K. Bastola and M. Hossain. The shape – morphing performance of magnetoactive soft materials. *Materials & Design*, 211:110172, 2021.

- 
- [21] S.i Sun, J. Yang, H. Du, S. Zhang, T. Yan, M. Nakano, and W. Li. Development of magnetorheological elastomers-based tuned mass damper for building protection from seismic events. *Journal of Intelligent Material Systems and Structures*, 29:1777–1789, 2018.
- [22] E. Yarali, M. Baniasadi, A. Zolfagharian, M. Chavoshi, F. Arefi, M. Hossain, A. Bastola, M. Ansari, A. Foyouzat, A. Dabbagh, M. Ebrahimi, M. J. Mirzaali, and M. Bodaghi. Magneto-/ electro-responsive polymers toward manufacturing, characterization, and biomedical/ soft robotic applications. *Applied Materials Today*, 26:101306, 2022.
- [23] Y. Kim and X. Zhao. Magnetic soft materials and robots. *Chemical Reviews*, 122(5):5317–5364, 2022. PMID: 35104403.
- [24] A. K. Bastola and M. Hossain. A review on magneto-mechanical characterizations of magnetorheological elastomers. *Composites Part B: Engineering*, 200:108348, 2020.
- [25] D. S. Wood and P. J. Camp. Modeling the properties of ferrogels in uniform magnetic fields. *Phys. Rev. E*, 83:011402, Jan 2011.
- [26] A.K. Bastola, V.T. Hoang, and L. Li. A novel hybrid magnetorheological elastomer developed by 3d printing. *Materials Design*, 114:391 – 397, 2017.
- [27] R. Mech and J. Kaleta. Influence of terfenol-d powder volume fraction in epoxy matrix composites on their magnetomechanical properties. *Acta Mechanica et Automatica*, 11:233–236, 2017.
- [28] C.Y. Lo, S.W. Or, and H.L.W. Chan. Large magnetostriction in epoxy-bonded terfenol-d continuous-fiber composite with [112] crystallographic orientation. *IEEE Transactions on Magnetics*, 42:3111–3113, 2006.
- [29] T. A. Duenas and G. P. Carman. Particle distribution study for low-volume fraction magnetostrictive composites. *Journal of Applied Physics*, 90:2433–2439, 2001.
- [30] G. Altin, Ken K. Ho, C. P. Henry, and G. P. Carman. Static properties of crystallographically aligned terfenol-d polymer composites. *Journal of Applied Physics*, 101:033537, 2007.
- [31] M. R. Jolly, J. D. Carlson, and B. C. Muñoz. A model of the behaviour of magnetorheological materials. *Smart Materials and Structures*, 5(5):607, oct 1996.

- [32] M. H. Ahmad Khairi, A. Y.r Abd Fatah, U. Mazlan, S. A.and Ubaidillah, N. A. Nordin, N. I. Nik Ismail, S. B. Choi, and S. A. Abdul Aziz. Enhancement of particle alignment using silicone oil plasticizer and its effects on the field-dependent properties of magnetorheological elastomers. *International Journal of Molecular Sciences*, 20, 2019.
- [33] J. S. An, S. H. Kwon, H. J. Choi, J. H. Jung, and Y.G. Kim. Modified silane-coated carbonyl iron/natural rubber composite elastomer and its magnetorheological performance. *Composite Structures*, 160:1020–1026, 2017.
- [34] E. Burgaz and M. Goksuzoglu. Effects of magnetic particles and carbon black on structure and properties of magnetorheological elastomers. *Polymer Testing*, 81:106233, 2020.
- [35] K. A. Kalina, P.Metsch, and M. Kästner. Microscale modeling and simulation of magnetorheological elastomers at finite strains: A study on the influence of mechanical preloads. *International Journal of Solids and Structures*, 102-103:286 – 296, 2016.
- [36] J. Winger, M. Schümann, A. Kupka, and S. Odenbach. Influence of the particle size on the magnetorheological effect of magnetorheological elastomers. *Journal of Magnetism and Magnetic Materials*, 481:176–182, 2019.
- [37] A. Bellelli and A. Spaggiari. Magneto-mechanical characterization of magnetorheological elastomers. *Journal of Intelligent Material Systems and Structures*, 30:2534–2543, 2019.
- [38] W. H. Li and X. Z. Zhang. A study of the magnetorheological effect of bimodal particle based magnetorheological elastomers. *Smart Materials and Structures*, 19:035002, jan 2010.
- [39] Q. Wen, L. Shen, J. Li, S. Xuan, Z. Li, X. Fan, B. Li, and X. Gong. Temperature dependent magneto-mechanical properties of magnetorheological elastomers. *Journal of Magnetism and Magnetic Materials*, 497:165998, 2020.
- [40] D.Yu. Borin, S. Odenbach, and G.V. Stepanov. Stress induced by the striction of hybrid magnetoactive elastic composites. *Journal of Magnetism and Magnetic Materials*, 470:85 – 88, 2019.

- 
- [41] I. M. Gitman. *Representative volumes and multi-scale modelling of quasi-brittle materials*. Doctoral thesis, Technische Universiteit Delft, 2006.
- [42] I. M. Gitman, H. Askes, and E.C. Aifantis. Gradient elasticity with internal length and internal inertia based on the homogenisation of a representative volume element. *Journal of the Mechanical Behavior of Materials*, 18:1–16, 2007.
- [43] I. Gitman, H. Askes, and E. Aifantis. The representative volume size in static and dynamic micro-macro transitions. *International Journal of Fracture*, 135:L3–L9, 2005.
- [44] I. Gitman, H. Askes, and L.J. Sluys. Representative volume size as a macroscopic length scale parameter. In *Fifth international conference on fracture mechanics of concrete and concrete structures*, pages 483–491. La-FraMCos, 2004.
- [45] A. Attaran, J. Brummund, and T. Wallmersperger. Modeling and finite element simulation of the magneto-mechanical behavior of ferrogels. *Journal of Magnetism and Magnetic Materials*, 431:188 – 191, 2017.
- [46] Y. L. Raikher and O. V. Stolbov. Numerical modeling of large field-induced strains in ferroelastic bodies: a continuum approach. *Journal of Physics: Condensed Matter*, 20:204126, 2008.
- [47] E Akbari and H Khajehsaeid. A continuum magneto-mechanical model for magnetorheological elastomers. *Smart Materials and Structures*, 30:015008, 2020.
- [48] A. Dorfmann and R.W. Ogden. Magnetoelastic modelling of elastomers. *European Journal of Mechanics - A/Solids*, 22(4):497–507, 2003.
- [49] I.A. Brigadnov and A. Dorfmann. Mathematical modeling of magneto-sensitive elastomers. *International Journal of Solids and Structures*, 40(18):4659–4674, 2003.
- [50] R. Bustamante. Transversely isotropic nonlinear magneto-active elastomers. *Acta Mechanica*, 210:183–214, 03 2010.
- [51] A. Dorfmann and R. W. Ogden. Nonlinear magnetoelastic deformations. *The Quarterly Journal of Mechanics and Applied Mathematics*, 57(4):599–622, 11 2004.
- [52] M.H.B.M. Shariff, R. Bustamante, M. Hossain, and P. Steinmann. A novel spectral formulation for transversely isotropic magneto-elasticity. *Mathematics and Mechanics of Solids*, 22(5):1158–1176, 2017.

- [53] P. Saxena, M. Hossain, and P. Steinmann. A theory of finite deformation magneto-viscoelasticity. *International Journal of Solids and Structures*, 50(24):3886–3897, 2013.
- [54] P. Saxena, M. Hossain, and P. Steinmann. Nonlinear magneto-viscoelasticity of transversally isotropic magneto-active polymers. *Proceedings of the Royal Society A: Mathematical, Physical and Engineering Sciences*, 470(2166):20140082, 2014.
- [55] R. Bustamante, M.H.B.M. Shariff, and M. Hossain. Mathematical formulations for elastic magneto-electrically coupled soft materials at finite strains: Time-independent processes. *International Journal of Engineering Science*, 159:103429, 2021.
- [56] K Haldar, B Kiefer, and A Menzel. Finite element simulation of rate-dependent magneto-active polymer response. *Smart Materials and Structures*, 25(10):104003, sep 2016.
- [57] F. Dadgar-Rad and M. Hossain. Large viscoelastic deformation of hard-magnetic soft beams. *Extreme Mechanics Letters*, 54:101773, 2022.
- [58] G. Ethiraj and C. Miehe. Multiplicative magneto-elasticity of magnetosensitive polymers incorporating micromechanically-based network kernels. *International Journal of Engineering Science*, 102:93–119, 2016.
- [59] D. Garcia-Gonzalez and M. Hossain. A microstructural-based approach to model magneto-viscoelastic materials at finite strains. *International Journal of Solids and Structures*, 208-209:119–132, 2021.
- [60] R. Gholami, R. Ansari, and Y.Gholami. Size-dependent bending, buckling and vibration of higher-order shear deformable magneto-electro-thermo-elastic rectangular nanoplates. *Materials Research Express*, 4:065702, 2017.
- [61] M. Xu, I. M. Gitman, and H. Askes. A gradient-enriched continuum model for magneto-elastic coupling: Formulation, finite element implementation and in-plane problems. *Computers and Structures*, 212:275–288, 2019.
- [62] L. Ke, Y. Wang, J. Yang, and S. Kitipornchai. Free vibration of size-dependent magneto-electro-elastic nanoplates based on the nonlocal theory. *Acta Mechanica Sinica*, 30:516–525, 2014.

- 
- [63] M. Arefi, M. Kiani, and T. Rabczuk. Application of nonlocal strain gradient theory to size dependent bending analysis of a sandwich porous nanoplate integrated with piezomagnetic face-sheets. *Composites Part B: Engineering*, 168:320–333, 2019.
- [64] R. Zabihiyan, J. Mergheim, J.P. Pelteret, B. Brands, and P. Steinmann. Fe2 simulations of magnetorheological elastomers: influence of microscopic boundary conditions, microstructures and free space on the macroscopic responses of mres. *International Journal of Solids and Structures*, 193-194:338–356, 2020.
- [65] K. A. Kalina, P. Metsch, J. Brummund, and M. Kästner. A macroscopic model for magnetorheological elastomers based on microscopic simulations. *International Journal of Solids and Structures*, 193-194:200–212, 2020.
- [66] E. Galipeau, S. Rudykh, G. deBotton, and P. Ponte Castañeda. Magnetoactive elastomers with periodic and random microstructures. *International Journal of Solids and Structures*, 51(18):3012–3024, 2014.
- [67] A. Javili, G. Chatzigeorgiou, and P. Steinmann. Computational homogenization in magneto-mechanics. *International Journal of Solids and Structures*, 50(25):4197–4216, 2013.
- [68] Z. Hashin. Analysis of Composite Materials—A Survey. *Journal of Applied Mechanics*, 50:481–505, 1983.
- [69] R. Hill. Elastic properties of reinforced solids: Some theoretical principles. *Journal of the Mechanics and Physics of Solids*, 11:357–372, 1963.
- [70] J. Lemaitre. *Continuum damage mechanics : theory and applications*. LISM Courses and Lectures ; 295. Springer, Wien, 1st ed. 1987. edition, 1987.
- [71] Jan G. M. van Mier. *Fracture Processes of Concrete*. CRC Press, London, 1st ed. 1997. edition, 1997.
- [72] M.R.A. van Vliet. Doctoral thesis, Delft University Press, 2000.
- [73] P. Evesque and F. Adjemian. Stress fluctuations and macroscopic stick-slip in granular materials. *The European physical journal. E, Soft matter*, 9:253–9, 12 2002.
- [74] W.J. Drugan and J.R. Willis. A micromechanics-based nonlocal constitutive equation and estimates of representative volume element size for elastic composites. *Journal of the Mechanics and Physics of Solids*, 44(4):497–524, 1996.

- [75] P. Metsch, K. A. Kalina, C. Spieler, and M. Kästner. A numerical study on magnetostrictive phenomena in magnetorheological elastomers. *Computational Materials Science*, 124:364–374, 2016.
- [76] S. Sun, X. Peng, and Z. Guo. Study on Macroscopic and Microscopic Mechanical Behavior of Magnetorheological Elastomers by Representative Volume Element Approach. *Advances in Condensed Matter Physics*, 2014.
- [77] H. Mane. *Mathematical Modeling and Numerical Simulation of Magnetoelastic Coupling*. Doctoral thesis, Technische Universität Kaiserslautern, 2019.
- [78] F. Claeysen, N. Lhermet, F. Barillot, and R. Le Letty. Giant dynamic strains in magnetostrictive actuators and transducers. *ISAGMM 2006 CONF*, 2006.
- [79] A. K. Soh, , and J.X. Liu. On the constitutive equations of magnetoelastic solids. *Journal of Intelligent Material Systems and Structures*, 16(7-8):597–602, 2005.
- [80] Ieee standard on magnetostrictive materials: Piezomagnetic nomenclature. *IEEE Std 319-1990*, pages 1–, 1991.
- [81] S. Eraslan, I. M. Gitman, H. Askes, and R. de Borst. Determination of representative volume element size for a magnetorheological elastomer. *Computational Materials Science*, 203:111070, 2022.
- [82] Y. Pang, J. Liu, Y. Wang, and D. Fang. Wave propagation in piezoelectric/piezomagnetic layered periodic composites. *Acta Mechanica Solida Sinica*, 21:483 – 490, 2008.
- [83] Z. P. Bažant. Size effect. *International Journal of Solids and Structures*, 37:69–80, 2000.
- [84] R. D. Mindlin. Micro-structure in linear elasticity. *Archive for Rational Mechanics and Analysis*, 16:51–78, 1964.
- [85] A. C. Eringen. Linear theory of nonlocal elasticity and dispersion of plane waves. *International Journal of Engineering Science*, 10:425–435, 1972.
- [86] D.C.C. Lam, F. Yang, A.C.M. Chong, J. Wang, and P. Tong. Experiments and theory in strain gradient elasticity. *Journal of the Mechanics and Physics of Solids*, 51:1477 – 1508, 2003.

- 
- [87] F. Yang, A.C.M. Chong, D.C.C. Lam, and P. Tong. Couple stress based strain gradient theory for elasticity. *International Journal of Solids and Structures*, 39:2731–2743, 2002.
- [88] C. Zhou, Y. Sai, and J. Chen. Tunable lamb wave band gaps in two-dimensional magnetoelastic phononic crystal slabs by an applied external magnetostatic field. *Ultrasonics*, 71:69–74, 2016.
- [89] J. O. Vasseur, O. Bou Matar, J. F. Robillard, A.-C. Hladky-Hennion, and P. A. Deymier. Band structures tunability of bulk 2d phononic crystals made of magnetoelastic materials. *AIP Advances*, 1:041904, 2011.
- [90] R. Ding, X. Su, J. Zhang, and Y. Gao. Tunability of longitudinal wave band gaps in one dimensional phononic crystal with magnetostrictive material. *Journal of Applied Physics*, 115:074104, 2014.
- [91] O. Bou Matar, J.F. Robillard, J. Vasseur, A.C. Hladky-Hennion, P. Deymier, P. Pernod, and V. Preobrazhensky. Band gap tunability of magneto-elastic phononic crystal. *Journal of Applied Physics*, 111, 2012.
- [92] T.T. Wu, L.C. Wu, and Z.G. Huang. Frequency band-gap measurement of two-dimensional air/silicon phononic crystals using layered slanted finger interdigital transducers. *Journal of Applied Physics*, 97:094916, 2005.
- [93] Y. Song. *The influence of random microstructure on wave propagation through heterogeneous media*. Doctoral thesis, The University of Sheffield, 2015.
- [94] F.M. Li and Y. Wang. Elastic wave propagation and localization in band gap materials: A review. *Science China Physics, Mechanics and Astronomy*, 55, 10 2012.
- [95] M. Kushwaha, P. Halevi, L. Dobrzynski, and B. Djafari-Rouhani. Acoustic band structure of periodic elastic composites. *Physical review letters*, 71:2022–2025, 1993.
- [96] M. Sigalas and E.N. Economou. Band structure of elastic waves in two dimensional systems. *Solid State Communications*, 86:141–143, 1993.
- [97] Y. Song, I. Gitman, W. Parnell, and H. Askes. The influence of random microstructure on wave propagation through heterogeneous media. *International Journal of Fracture*, 204, 2017.

- [98] J. Vasseur, P.A. Deymier, B. Chenni, B. Djafari-Rouhani, L. Dobrzynski, and D. Prevoist. Experimental and theoretical evidence for the existence of absolute acoustic band gaps in two-dimensional solid phononic crystals. *Physical review letters*, 86:3012–5, 2001.
- [99] Y. Wang, F.M.Li, K. Kishimoto, Y.S.Wang, and W.H. Huang. Elastic wave band gaps in magnetoelastic phononic crystals. *Wave Motion*, 46:47–56, 2009.
- [100] J. Baumgartl, M. Zvyagolskaya, and C. Bechinger. Tailoring of phononic band structures in colloidal crystals. *Phys. Rev. Lett.*, 99:205503, 2007.
- [101] G. Zhang and Y. Gao. Tunability of band gaps in two-dimensional phononic crystals with magnetorheological and electrorheological composites. *Acta Mechanica Sinica Sinica*, 34:1–13, 2020.
- [102] J.F. Robillard, O. Bou Matar, J. Vasseur, P. Deymier, M. Stippinger, A.C. Hladky-Hennion, Y. Pennec, and B. Djafari-Rouhani. Tunable magnetoelastic phononic crystals. *Applied Physics Letters*, 95, 2009.
- [103] S. Zhang, Y. Shi, and Y. Gao. A mechanical-magneto-thermal model for the tunability of band gaps of epoxy/terfenol-d phononic crystals. *Journal of Applied Physics*, 118(3), 2015.
- [104] S. Zhang, Y. Shi, and Y. Gao. Tunability of band structures in a two-dimensional magnetostrictive phononic crystal plate with stress and magnetic loadings. *Physics Letters A*, 381:1055–1066, 2017.
- [105] I. M. Gitman and Y. Song. Fibonacci sequence for modelling stop bands in random microstructure. *ZAMM - Journal of Applied Mathematics and Mechanics / Zeitschrift für Angewandte Mathematik und Mechanik*, 98:270–276, 2018.
- [106] R. De Borst and H. B. Mühlhaus. Gradient-dependent plasticity: Formulation and algorithmic aspects. *International Journal for Numerical Methods in Engineering*, 35:521–539, 1992.
- [107] Geers, M. G.D., de Borst, R., Brekelmans, W. A.M., and Peerlings, R. H.J. On the use of local strain fields for the determination of the intrinsic length scale. *J. Phys. IV France*, 08:Pr8–167–Pr8–174, 1998.

- 
- [108] H. Askes and A. V. Metrikine. One-dimensional dynamically consistent gradient elasticity models derived from a discrete microstructure: Part 2: Static and dynamic response. *European Journal of Mechanics - A/Solids*, 21:573–588, 2002.
- [109] A. V. Metrikine and H. Askes. One-dimensional dynamically consistent gradient elasticity models derived from a discrete microstructure: Part 1: Generic formulation. *European Journal of Mechanics - A/Solids*, 21:555–572, 2002.
- [110] V. Kouznetsova, M. Geers, and W. Brekelmans. Size of a representative volume element in a second-order computational homogenization framework. *International Journal for Multiscale Computational Engineering*, 2:575–598, 2004.
- [111] I. Gitman, H. Askes, L. Sluys, and O. Lloberas-Valls. *The concept of Representative Volume Elements for elastic, hardening and softening materials*, page 1–5. 2004.
- [112] I. Gitman, M. Gitman, and H. Askes. Quantification of stochastically stable representative volumes for random heterogeneous media. *Archive of Applied Mechanics*, 75:79–92, 2006.
- [113] Y. Z. Wang, F. M. Li, W. H. Huang, X. Jiang, Y. S. Wang, and K. Kishimoto. Wave band gaps in two-dimensional piezoelectric/piezomagnetic phononic crystals. *International Journal of Solids and Structures*, 45:4203 – 4210, 2008.
- [114] O. van der Sluis, P.J.G. Schreurs, and H.E.H. Meijer. Homogenisation of structured elastoviscoplastic solids at finite strains. *Mechanics of Materials*, 33(9):499–522, 2001.
- [115] K. Terada, M. Hori, T. Kyoya, and N. Kikuchi. Simulation of the multi-scale convergence in computational homogenization approaches. *International Journal of Solids and Structures*, 37(16):2285–2311, 2000.
- [116] H. Askes, S. Piercy, and S. Ilanko. Tyings in linear systems of equations modelled with positive and negative penalty functions. *Communications in Numerical Methods in Engineering*, 24:1163–1169, 2008.
- [117] S. Eraslan, I. M. Gitman, M. Xu, H. Askes, and R. de Borst. Representative volume element size and length scale identification in generalised magneto-elasticity. In H. Altenbach, A. Berezovski, F. dell’Isola, and A. Porubov, editors, *Sixty Shades of Generalized Continua*. Springer Cham, 2023. In press.

- [118] V. Kouznetsova, M. G. D. Geers, and W. A. M. Brekelmans. Multi-scale constitutive modelling of heterogeneous materials with a gradient-enhanced computational homogenization scheme. *International Journal for Numerical Methods in Engineering*, 54:1235–1260, 2002.
- [119] Ze-Ping Wang and C.T. Sun. Modeling micro-inertia in heterogeneous materials under dynamic loading. *Wave Motion*, 36(4):473–485, 2002.
- [120] M. B. Rubin, P. Rosenau, and O. Gottlieb. Continuum model of dispersion caused by an inherent material characteristic length. *Journal of Applied Physics*, 77:4054–4063, 1995.
- [121] H. B. Muhlhaus and E. C. Aifantis. The influence of microstructure-induced gradients on the localization of deformation in viscoplastic materials. *Acta mechanica*, 89:217–231, 1991.
- [122] E. C. Aifantis. On the role of gradients in the localization of deformation and fracture. *International Journal of Engineering Science*, 30(10):1279–1299, 1992.
- [123] C.Q. Ru and E. Aifantis. A simple approach to solve boundary-value problems in gradient elasticity. *Acta Mechanica*, 101:59–68, 03 1993.
- [124] B. S. Altan and E. C. Aifantis. On some aspects in the special theory of gradient elasticity. *Journal of the Mechanical Behavior of Materials*, 8:231 – 282, 1997.
- [125] H. Askes and E. C. Aifantis. Gradient elasticity in statics and dynamics: An overview of formulations, length scale identification procedures, finite element implementations and new results. *International Journal of Solids and Structures*, 48:1962–1990, 2011.
- [126] H. Askes, I. Morata, and E. C. Aifantis. Finite element analysis with staggered gradient elasticity. *Computers & Structures*, 86:1266–1279, 2008.
- [127] M.Yu. Gutkin and E.C. Aifantis. Edge dislocation in gradient elasticity. *Scripta Materialia*, 36:129–135, 1997.
- [128] M.I Sigalas, M. Kushwaha, E. Economou, M. Kafesaki, I. Psarobas, and W. Steurer. Classical vibrational modes in phononic lattices: Theory and experiment. *Zeitschrift Fur Kristallographie*, 220:765–809, 05 2005.

- 
- [129] J Vasseur, PA Deymier, P. Khelif, A. and Lambin, B. Djafari-Rouhani, A. Akjouj, L. Dobrzynski, N Fettouhi, and J. Zemmouri. Phononic crystal with low filling fraction and absolute acoustic band gap in the audible frequency range: A theoretical and experimental study. *Physical review. E, Statistical, nonlinear, and soft matter physics*, 65:056608, 06 2002.
- [130] Z. Shu, H. Jia, and C. Jian-Chun. Experimental and theoretical evidence for the existence of broad forbidden gaps in the three-component composite. *Chinese Physics Letters*, 20:1303, 2003.
- [131] K. NAKASHIMA, S. BIWA, and E. MATSUMOTO. Elastic wave transmission and stop band characteristics in unidirectional composites. *Journal of Solid Mechanics and Materials Engineering*, 2:1195–1206, 2008.
- [132] J. O. Vasseur and P. A. Deymier. Propagation of acoustic waves in periodic and random two-dimensional composite media. *Journal of Materials Research*, 12:2207–2212, 1997.
- [133] J.C. Hsu and T.T. Wu. Efficient formulation for band-structure calculations of two-dimensional phononic-crystal plates. *Physical Review B - PHYS REV B*, 74, 2006.
- [134] M. Lan and P. Wei. Band gap of piezoelectric/piezomagnetic phononic crystal with graded interlayer. *Acta Mechanica*, 225, 2014.
- [135] S. Eraslan, I. Gitman, H. Askes, and R. Borst. Effects of randomness and piezomagnetic coupling on the appearance of stop-bands in heterogeneous magnetorheological elastomers. *Archive of Applied Mechanics*, 93:1–15, 05 2023.
- [136] Q. Hu, W. Yang, and S. Zhang. Studies on band structure of magneto-elastic phononic crystal nanoplates using the nonlocal theory. *Physics Letters A*, 423:127820, 2022.
- [137] L. L. Ke and Y. S. Wang. Free vibration of size-dependent magneto-electro-elastic nanobeams based on the nonlocal theory. *Physica E: Low-dimensional Systems and Nanostructures*, 63:52–61, 2014.

- [138] S. Zhang and Y. Gao. Flexural wave band structure of magneto-elastic phononic crystal nanobeams based on the nonlocal theory. *Physics Letters A*, 390:127090, 2021.
- [139] M. Xu, H. Askes, and I. M. Gitman. Mono-scale and multi-scale formulations of gradient-enriched dynamic piezomagnetism. *Wave Motion*, 91:102402, 2019.
- [140] M. Xu, I. M. Gitman, P. Wei, and H. Askes. Finite element implementation of a multi-scale dynamic piezomagnetic continuum model. *Computers & Structures*, 240:106352, 2020.